공학박사학위논문

Development of optical and γ-ray diagnostics for a nonlinear Compton scattering experiment with a multi-PW laser

PW 레이저를 이용한 비선형 컴프톤 산란 실험을 위한 광학 및 감마선 진단계 개발

2023 년 2 월

서울대학교 대학원

에너지시스템공학부

김 도 연

Development of optical and γ−ray diagnostics for a nonlinear Compton scattering experiment with a multi−PW laser

지도 교수 황 용 석

이 논문을 공학박사 학위논문으로 제출함
2023 년 2 월

서울대학교 대학원
에너지시스템공학부
김 도 연

김도연의 공학박사 학위논문을 인준함
2023 년 2 월

위 원 장   김 기 현   (인)

부위원장   황 용 석   (인)

위 　 원   정 경 재   (인)

위 　 원   남 창 희   (인)

위 　 원   김 기 용   (인)

Abstract

Development of optical and γ－ray diagnostics for a nonlinear Compton scattering experiment with a multi－PW laser

Doyeon Kim

Department of Energy System Engineering

The Graduate School

Seoul National University

Optical and γ－ray diagnostics has been developed for a nonlinear Compton scattering (NCS) between an ultra－relativistic electron beam and an ultrahigh intensity laser. With the advancement of PW laser technology, strong field physics entered a new physics regime of strong field quantum electrodynamics. Based on the laser wakefield acceleration scheme, a multi－GeV electron beam could be produced by driving a He gas target with a PW laser. When this ultra－relativistic GeV electron beam scatters with an ultrahigh intensity laser beam, multi－photon Compton scattering, i.e., NCS, can occur, generating γ－rays beyond the cutoff energy of linear Compton scattering.   In order to perform the NCS experiment, the

spatiotemporal synchronization between the electron-driving main laser and the scattering laser is critical for the realization of Compton scattering. With the installation of two optical delay monitoring systems the temporal synchronization between the two laser beams was monitored and controlled, which allowed the successful demonstration of Compton scattering and provided the success rate of Compton scattering as high as 40%.

Generated γ-rays from the Compton scattering were diagnosed using two scintillation detectors – single crystal LYSO for imaging and pixelated LYSO for energy spectrum. The gamma ray energy spectrum generated by NCS was retrieved using two methods – the first method based on the NCS cross section (cross-sectional method) and the other by the simultaneous iterative reconstruction technique. In order to apply the cross-sectional method, it is necessary to know the laser intensity during the scattering. The laser intensity during the scattering and number of scattered electrons were obtained by reconstructing a gamma-ray profile. Finally, the gamma-ray energy spectrum was calculated using the cross-sectional method. In addition, the gamma-ray energy spectrum was obtained independently from the response of the pixelated gamma-ray scintillator using the simultaneous iterative reconstruction technique. The reconstructed result showed that the gamma-ray energy spectrum extended up to several hundred MeV, which is well beyond the cutoff energy of linear Compton scattering, confirming the realization of NCS. Through this study, the particle interaction under the strong field was experimentally investigated. In addition,

the gamma ray generated by NCS is anticipated to be used as a high－

energy gamma－ray source.

Table of Contents

List of Tables

List of Figures

Chapter 1. Introduction

1.1. Strong field quantum electrodynamics

Quantum electrodynamics (QED) is a relativistic quantum field theory of electrodynamics. QED describes light－matter interactions by combining quantum mechanics and special relativity. QED is known to be an extremely precise theory. For example, the magnetic dipole moment predicted by QED agrees with the experimentally measured value up to 12 significant number[1, 2]. When relativistic charged particles are exposed to extremely strong electric and magnetic fields, QED in a strong field, or strong field QED is applied to light－matter interactions. Under a strong electric field, called the Schwinger field[3, 4], an electron gains the energy of mc^2 over a Compton wavelength, $\bar{\lambda}_C = \frac{\hbar}{m_e c} = 3.9 \times 10^{-11}$ cm and the production of electron－positron pairs can occur from vacuum fluctuations[3, 5]. Here m_e is the electron mass and c the speed of light and $\hbar$ the reduced Planck constant. The laser intensity corresponding to the Schwinger electric field of 1.3×10^{16} V/cm is 2×10^{29} W/cm^2, which is 10^6 times higher than the world－record laser intensity of $1 \times 10^{23} W/cm^2$ [6]. As a consequence, physical phenomena of strong field QED have rarely been observed in a laboratory because it is not feasible to create the Schwinger field in the lab frame.

Light－matter interaction between ultra－relativistic electron and ultrahigh intensity laser can offer a chance to investigate strong field QED experimentally. When an ultrahigh intensity laser backscatters

1

with an ultra−relativistic electron, the electron experiences an enhanced laser field, due to the relativistic Doppler shift, close to the Schwinger limit. The interaction of an ultra−relativistic electron with an ultrahigh intensity electromagnetic field can be represented by a characteristic parameter, called quantum nonlinearity parameter, χ_e, which is expressed as follows [7] [8]:

$$\chi_e = \frac{1}{m_e c^2} \frac{\bar{\lambda}_C}{c} \sqrt{\left(\frac{e}{m_e} F_{\mu\nu} p^\nu\right)^2} = \frac{E}{E_S} \qquad (1.1)$$

where e is an electron charge, $p = (E_p, p)$ denotes the four−momentum of an electron, E is an electric field and E_S is the Schwinger field. When χ_e is comparable to or greater than 1, strong field QED phenomena are expected to occur. For example, a 4 GeV electron backscatters with an ultrahigh intensity laser with an intensity of $1 \times 10^{21} W/cm^2$, χ_e is about 1.

1.2. Nonlinear Compton scattering

Compton scattering is the inelastic scattering of a hard x−ray or gamma−ray photon with an electron. The physical nature of Compton scattering depends on the strength of an incident electromagnetic field. When an ultra−relativistic electron encounters an ultrahigh intensity laser, the electron can experience a Lorentz−boosted electromagnetic field near the Schwinger field and strong field QED phenomena are expected to occur. Under a strong electromagnetic field, nonlinear Compton scattering (NCS) emits a gamma−ray from a simultaneous collision of an electron with two or more photons, has attracted strong attention because it can offer an opportunity to

explore strong field QED processes.

With the development of ultrashort high power lasers based on the chirped pulse amplification technique, the realization of NCS has been pursued in a number of laboratories. In 1996, a series of experiments on NCS were performed at SLAC with a 46.6 GeV electron beam and a laser with peak intensity of $a_0 \approx 0.6$[9]. Here $a_0 = \frac{eE}{m\omega_0 c}$ is the normalized vector potential of a laser with e and m being the charge and the mass of electron, respectively, E a field amplitude, and ω_0 a frequency. From this experiment, it was reported a multiphoton Compton scattering up to four photons from the electron energy reduction after the scattering. Since the development of ultrahigh power lasers and the laser wakefield acceleration method [10], all−optical inverse Thomson and Compton scatterings have been actively researched [11−14]. In 2017, W. Yan et al.[15] observed high−order multiphoton Thomson scattering between an ultra−relativistic laser and a high intensity laser. In 2018, K. Poder et al.[16] conducted an inverse Compton scattering with laser intensity of $a_0 \sim 10$ and electron energy reaching up to 1.5 GeV, claiming the observation of a radiation reaction effect. So far, all optical NCS has not been realized.

1.3. Purpose and significance

PW lasers have been developed at Center for Relativistic Laser Science of Institute for Basic Science and applied to charged particle acceleration. Two PW laser beamlines of 1.5 PW and 1.0 PW at 30 fs were established during the Ultrashort quantum beam facility project, carried out for 9 years till 2012. The 1.5 PW beamline was upgraded to a 4 PW at 20 fs in 2017 at CoReLS[17], and utilized for the investigations of strong field physics. By applying the laser wakefield acceleration scheme, a multi−GeV electron beam could be produced by driving a He gas target with a PW laser. With this ultra−relativistic electron beam and an ultrahigh intensity laser, we can pursue the realization of NCS by introducing a set of optical synchronization systems. Since the generation of a multi−GeV electron beam is accomplished by a PW laser, this is an all optical NCS experiment.

In addition, we pursue the direct measurement of Compton gamma rays to confirm the Compton scattering process. In the previous studies, the Compton scattering was confirmed through the measurements of the gamma−ray yield depending on the synchronization between an electron beam and a scattering laser[11] and the electron energy loss during the Compton scattering[9, 16]. The most intuitive way to verify the occurrence of NCS is to measure the gamma−ray energy reaching beyond the cutoff energy of linear Compton scattering. In this research, optical and γ−ray diagnostics are developed to obtain gamma−ray energy spectra from NCS.

The gamma rays from NCS are expected to possess unique

properties not found from other gamma-ray sources. The NCS gamma rays is expected to exhibit an energy spectrum extending up to hundreds of MeV. The high energy gamma-ray can be used as radiation sources for linear/nonlinear Breit-Wheeler pair production[18-20], particle physics[21-25] and muon generation[26]. The divergence of NCS gamma-ray is proportional to $1/\gamma$, one over Lorentz factor of electron[27]. With the ultra-relativistic electron, a point-like gamma-ray source can be applied for the flash radiotherapy[28-30].

The structure of this thesis is as follows. In chapter 2, an overall set-up for a NCS experiment is described. The experimental tools of ultrahigh power laser and ultra-relativistic electron generation are described in details. The principle and utility of optical synchronization systems is explained. Diagnostics for electron and gamma-ray are presented. Also, experimental procedure and representative results are described. Chapter 3 deals with gamma-ray characterization. The methods to simulate an electron beam and scattering laser beam in the (x, y, z, t) coordinate, to estimate a laser intensity during the scattering process, and to obtain the gamma-ray energy spectra are presented in details. Finally, a conclusion is given in Chap. 4.

Chapter 2. Nonlinear Compton scattering experiment

2.1. Introduction

For the experimental investigation of light−matter interaction in a strong field, a scheme of an inverse Compton scattering between an ultra−relativistic electron beam and an ultrahigh intensity laser, as shown in Figure 2.1, was adopted. When the laser intensity with $a_0 > 1$ is applied, the electron scatters simultaneously with many photons and the scattering becomes a nonlinear Compton scattering (NCS), i.e., multi−photon Compton scattering.
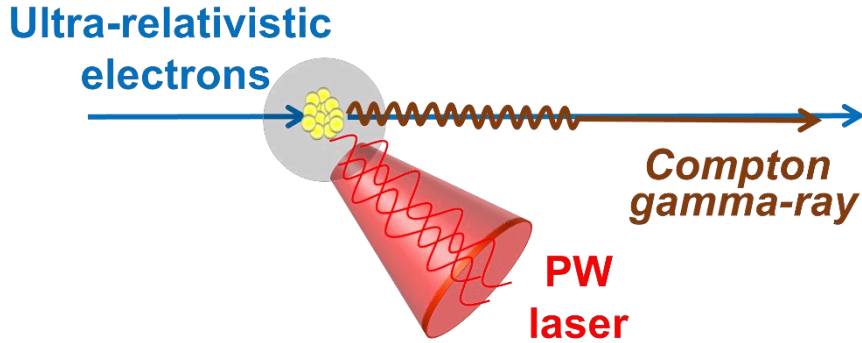
Figure 2.1: Schematics of all−optical nonlinear Compton scattering. An ultra−relativistic electron beam, accelerated by laser wakefield acceleration, makes a scattering with an ultrahigh intensity laser beam, which generates gamma rays along the electron propagation direction.

In order to perform a nonlinear Compton scattering experiment, several key components are required. These include an ultra−relativistic electron beam, an ultrahigh intensity scattering laser beam, a synchronization system, and diagnostic tools to measure and analyze experimental results. The electron beam was produced by the laser wakefield acceleration method using a main driving laser with a peak intensity of $a_0 \approx 2$. The ultrahigh intensity scattering laser had a peak intensity of $a_0 \approx 13$. For the synchronization between the main and the scattering laser beams, spatial and spectral interferometers were introduced. For the measurement of scattering results, diagnostic tools were used to characterize the beam profiles and the energy spectra of electron and laser beams. The experimental layout for an NCS experiment in Fig. 2.1 shows the key components and systems. The red dashed box indicates the region where the electrons are accelerated and scattered, the black−dashed box shows the diagnostic tools for the electron and gamma−ray, and the purple color represents the spatiotemporal synchronization system. A real−time delay measurement system is also shown.

The structure of this chapter is as follows. In Section 2.2, the specifications of the main driving laser and the scattering laser are described, along with the information on how the focal spots of the two lasers were optimized. Section 2.3 covers the generation of ultra−relativistic electrons using the laser wakefield acceleration method, with a particular focus on the plasma density and the focusing position of the laser. The spatiotemporal synchronization systems are introduced in Section 2.4, including information on how

to synchronize the two laser beams and to measure the time delay between them as well as the necessity and benefits of a real-time delay measurement system. The diagnostics for electrons and gamma-rays are discussed in Section 2.5, and experimental results and conclusions are presented in Section 2.6.
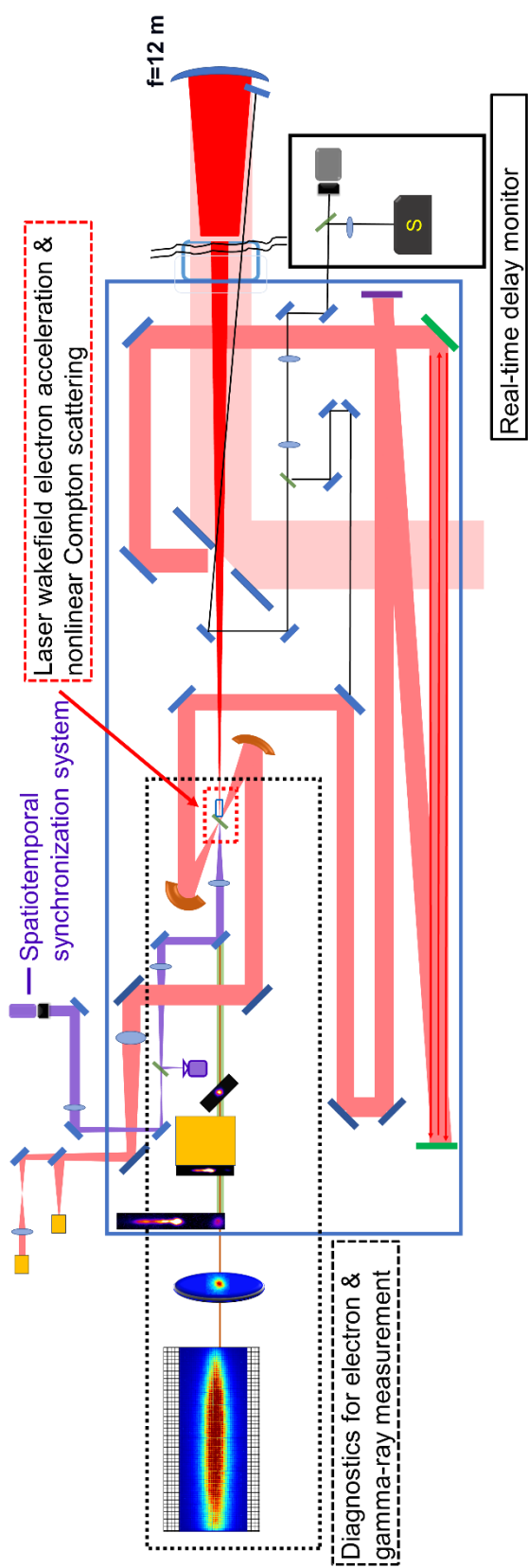
Figure 2.2: Schematics of experimental setup for the nonlinear Compton scattering.

2.2. Ultrahigh power laser

The history of LASER (Light Amplification by Stimulated Emission of Radiation) begins with A. Einstein's introduction of the concept of stimulated emission in 1917[31]. Since T. H. Maiman developed the first functional laser in 1960 using an $Al_2O_3:Cr$ ruby crystal and a helical flash lamp[32], laser technology has been researched to boost the laser peak power. Through the introduction of Q-switching[33] and mode-locking[34-36], the magnitude of peak power increased several orders. In late 1980s, the laser intensity had a big jump thanks to the development of the chirped pulse amplification technique[37], as shown in Figure 2.3.
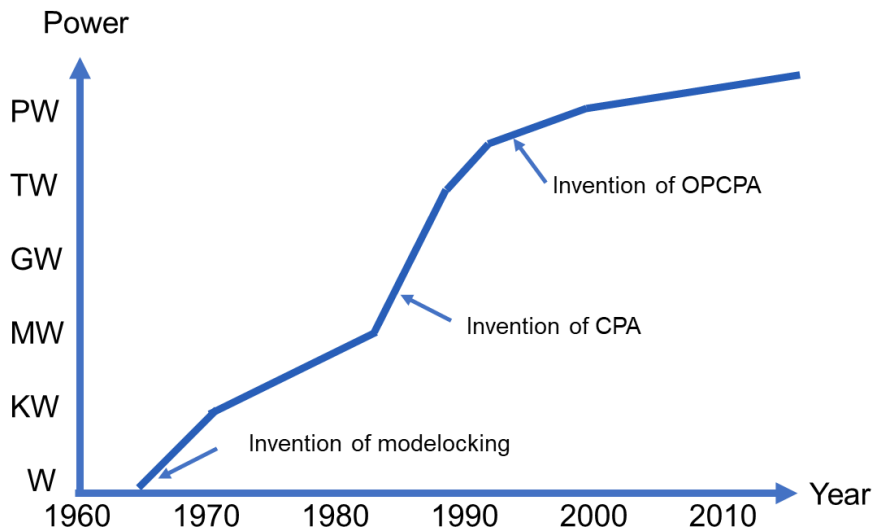
Figure 2.3 Historical advancement of laser power. [adapted from Figure 1 of Danson[38]]
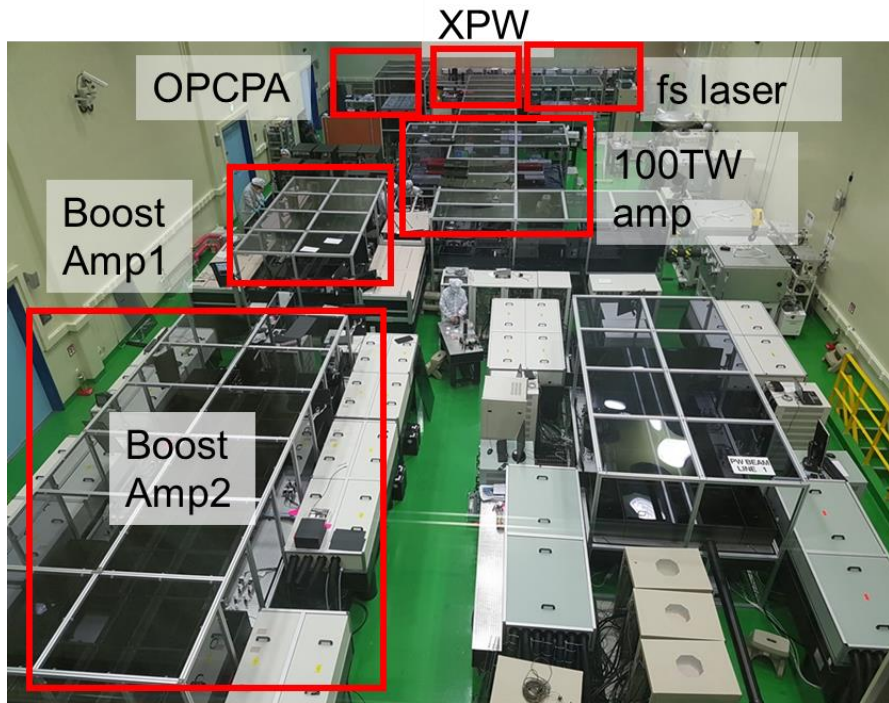
Figure 2.4: 4 PW laser operated at CoReLS. From the top of the figure, fs laser, optical parametric chirped-pulse amplification (OPCPA), cross-polarized wave (XPW) stage, 100TW amplifier and booster amplifiers. After the booster amplifiers, the laser pulse was compressed in a compressor with four grating to produce 20 fs, 4 PW laser pulses.

The Center for Relativistic Laser Science (CoReLS) is operating a Ti:Sapphire laser facility with a peak power of 4 PW at 20 fs[17]. For an NCS experiment, an ultrahigh power laser with a 280 mm diameter, energy of 34 J and a pulse width of 20 − 25 fs was prepared. The laser beam was split into two parts by a holed mirror. The scattering laser beam passed through the hole with a diameter of 70 mm. The main driving laser beam was reflected by the holed mirror and sent to the focusing mirror for electron acceleration.

2.2.1 Main driving laser

A multi−GeV electron beam was generated by focusing the main driving laser onto a gas cell with a spherical mirror with a focal length of 12 m. The focal spot optimization system for the main driving laser beam was installed, as shown in Figure 2.5, to optimize the focal spot as close to the diffraction limit as possible. To prevent damage to the optics and cameras, the main driving laser beam was attenuated by about 7 orders during the focal spot optimization process. The main driving laser beam was split into two parts with the beam splitter in the focal spot optimization system. The transmitted laser beam was then imaged on the focal spot monitoring camera (EPIX, SV10M6). The position of the camera was determined by comparing the distance from the beam splitter to the gas cell to the distance from the beam splitter to the focal spot monitoring camera. The wavefront of the reflected laser beam at the deformable mirror was imaged on the wavefront sensor with a f=500 mm lens. The deformable mirror (AKA Optics) had 127 channels and a 300 mm diameter. The

deformable mirror was calibrated by measuring the wavefront deformation with respect to a voltage applied to each channel. In order to remove the aberrations of the main laser, the voltage applied to each channel of the deformable mirror was adjusted. Even though the wavefront was optimized initially by the deformable mirror, the measured focal spot could still have aberrations due to the alignment of the wavefront sensor and the imaging lens. In this case, low−order aberrations such as astigmatism and coma were provided as an offset to optimize the focal spot at the camera. For example, in Figure 2.7, an x−astigmatism of 0.2 was purposefully added to compensate for the aberration from the lens and the wavefront sensor. As a result, the focal spot was optimized to have a size of 45 μm (FWHM), which is larger by $1 - 2$ μm than the diffraction−limited size, providing a peak intensity of $a_0 \approx 2$ and a concentration ratio in the first airy disk that ranged from 45 to 55 %, as shown in Figure 2.6.
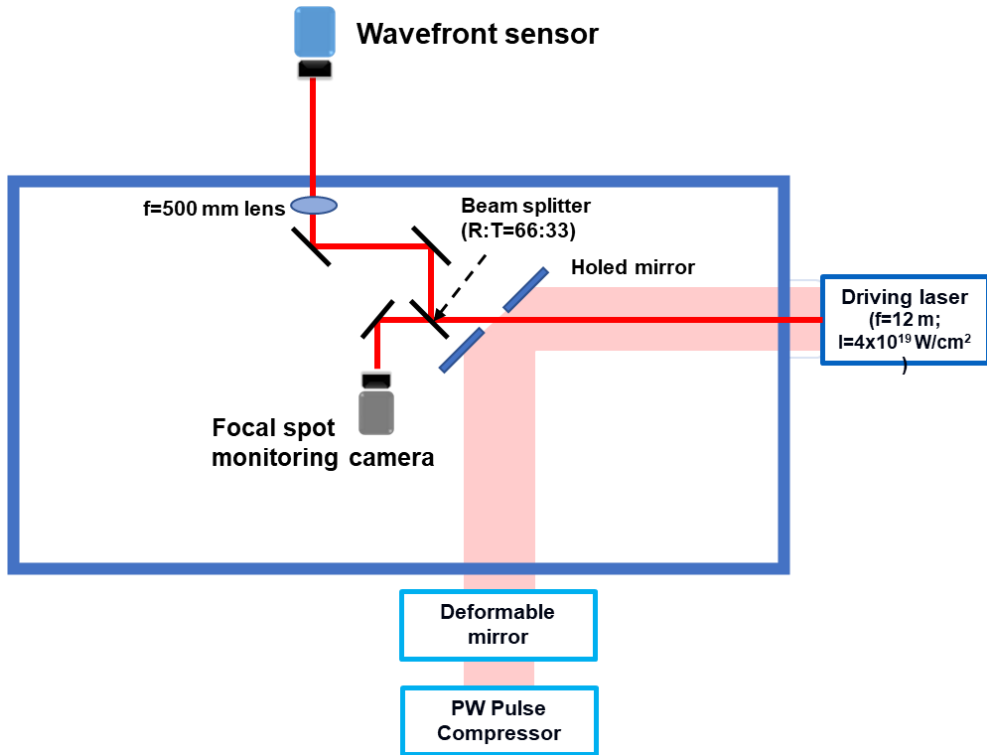
Figure 2.5: Focal spot optimizing system for the main driving laser. The main driving laser was split into two parts by the beam splitter during the focusing. The wavefront sensor received the reflected laser, and the focal spot monitoring camera received the transmitted laser. The deformable mirror was manipulated to minimize aberrations to achieve a near diffraction-limited focused spot.
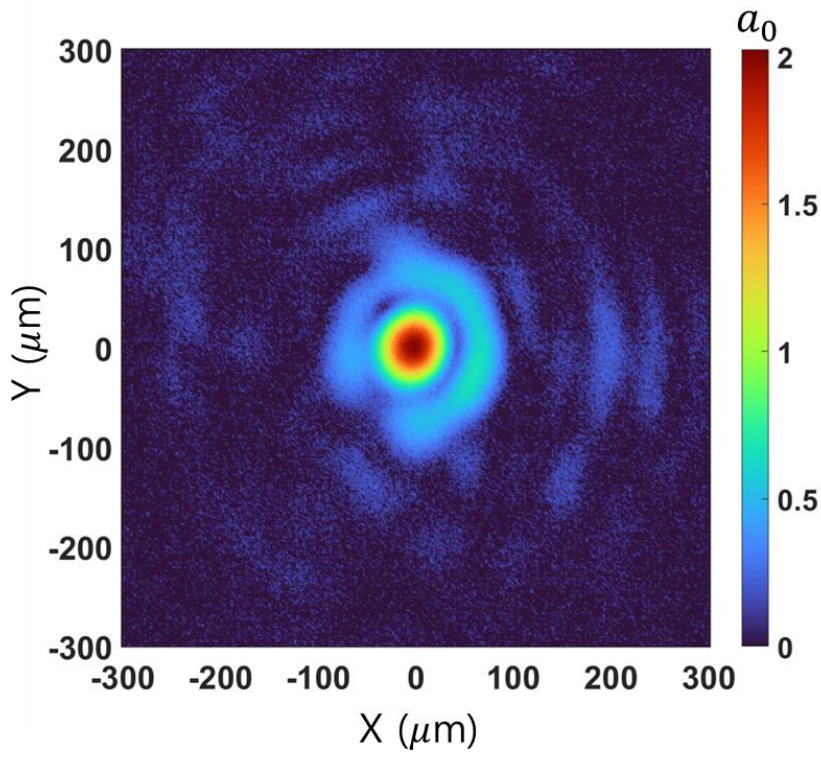
Figure 2.6: Typical focal spot image of the main driving laser. The focal spot had a size of 45 μm (FWHM). The first Airy disk contained 45−55% of the total energy. The peak intensity of the main driving laser was $I_0 = 1 \times 10^{19} w/cm^2$, corresponding to $a_0 \approx 2$.
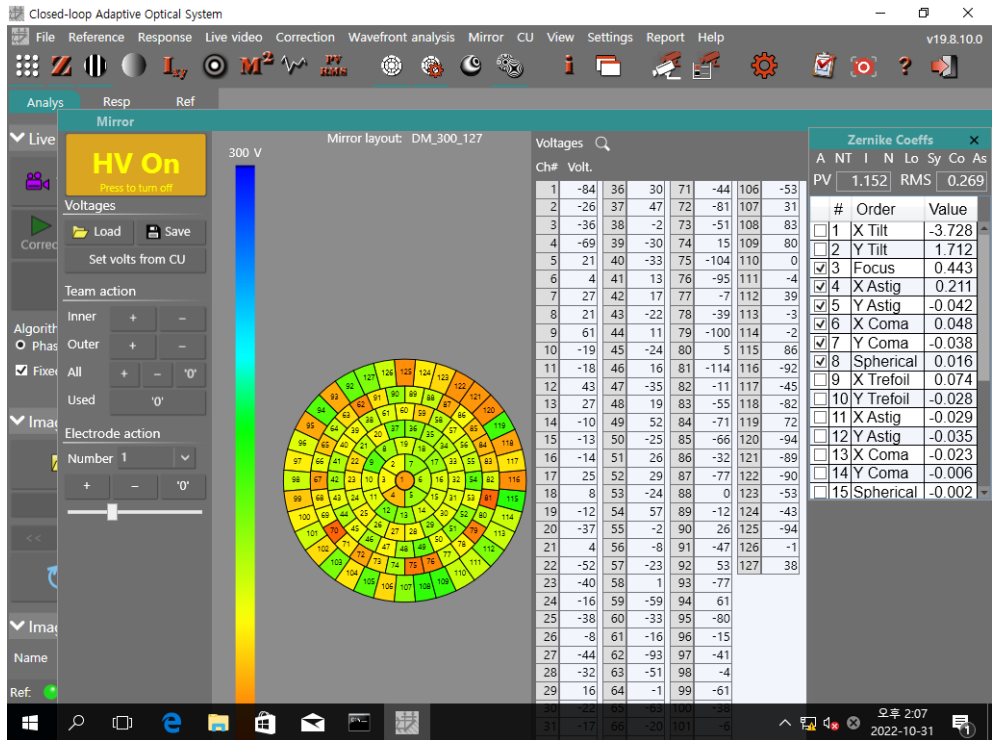
Figure 2.7: Snapshot of the deformable mirror software screen while optimizing the focal spot of the main driving laser.

2.2.2 Scattering laser

The scattering laser beam was delivered to an off-axis parabolic mirror and focused at the scattering position, which was located 30 mm away from the gas-cell exit. The scattering laser beam path was matched to that of the main driving laser from the holed mirror to the target, a distance of approximately 20 meters. The scattering laser beam optics consisted of an off-axis parabolic mirror, a delay stage, and 11 mirrors. Cameras were mounted on the back of each mirror to align the scattering laser beam. The off-axis parabolic mirror had a focal length of 161.3 mm. The delay stage (Newport, UTS150PPV6) had a travel range of 150 mm and an accuracy of 2 μm. In order to optimize the scattering laser beam, a focal spot monitoring camera (EPIX, SV10M6) with an objective lens (Hamamatsu, LCPlan N50x/0.65 IR) was prepared. Here, the objective lens was used for magnifying the focal spot image 16 times because the focal spot size was similar to the pixel size (1.67 μm) of the camera. The focal spot was optimized by adjusting the alignment of the off-axis parabolic mirror. As shown in Figure 2.9, the off-axis parabolic mirror was mounted on three linear stages, two rotation stages, and one gonio stage in order to optimize the focal spot at the scattering point. The position of the off-axis parabolic mirror was controlled by the three linear stages in different axes, and the reflection angle of the incidence plane and perpendicular to the incidence plane was adjusted using the two rotation and gonio stage. The focal spot was optimized by adjusting the alignment of the off-axis parabolic mirror, resulting in a focal spot size of 2.5 μm (FWHM) and a laser peak intensity of

$a_0 \approx 12$, as shown in Figure 2.8.
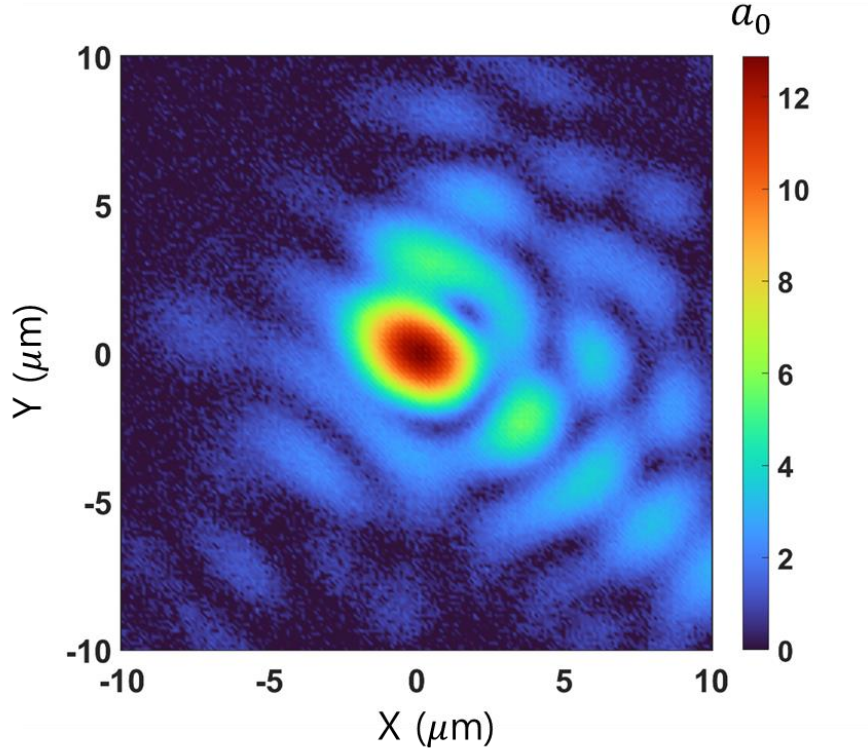
Figure 2.8: Typical focal spot image of the scattering laser beam. The focal spot had a size of 2.5 μm (FWHM). The Airy disk contained 40−50% of the total energy. The peak intensity of the scattering laser was $I_0 = 3.5 \times 10^{20} w/cm^2$, corresponding to $a_0 \approx 13$.
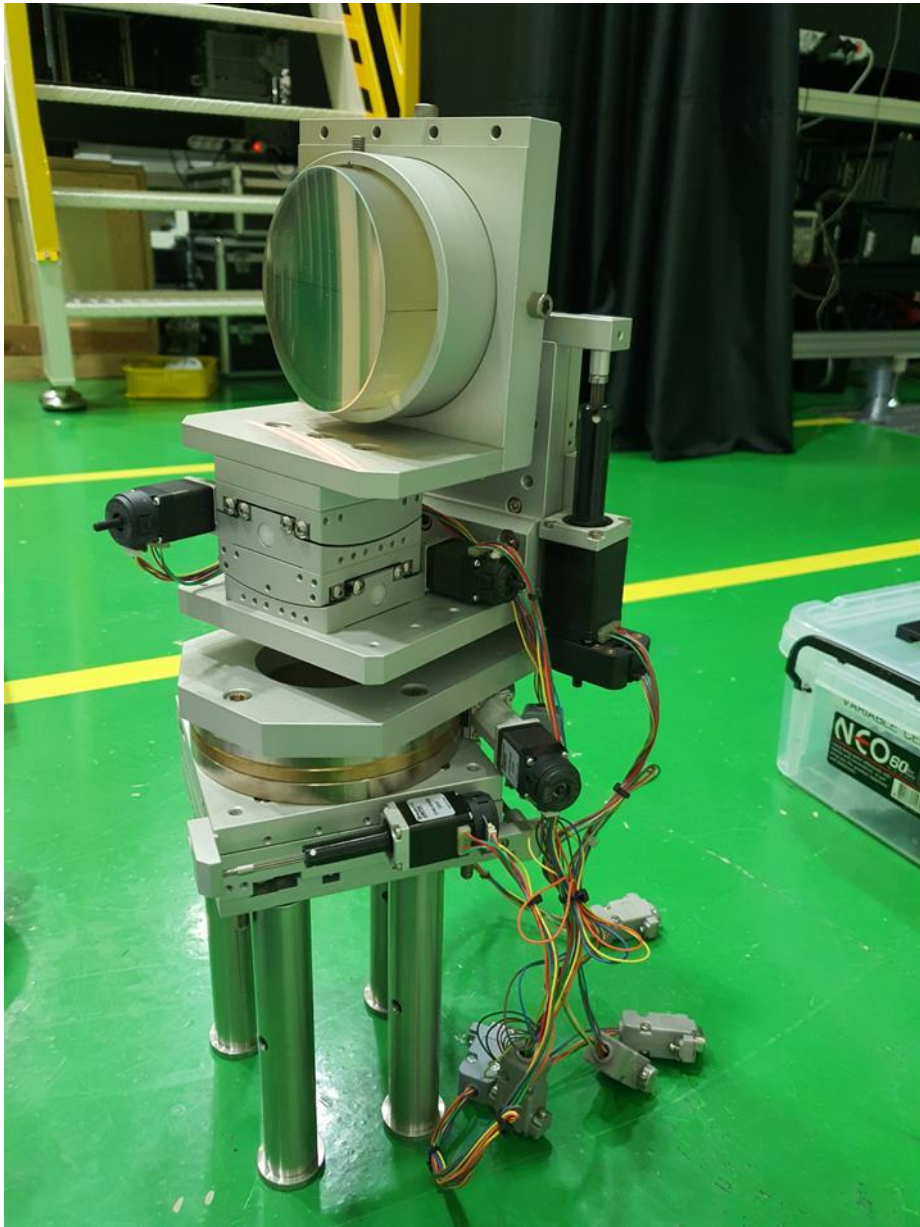
Figure 2.9: Off-axis parabolic mirror installed on a stage.

2.3. Generation of multi-GeV electrons

At CoReLS, ultra-relativistic electrons have been generated by the main driving laser using the laser wakefield acceleration (LWFA) scheme.

2.3.1. Laser wakefield acceleration

The principle of LWFA is to accelerate electrons by utilizing the large electric fields within a laser-produced plasma. The concept was first proposed in 1979 by Tajima and Dawson[39], but it was not possible to implement due to the lack of high-power lasers. With the development of high-power femtosecond lasers in the late 21th century[40, 41], LWFA became a reality and has since been widely adopted and developed by research groups worldwide[10, 42].

In this section, a principle of LWFA is briefly introduced using Figure 2.10. When a high-power laser is focused to a plasma, the laser beam exerts a ponderomotive force[43] on electrons and ions. Only the electrons are responsive to the ponderomotive force because of their low mass. As a result, the electrons are pushed out from the laser propagation axis. The remaining heavy ions form a positive charge bubble surrounded by the pushed-out electrons. As the electrons are pulled back by the charge separation force of the ions, this creates a wakefield structure along the laser propagation axis. When an electron bunch are trapped in the positive charge bubble (wakefield structure), they are accelerated towards the bubble center by a huge electric field of about hundreds of GV/m. At CoReLS, electrons with an energy of 2 − 3 GeV are generated

stably[44].
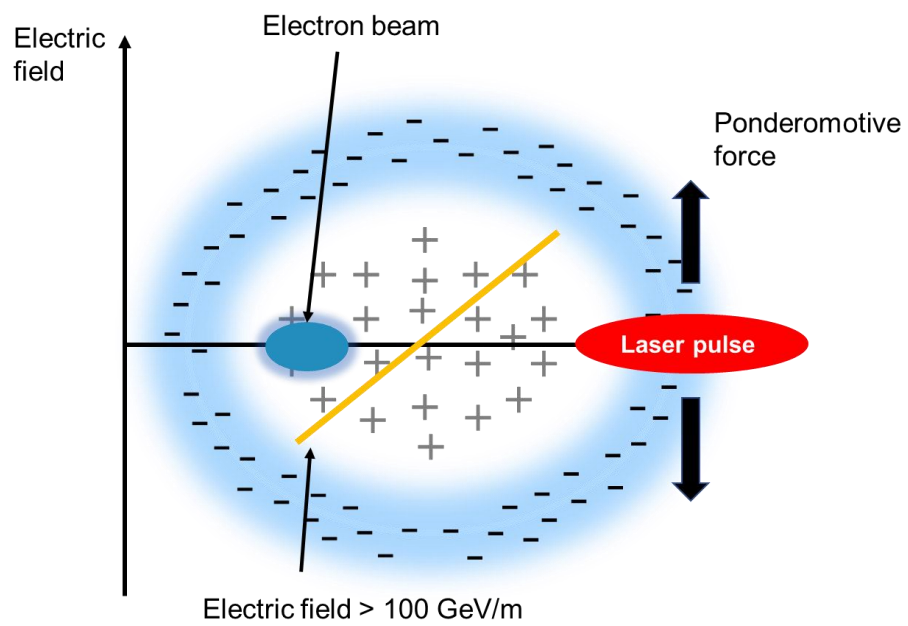
Figure 2.10: Schematics of the laser wakefield acceleration scheme.

2.3.2. Plasma density

Plasma density is a crucial parameter for electron acceleration using LWFA because it affects the dephasing and the depletion lengths that limit the acceleration length of electrons. In this experiment, a gas cell, shown in Figure 2.11, was used as a gas target of electron acceleration. The right side of the gas cell in Figure 2.11 b) was designed asymmetrically to allow it to be placed as close as possible to the scattering point without interfering with the scattering laser beam. On the other hand, the interior of the gas cell was symmetrically shaped with a size of 20 mm x 20 mm x 50 mm. The gas cell has entrance and exit holes with a diameter of 2 mm.
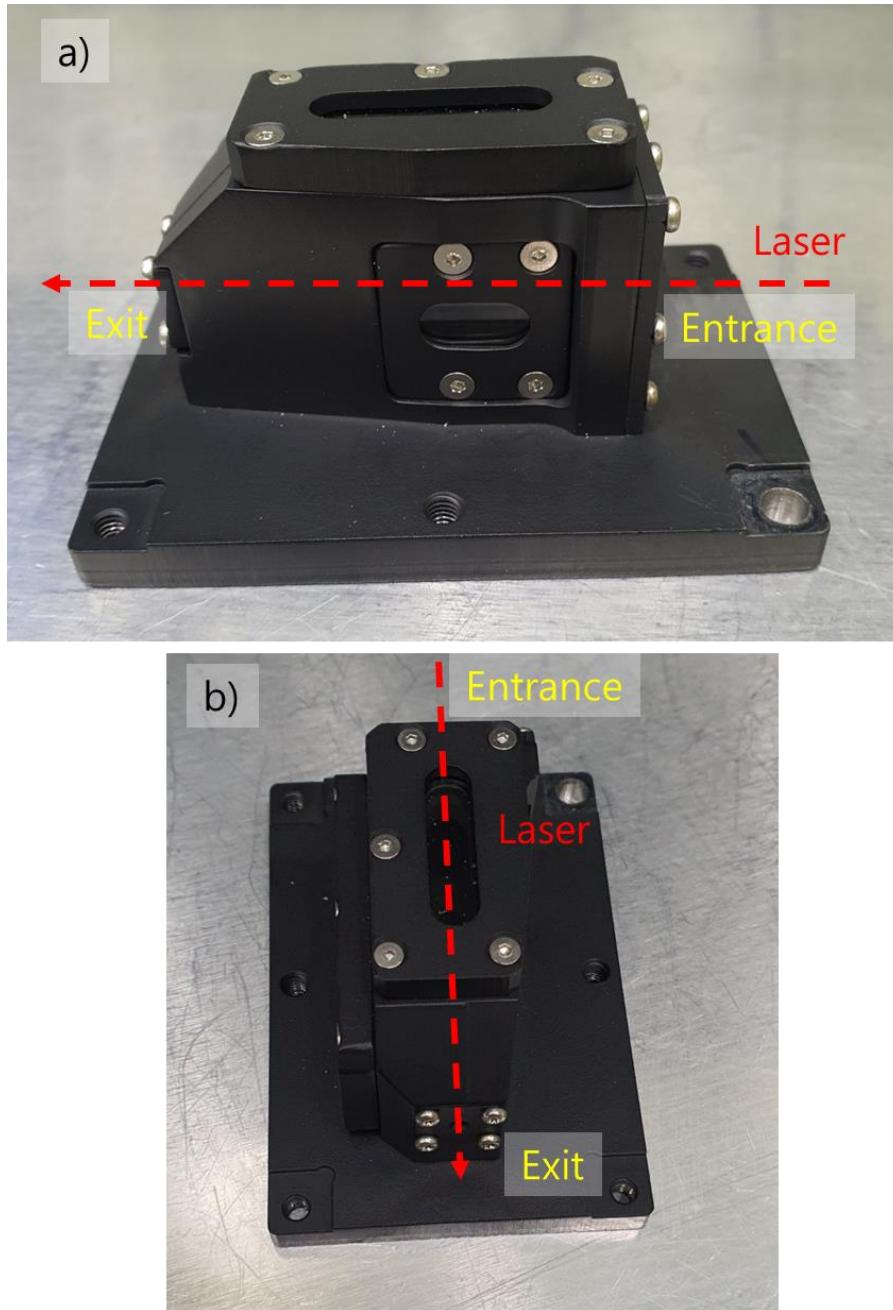
Figure 2.11: a) Photo of the gas cell of electron acceleration taken from the side. b) Photo taken from the top.

The gas injection system was built as shown in Figure. 2.12. The gas injection system consists of a gas cell, a gas reservoir, a Parker valve, a valve control device, a pressure control device, and a gas cylinder containing a mixture of 97% He and 3% Ne. The backing pressure of the Parker valve was managed by the pressure controller (CPC3000). The gas opening time and duration were adjusted by the valve controller (IOTA ONE). In this experiment, Parker valve was opened 25 ms prior to the laser injection by the valve controller. The reservoir and the gas cell were filled with the gas that entered through Parker valve.
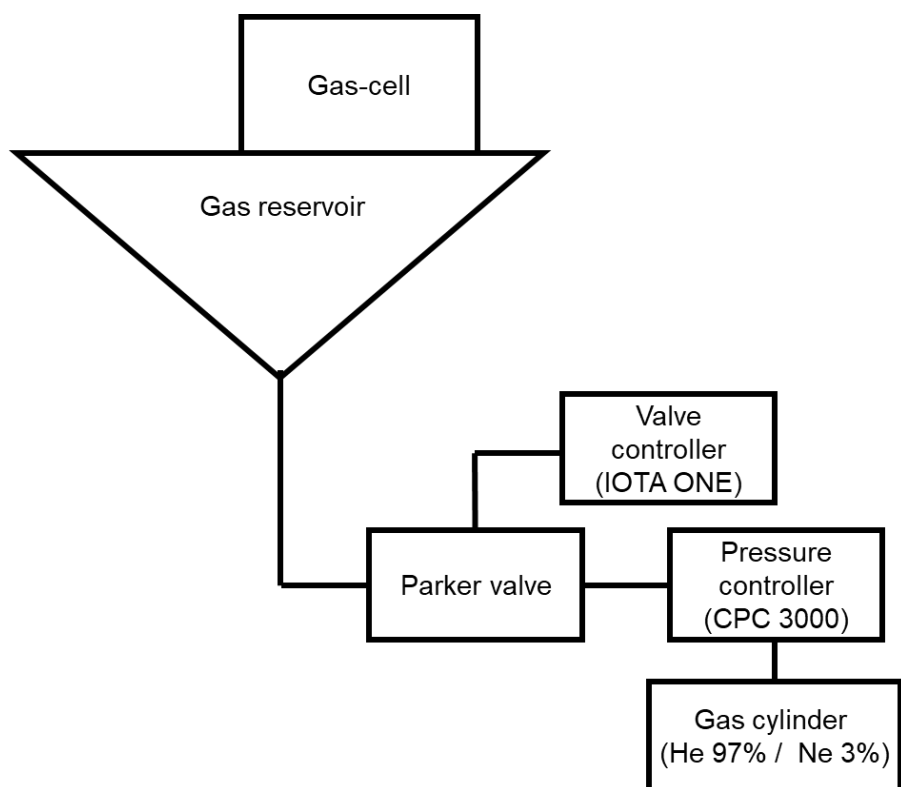
Figure. 2.12: Gas injection system consists of a gas cell, a gas reservoir, a Parker valve, a valve control device, a pressure control device, and a gas cylinder containing a gas mixture of 97% He and 3% Ne.
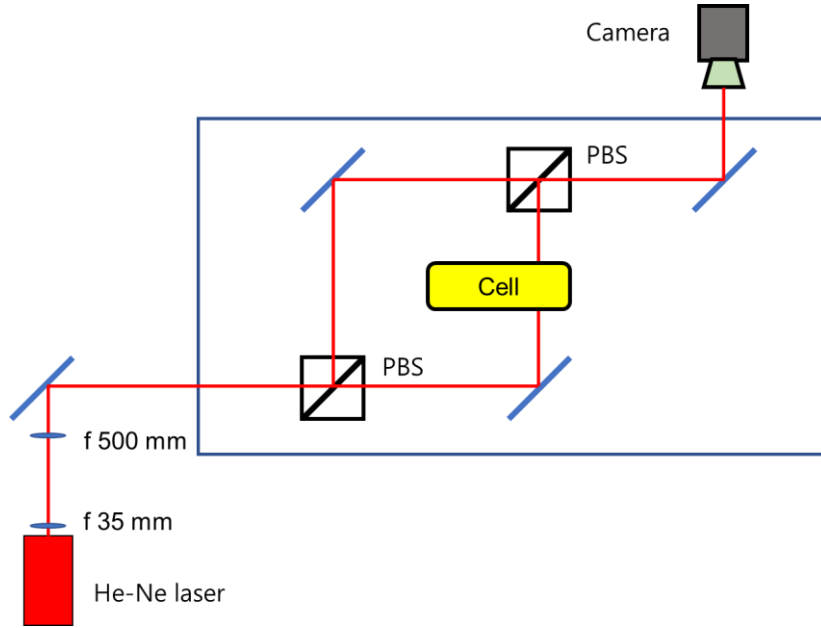
Figure 2.13: Schematics of a Mach−Zehnder interferometer consisting of a He−Ne laser, two lenses for magnification, two polarized beam splitters (PBS) and a camera.

The gas density inside the gas cell was measured using a Mach−Zehnder interferometer[45], as depicted in Figure 2.13. The interferometer consisted of a He−Ne laser, two lenses for magnification, two polarized beam splitters, and a camera (Basler, acA 1300−30gm). The camera measured the phase shift of the interference pattern when the gas cell was filled with gas. For example, Figure 2.14 shows the interference pattern compared to vacuum and gas filled using the gas injection system with a mixture of 97% He and 3% Ne gas, the backing pressure was set to 9 bar using the pressure controller and the Parker valve was opened 25 ms prior to the measurement by the valve controller.
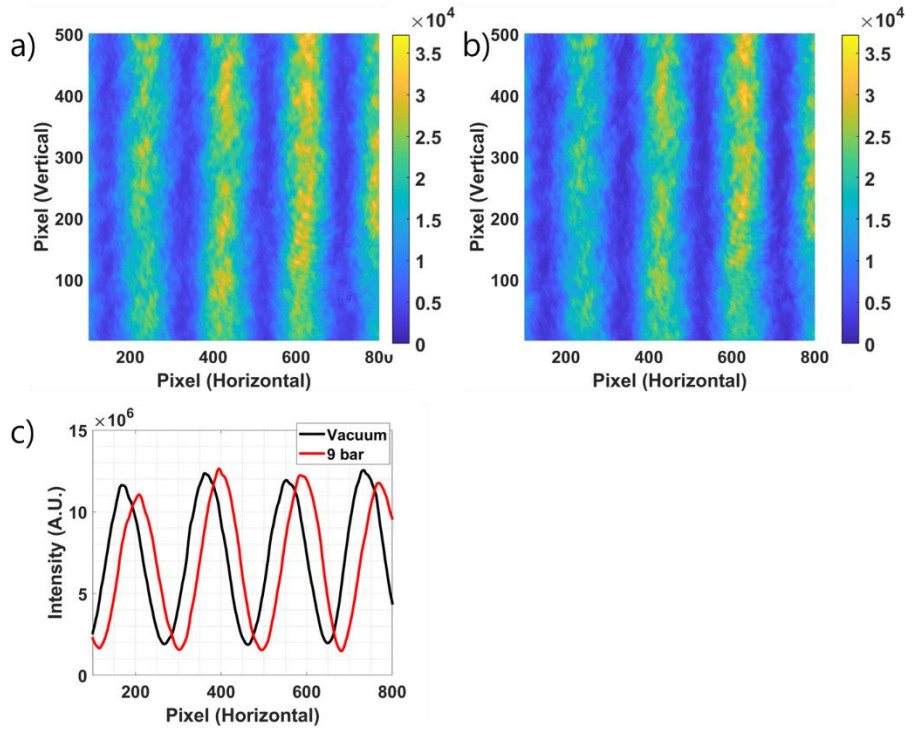
Figure 2.14: Interferograms of the gas cell a) in vacuum and b) with a gas mixture of 97% He and 3% Ne. c) Horizontal lineout of a) and b).

Here, the interference phase shift can be represented by the following equation[46]:

$$\Delta\phi = \omega\Delta t = 2\pi\frac{c}{\lambda}\Delta t = 2\pi\frac{c}{\lambda}(n-1)\times\frac{d}{c} \qquad (2.1)$$

where, $\Delta\varphi$ is a phase shift, ω is a wave frequency, Δt is a time lag, c is the speed of light, λ is a laser wavelength, n is a refractive index of gas and d is a lateral medium length of the gas cell. The gas density can be calculated from the interference phase shift of the interferometer by the formula:

$$\rho = \frac{\Delta\phi \cdot \lambda}{2\pi \cdot d \cdot (n_0 - 1)}\rho_0 \qquad (2.2)$$

where, n_0 is a refractive index of gas at 1 atm. ρ is a gas density and ρ_0 is a gas density at 1 atm. The gas density can be calculated by obtaining the phase shift. Figure 2.15 shows the measured gas density. The gas density was calculated by averaging the five repeated measurements to reduce the measurement error. The gas density was measured with backing pressures of 3, 6, and 9 bars in order to confirm the linearity between the backing pressure and the gas density, as shown in Figure 2.16.
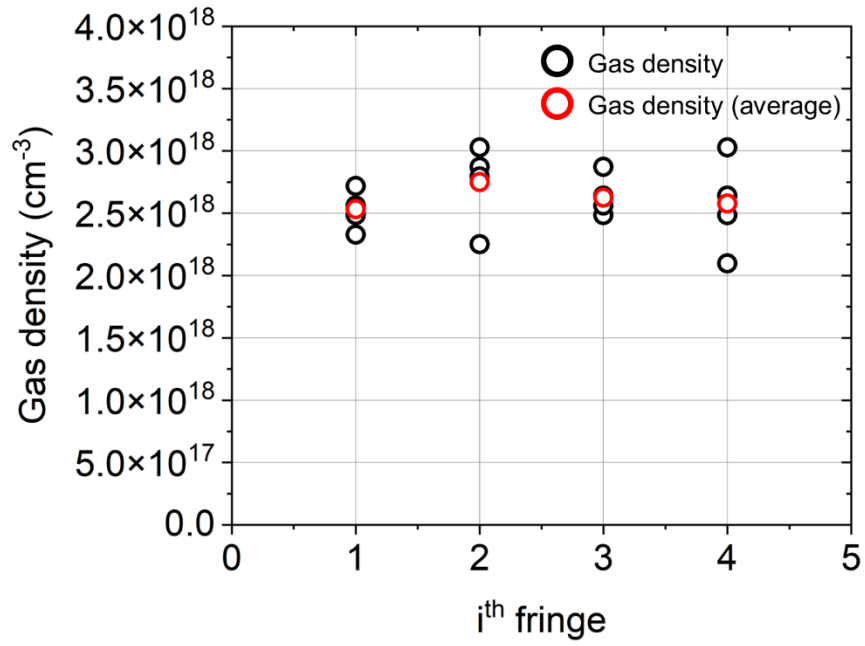
Figure 2.15: Gas density measured from the fringe shift shown in Figure 2.14. The ith fringe denotes the appearance order of intensity peaks in the interferogram. The black circles show the measured gas density from 5 measurements, while the red circles show the average gas density at each fringe position.
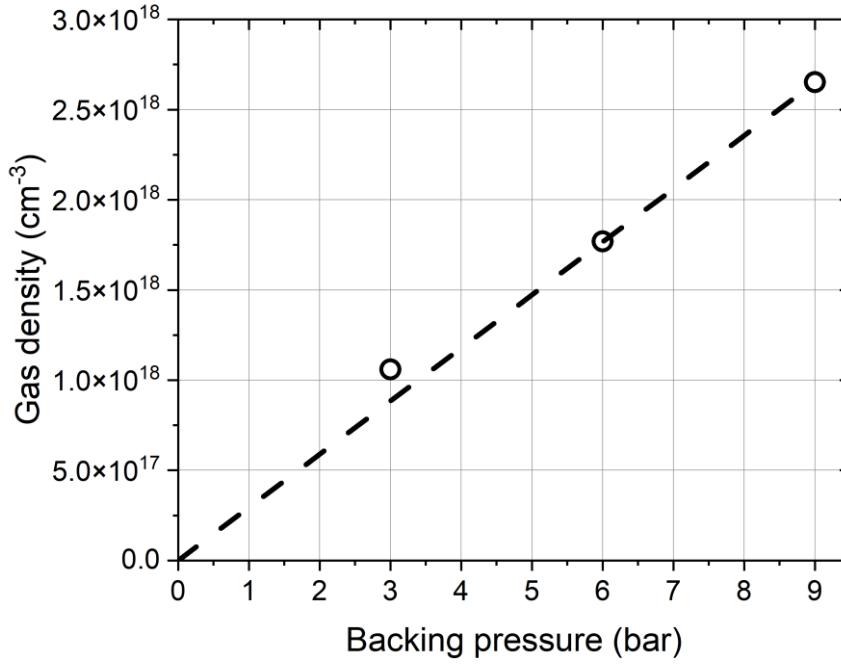
Figure 2.16: Dependence of gas density on backing pressure.

The gas mixture of 97% He and 3% Ne was used in the experiment. As He was fully ionized in the leading edge of the main laser, the electron density was two times the neutral gas density. As the target electron density was $7 \times 10^{17} cm^{-3}$, neutral gas density was set to $3.5 \times 10^{17} cm^{-3}$ under the condition of the backing pressure of $1.0 - 1.5$ bar.

2.3.3 Laser focusing position

The position of the focal spot within the gas cell affects the laser wakefield acceleration. In particular, electrons can be accelerated up to the dephasing length and the depletion length. To obtain the maximum energy of electrons, the distance that electrons travel in the plasma must be comparable to the dephasing and the depletion lengths. The starting position of electron acceleration in the gas cell and the travel distance of the electron in the plasma were controlled by adjusting the focus position of the main driving laser. In the experiment, the focal spot position was controlled by adjusting the defocus of the deformable mirror. By scanning the voltage of the deformable mirror during the experiment, the optimum focus position for generating electrons with energy over 2 GeV was obtained.

2.4. Spatiotemporal synchronization

In Compton scattering experiments, a precise spatiotemporal synchronization between the main driving laser beam and the scattering laser beam, ultimately converting into the synchronization between the electron and the scattering laser beams for collision, is an essential prerequisite. At the same time, the time delay between the two laser beams should be controlled to consider the inherent time delay between the main laser beam and the accelerated electron beam, which is about the light travel time of the bubble radius in the blowout regime. The spatial overlap of the two laser beams can be simply verified by measuring the centroids of two beams at the scattering point with a camera. For the temporal synchronization, various optical and electronic techniques can be utilized. In order to achieve an accurate temporal overlap, the resolution needs to be much shorter than the pulse duration of the laser. For laser pulses with a duration of tens of femtoseconds, optical techniques can be favorably employed, since the shortest resolution provided by electronic techniques is currently limited to about 200 fs[47].

Interferometric optical techniques are often employed to measure a time delay between two femtosecond laser pulses. In particular, spectral interferometry has been widely used due to its simplicity in data acquisition and analysis[48]. In this method, the time delay is determined from the period of the spectral interference fringe. This technique also allows to measure a time delay much longer than the pulse duration. On the other hand, spatial interferometry can be an

alternative that provides a narrow temporal range comparable to the pulse duration. From the visibility measurement of spatial interference fringes, the temporal overlap between two laser beams could be characterized. Hence these optical techniques are frequently adopted to measure and control the temporal overlap and delay. It is noted that it is very difficult to maintain a fixed time delay within tens of femtoseconds in an experiment requiring a long optical path length because of several external factors including mechanical vibration and temperature variation. As a result, the time delay needs to be monitored in real time in order to control the time delay and correct any temporal shifts occurring during scattering experiments [49].

2.4.1. Theory

2.4.1.1. Spatial interference

The interference of two spatio−temporally overlapped waves was considered to find out the time delay from the fringe visibility. When two light pulses with Gaussian intensity profiles, $I_1(t)$ and $I_2(t)$, are overlapped, the total intensity, $I(t)$, is given by

$$I(t) = I_1(t) + I_2(t)$$
$$+2\sqrt{I_1(t)I_2(t)} \cos (k_1 r_1 - k_2 r_2 - w_1 t_1 + w_2 t_2 + \phi_1 - \phi_2)$$

(2.3)

with $I_1(t) = A_1 \exp (-\frac{(t-T_1)^2}{2\sigma_1^2})$ and $I_2(t) = A_2 \exp (-\frac{(t-T_2)^2}{2\sigma_2^2})$.

Here k is a wave vector, r a displacement vector, w a wave frequency, ϕ a phase constant, A an amplitude of the light pulse, T the time of peak intensity, and $2\sqrt{2 \ln 2} \sigma$ a pulse width (FWHM). The visibility, η, of the interference fringe is, then, given by

$$\eta = \frac{I_{max} - I_{min}}{I_{max} + I_{min}} = \frac{\int 2\sqrt{I_1(t)I_2(t)}dt}{\int [I_1(t) + I_2(t)]dt} = C\exp\left(-\frac{(\Delta t)^2}{2 \cdot \sigma'^2}\right) \quad (\,2.4\,)$$

with $I_{max} = \int [I_1(t) + I_2(t) + 2\sqrt{I_1(t)I_2(t)}]\,dt$,

and $I_{min} = \int [I_1(t) + I_2(t) - 2\sqrt{I_1(t)I_2(t)}]\,dt$.

Here C is a constant, $\sigma' = \sqrt{2(\sigma_1^2 + \sigma_2^2)}$ and Δt is a time delay of $T_2 - T_1$. It shows that the visibility takes the form of a Gaussian distribution, of which the temporal center is zero. By rearranging Eq. 2.4 in terms of Δt, the absolute time delay between two beams is given as,

$$|\Delta t| = \sqrt{2\sigma^2 \ln(C/\eta)} \quad (\,2.5\,)$$

By plotting the time delay with respect to the fringe visibility, the time delay can be obtained by setting the zero time delay at the maximum visibility.

2.4.1.2. Spectral interference

The interference of two waves in the spectral domain is considered for the measurement of a long time delay. When two beams are overlapped spatially, the total spectral intensity can be written as

$$I(f) = I_1(f) + I_2(f) + 2\sqrt{I_1(f)I_2(f)}\cos(2\pi\Delta t \cdot f + \phi) \quad (\,2.6\,)$$

where f is a frequency and ϕ is a phase difference of $\phi_1 - \phi_2$. When I(f) is Fourier-transformed to the time domain, a spectrum which corresponds to the interference term, $2\sqrt{I_1(f)I_2(f)}\cos(2\pi\Delta t \cdot f +$

ϕ), is formed and the peak of this spectrum indicates the time delay. In order to extract the time delay from the interference term, the constant terms from $I_1(f)$ and $I_2(f)$ have to be removed from the data taken at a time delay Δt_{far} outside the temporal overlap of two beams. And $[I_{\Delta t}(f) - I_{\Delta t_{far}}(f)]$ is Fourier−transformed as,

$$F_f\left[I_{\Delta t} - I_{\Delta t_{far}}\right](t)$$

$$= F_f[2\sqrt{I_1 I_2}(\cos(2\pi\Delta t \cdot f + \phi) - \cos(2\pi\Delta t_{far} \cdot f + \phi))](t)$$

$$= e^{-i\phi} \times F_f\left[\sqrt{I_1 I_2}\right](t - \Delta t) + e^{i\phi} \times F_f\left[\sqrt{I_1 I_2}\right](t + \Delta t) - e^{-i\phi} \times$$

$$F_f\left[\sqrt{I_1 I_2}\right](t - \Delta t_{far}) - e^{i\phi} \times F_f\left[\sqrt{I_1 I_2}\right](t + \Delta t_{far}).$$

(2.7)

At the delay region of interest, $F_f\left[\sqrt{I_1 I_2}\right](t \pm \Delta t_{far})$ terms are negligible. If $I_1(f)$ and $I_2(f)$ are close to a Gaussian distribution, an absolute value of $F_f\left[I_{\Delta t} - I_{\Delta t_{far}}\right](t)$ can be written as

$$abs\left[F_f\left[I_{\Delta t} - I_{\Delta t_{far}}\right](t)\right]$$

$$\approx C\left[\exp\left(-\frac{(t-\Delta t)^2}{2\left(\frac{1}{2\sqrt{2\pi}\sigma_f}\right)^2}\right) + \exp\left(-\frac{(t+\Delta t)^2}{2\left(\frac{1}{2\sqrt{2\pi}\sigma_f}\right)^2}\right)\right],$$

(2.8)

where C is a constant, $\sigma_f = \sqrt{\frac{\sigma_{f1}^2 \sigma_{f2}^2}{\sigma_{f1}^2 + \sigma_{f2}^2}}$ and a spectral width (FWHM) of $I_1(f) (I_2(f))$ is given as $2\sqrt{2\ln 2}\,\sigma_{f1}\,(\sigma_{f2})$. Now, the time delay can be determined by fitting $abs\left[F_f\left[I_{\Delta t} - I_{\Delta t_{far}}\right](t)\right]$ as a convolution of two Gaussian distribution functions. To distinguish two Gaussian distribution functions, Δt should be large enough to satisfy the Rayleigh criterion, resulting in the condition, $2 \times \exp(-4\pi^2 \sigma_f^2 \Delta t^2) < 0.8$. Consequently, the time delay can be obtained for the temporal region satisfying the condition, $|\Delta t| > \frac{\sqrt{\ln 2.5}}{2\pi\sigma_f} \approx \frac{0.15}{\sigma_f}$.
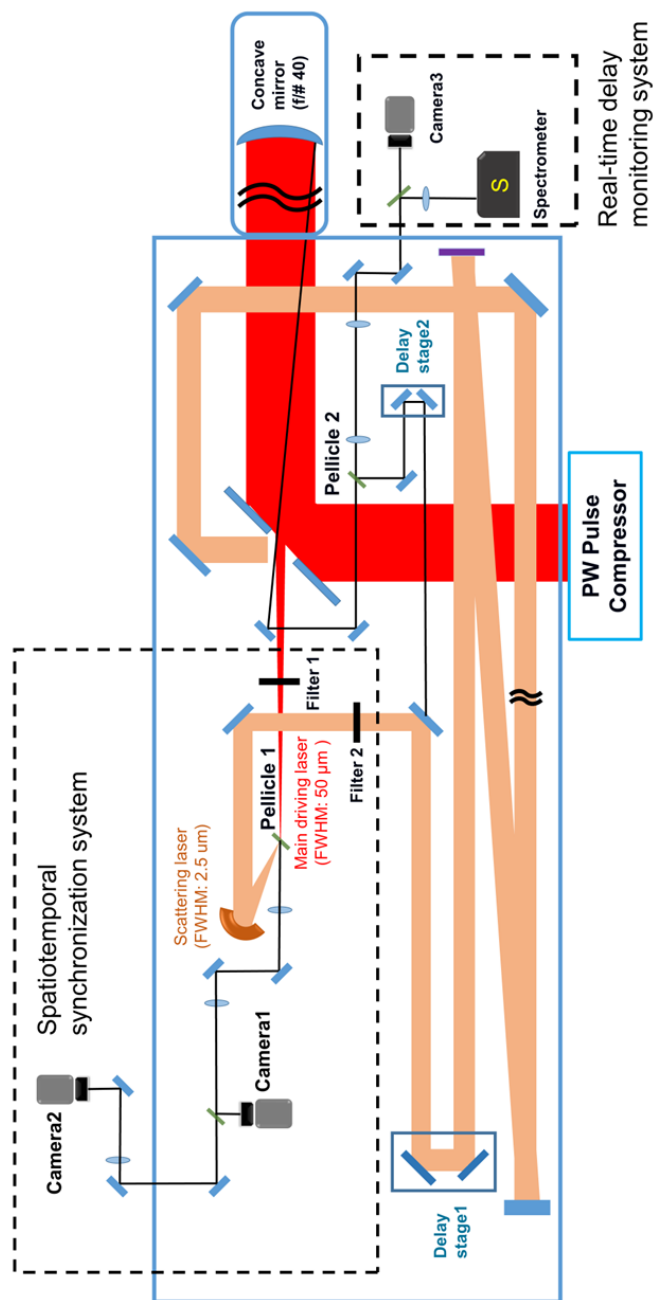
Figure 2.17: Experimental layout of the spatiotemporal synchronization between two laser beams – the main driving laser for electron acceleration and the scattering laser for scattering.

2.4.2. Spatiotemporal synchronization setup

A spatiotemporal synchronization setup was installed to check the spatiotemporal overlap between the main driving laser beam for electron generation and the second laser beam for scattering. The main driving laser beam with a pulse width of 25 fs (FWHM) and a spot size of 50 μm (FWHM) was used to generate a high−energy electron beam in a gas cell (not shown) using the laser wakefield acceleration scheme. And the scattering laser beam had the same pulse width of 25 fs (FWHM) and a tightly focused spot size of 2.5 μm (FWHM) at the scattering point. The synchronization system consists of a pellicle beam splitter, lenses, filters, two cameras and a delay stage, as shown in Figure 2.17. The scattering beam was focused at the first pellicle beam splitter (Pellicle 1) located at the scattering position (30 mm away from gas cell exit) and reflected to the propagation direction of the main beam. Here neutral density filters (Filter 1 and Filter 2) with the same thickness were inserted in the main and in the scattering laser beam paths to prevent the damage of Pellicle 1 by the focused laser beams. An image at the scattering position was magnified three times and relayed to the camera 1 (EPIX, SV10M6) with 1.67−μm pixels, while an image plane after the first lens was relayed to the camera 2 (PCO, Pixelfly usb) with 6.45−μm pixels. The main beam was first aligned to make spatial centroids of two beams coincide at the camera 1, and then Pellicle 1 was tilted minutely to make the centroids coincide at the camera 2. Here the spatial synchronization of two beams at Pellicle 1 (the scattering point) was measured with an uncertainty of 0.6 μm.

A spatial interferogram of two beams measured with the camera 2 was utilized to verify the temporal synchronization. Only when the time delay between two beams was within ±55 fs, the interferogram with a circular form was visible and its visibility changed according to the time delay, as shown in Figure 2.18(a) and (b). Here the optical time delay (Δt_{stage}) was adjusted by moving the first delay stage (Delay stage1), and the whole interferograms were measured over the course of several minutes with a low−energy laser beam operating at 5 Hz to minimize the time delay shift due to temperature variation. The red solid line in Figure 2.18 2(b) indicates the Gaussian fitting of the 5−shot−averaged visibility at each delay, which is given as

$$\eta' = 0.40 \times \exp\left(-\frac{\Delta t^2}{2 \times 23.5^2}\right) + 0.32 \qquad (2.9)$$

Here, η' has a form of Eq. 2.4 with the background of 0.32 originating from the non−uniform spatial profile of the main driving laser beam. Using Eq. 2.9, the absolute measured time delay (Δt_{mea}) can be expressed as follow:

$$|\Delta t_{mea}| = \sqrt{2 \times 23.5^2 \times \ln\frac{0.40}{(\eta' - 0.32)}} \ (fs) \qquad (2.10)$$

From Eq. 2.10, the visibility could be converted into the time delay, as shown in Figure 2.18(c). The error of Δt_{mea} ($\sqrt{\frac{\sum_{i=1}^{n}(\Delta t_{mea}-\Delta t_{stage})i^2}{n}}$, $\Delta t_{stage} \leq 33 \ fs$) was 11 fs in RMS. This error originated from the jitter of time delays, coming from beam pointing fluctuations. Consequently,

the zero time delay was set to the time of the maximum visibility, $\eta' = 0.72$, with a jitter of 11 fs.
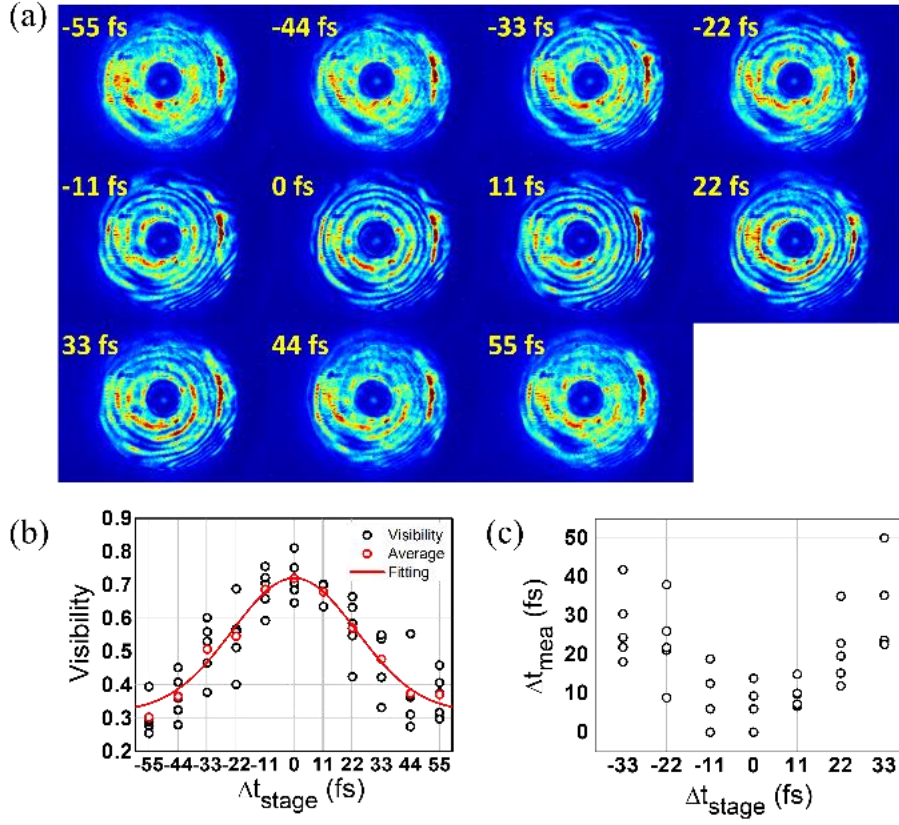
Figure 2.18: (a) Interferograms measured with the camera 2 while changing Δt_{stage}, as indicated in the interferograms. (b) Black circles at each Δt_{stage} indicate the visibility obtained from the interferograms. The red square represents an average visibility at each delay. The red solid line is the Gaussian fitting of red squares. (c) Δt_{mea} was calculated from the visibility in (b) using Eq. 2.10.

2.4.3 Real-time delay monitoring system

The real-time delay monitoring setup was installed to check the time delay during a scattering experiment. As shown in Figure 2.17, a small portion of the main driving laser beam was picked off with a small plane mirror placed at the bottom edge of the concave mirror, and was combined with the leakage beam of the scattering laser beam at the pellicle beam splitter 2 (Pellicle 2). After the combination of two laser beams, they were relayed to a fiber spectrometer (Ocean Optics, HR4000CG) and the camera 3 (PCO, Pixelfly usb) to measure a spectral interference signal and a spatial interferogram, respectively. Here the fiber spectrometer had a 0.25-nm resolution, corresponding to a 10-fs resolution in the Fourier-transform domain. After achieving the temporal overlap of the main beam and the scattering beam with the spatiotemporal synchronization setup, the zero-delay setting in the real-time delay monitoring setup was defined by adjusting the time delay of the leakage scattering beam using the second delay stage (Delay stage2). Finally, the actual time delay at each shot during an experiment was obtained in real time from the spectral interference signal and the spatial interferogram.

2.4.3.1 Spatial interferometry

The time delay shorter than 30 fs between the two beams was identified by measuring the visibility of the spatial interferogram on the camera 3. Figure 2.19(a) shows the interferograms measured while scanning Δt_{stage} of the scattering beam with Delay stage 1.

Here, the shape of the interference fringes was not circular but rectilinear because two collimated beams were slightly misaligned intentionally in the horizontal direction to clearly measure the interference fringes. Figure 2.19 (b) shows that the visibility changes with Δt_{stage}. The red solid line is the Gaussian fitting of the average visibility, corresponding to

$$\eta' = 0.63 \times \exp\left(-\frac{\Delta t^2}{2 \times 14.3^2}\right) + 0.12 \qquad (\,2.11\,)$$

Using Eq. 2.11, the absolute delay is expressed as

$$|\Delta t_{mea}| = \sqrt{2 \times 14.3^2 \times \ln\frac{0.63}{(\eta' - 0.12)}} \; (fs) \qquad (\,2.12\,)$$

By using Eq. 2.12, the visibility could be converted into time delay, as shown in Figure 2.19 (c). The error of Δt_{mea} was 6 fs in RMS. This error was smaller than that of the spatiotemporal synchronization setup. Because two beams were overlapped in a non−focusing geometry, the pointing fluctuation is smaller than that in the spatiotemporal synchronization setup. Consequently, the time delay between 0 and 30 fs was monitored using the spatial interferometer in real time with the jitter of 6 fs.
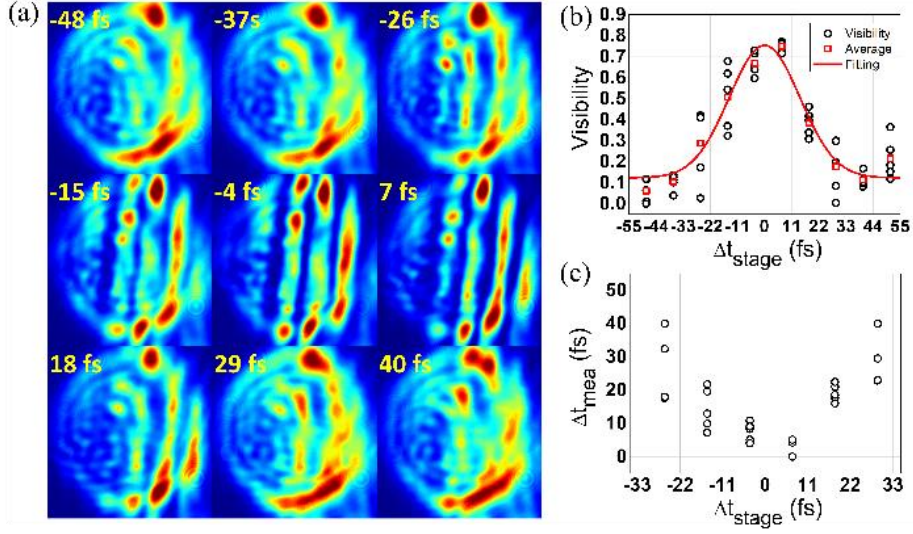
Figure 2.19: (a) Interferograms measured with the camera 3 while controlling Δt_{stage} with Delay stage 1, as indicated with the interferograms. (b) The black circles at each Δt_{stage} show the visibility obtained from the interferogram measured five times. The red square represents an average visibility at each delay. The red solid line is the Gaussian fitting of the red circle data. (c) Δt_{mea} calculated from the visibility in (b) using Eq. 2.12.

2.4.3.2. Spectral interferometry

A long time delay between the two laser beams was monitored by using the spectral interference signal measured with a spectrometer. In a scattering experiment, the scattering laser beam collides with a multi−GeV electron beam driven by the main driving laser. Here its time delay needs to be controlled up to a−few−hundred fs, because the group velocity of the driving laser propagates in plasma is less than the speed of light and the time lag of multi−GeV electrons from the driving laser depends the bubble size of laser wake field acceleration. It is thus necessary to measure the time delay from 20 fs ($\approx \frac{0.15}{\sigma_f}$) to 200 fs by analyzing the spectral interference signal. For this analysis, an interference term should be distinguished in the Fourier transformed domain. The spectral interference signal at the time delay of 300 fs was first measured for the background subtraction. As shown in Figure 2.20 (a) and (b), spectral interference signals were measured at several time delays and their Fourier−transformed signals ($F_f[I_{\Delta t} - I_{\Delta t=300\,fs}](t)$) were obtained. Each red dashed line in Figure 2.20 (b) indicates the Gaussian fitting of the Fourier−transformed signal, and the actual time delay was obtained from the central value of the Gaussian distribution. Because the spectral intensity of the laser beam was close to a Gaussian function, $F_f[I_{\Delta t} - I_{\Delta t=300\,fs}](t)$ fitted well with a Gaussian function. As a result, Δt_{mea} matched each Δt_{stage} well, as shown in Figure 2.20 (c). Here the error of Δt_{mea} was 7 fs in RMS. The resolution of the spectrometer, 10 fs, could be improved slightly through the Gaussian fitting. Co

nsequently, in the range between 20 fs and 200 fs, the time delay m
easurement was demonstrated with the jitter of 7 fs.
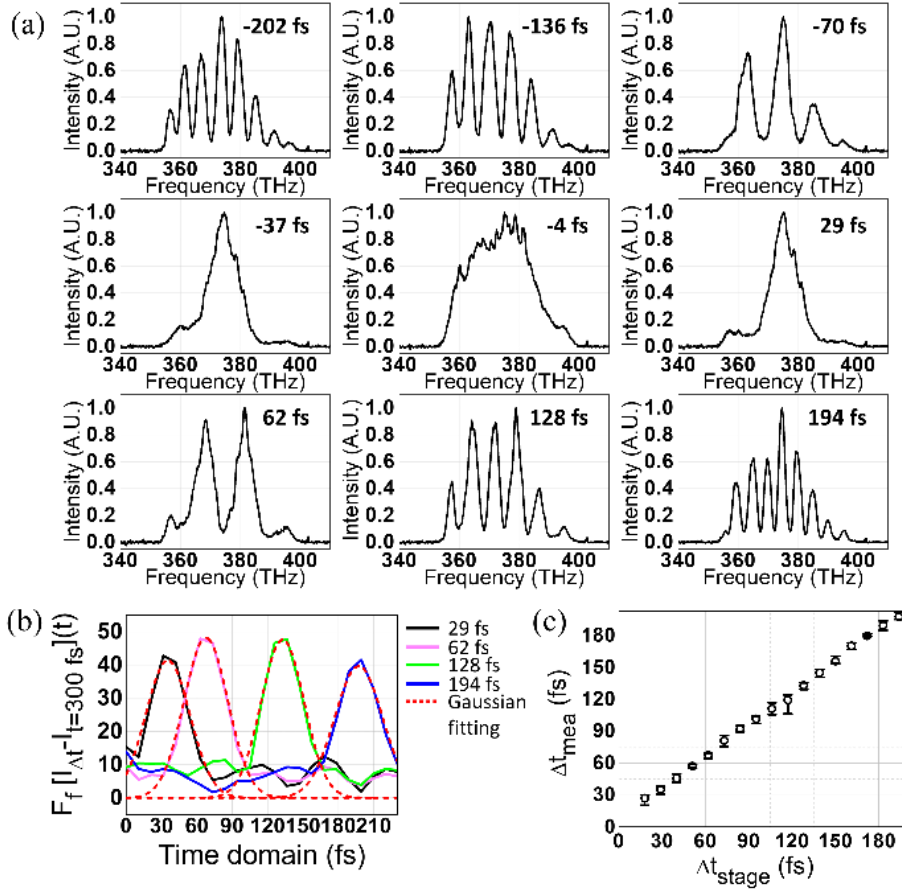
Figure 2.20: (a) Spectral interference signals obtained by changing Δt_{stage} with Delay stage 1. (b) Fourier-transformed signals of the spectral interference signals shown for four time delays of 29 fs (black), 62 fs (magenta), 128 fs (green), and 194 fs (blue). The red dashed lines show the Gaussian fittings. (c) Linear variation of Δt_{mea} with Δt_{stage} set by Delay stage 1. The error bars correspond to the maximum and minimum values of Δt_{mea} among five repeated measurements at each Δt_{stage}.

4 4

2.4.4. Time delay control during Compton scattering experiments

A series of NCS experiments was carried out at CoReLS to examine strong field quantum electrodynamics processes through the scattering between a multi-GeV electron beam, driven by the main driving laser, and an ultrahigh intensity scattering laser. Before the experiment, the temporal synchronization between the main driving laser and the scattering laser beams using the spatiotemporal synchronization setup was set. Then, Pellicle 1, Filter 1 and Filter 2 were removed, and the time delay during an experiment was measured using the real-time delay monitoring setup.

For the successful operation of Compton scattering experiments the time delay was monitored in every shot. The measurement result of Δt_{mea}, along with Δt_{stage}, for 37 consecutive shots taken for an hour is shown in Figure 2.21 (a), and the difference between Δt_{stage} and Δt_{mea}, corresponding to the time delay shift, is shown in Figure 2.21 (b). The time delay shift came from the pointing fluctuations and the temporal jitter of two beams and the thermal expansion of optical mounts and boards. Especially, the thermal expansion of the optical board with the time delay line for the scattering laser can cause a time delay shift of tens of femtosecond. The optical path length of the scattering laser beam was sensitive to the thermal expansion of an optical board because it had a long optical path over 20 m on the optical board to make its path length the same as the main beam path with the 12-m focusing mirror. For the small temperature variation of 0.01 ℃ the aluminum optical board, with the linear thermal

expansion coefficient of $0.23\mu m/(m\,℃)$, could change 4.6 μm length, comparable to the time delay shift of about 15 fs. In order to test how precisely the time delay can be controlled in the scattering experiment, the time delay of 60 fs was intended for the shots from 18 to 37 in Figure 2.21. In this case, Δt_{stage} was adjusted to compensate for the time delay shift. As shown in Figure 2.21 (a), Δt_{mea} was maintained with the standard deviation of 14 fs for 20 consecutive shots. As a result, eight gamma-ray signals by the NCS were obtained among 20 consecutive shots. The slow oscillation of the time delay shift in Figure 2.21 (b) mainly came from the temperature variation in the laser room. As a result, the introduction of the real-time delay monitoring system made it possible to control the time delay with a precision of 14 fs during the scattering experiment, and the success rate of Compton scattering experiments became as high as 40%.
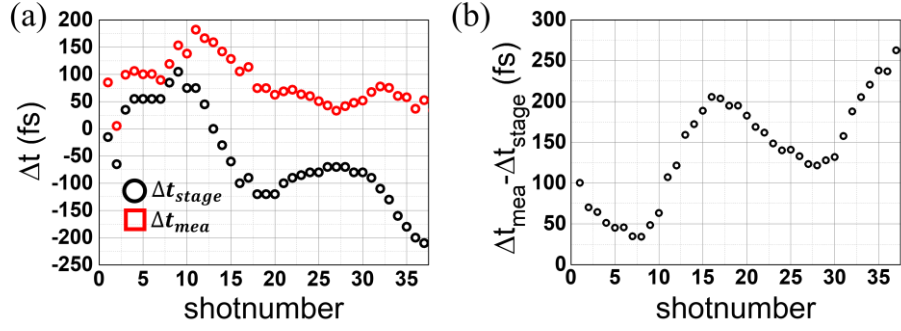
Figure 2.21: (a) Δt_{stage} (black circle) and Δt_{mea} (red square) of 37 consecutive shots taken for an hour during a scattering experiment. For the 20 shots after the shot number 18, Δt_{stage} was adjusted to maintain Δt_{mea} of 60 fs. (b) Time delay difference between Δt_{stage} and Δt_{mea}, showing the time delay shift during the experiment.

2.5. Diagnostics

In order to understand the physical process of Compton scattering, it is necessary to measure the beam profile and energy spectrum of electrons and of gamma rays from NCS. The layout of the diagnostics for gamma rays and electrons is shown in Figure 2.22. The multi-GeV electron beam accelerated by laser wakefield acceleration follows the propagation axis of the main driving laser. As the electrons pass through the dipole magnet of the electron spectrometer, their trajectory changes depending on energy. Lanex 1, a scintillation screen, was installed before the magnet to measure the electron beam profile. Lanex 2 and 3 were installed after the magnet to measure the spectral image of dispersed electrons. The energy spectrum can be retrieved after calibrating the trajectory with respect to electron energy. For gamma-ray measurements, a single crystal LYSO (LYSO-SC) and a pixelated LYSO (LYSO-PX) were installed after Lanex 3 to measure the gamma-ray profile and the energy spectrum, respectively.
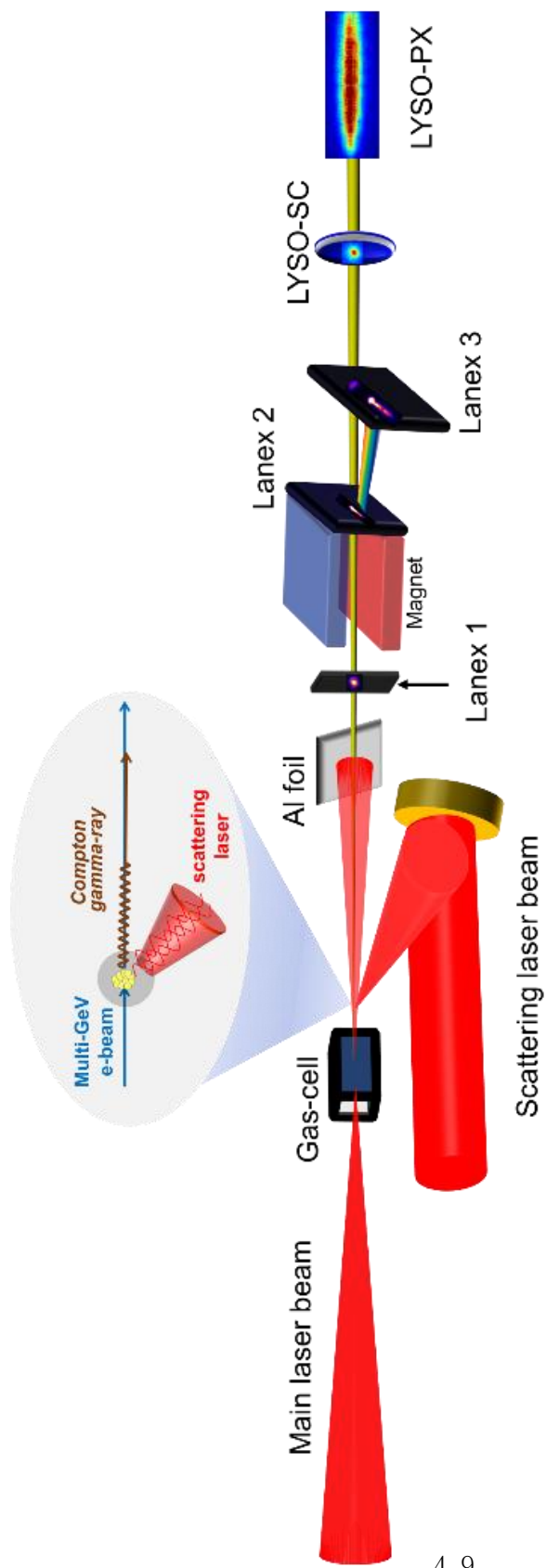
Figure 2.22: Schematics of Compton scattering setup showing the diagnostics for electron and gamma ray. Lanex 1 measures the electron beam profile. Lanex 2 and 3 are used to measure the electron energy spectrum. Lanex 2 and 3 are used to measure the electron energy spectrum. Lanex 2 measures the gamma−ray profile. The pixelated LYSO (LYSO−PX) measures the stored energy at each pixel during the propagation of the gamma−ray beam.

2.5.1. Electron measurement

Lanex, a scintillation screen, is widely used to measure an electron beam profile and an energy spectrum in LWFA research [50, 51]. The electron beam profile is measured by Lanex 1 (KODAC, Lanex Fine), installed 830 mm from the gas−cell exit along the main driving laser propagation axis. A camera (PCO, PCO.Edge) detected the scintillated light. Figure 2.23 shows the photo of Lanex 1 with marked dots for calibration. The distance between adjacent dots is 1 cm. The Lanex 1 is placed at 45 degrees to the laser propagation axis. The central dot indicates the beam axis and the left, right, up, and down sides are written as L, R, U, and D, respectively. Here, a pixel size of the camera is 46 μm by 65 μm in vertical and horizontal directions, respectively. Considering the distance between the gas−cell exit to Lanex 1, the pixel size is converted to 55 *μrad* vertically and 78 μrad horizontally. A band−pass filter (FES0650) was placed in front of the camera to reduce the stray light.
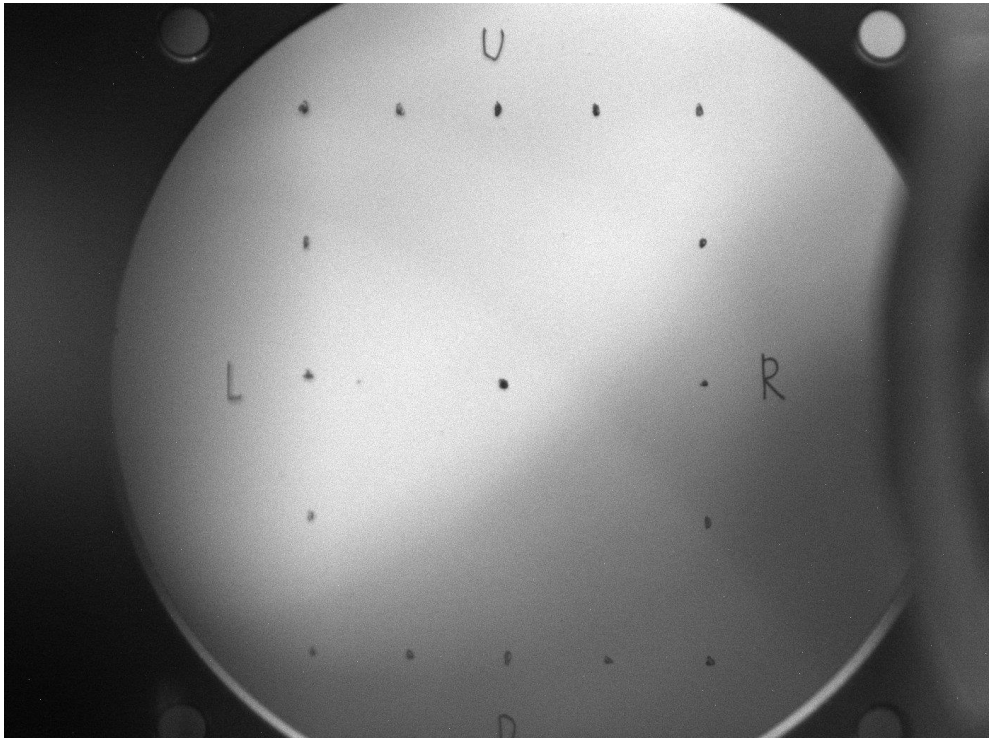
Figure 2.23: Photo of Lanex 1 marked with calibration dots. The distance between the dots is 1 cm. The central dot indicates the beam axis. The left, right, up, and down sides are also marked as L, R, U, and D, respectively.

The dipole magnet has a gap size of $30 \times 30 \times 1\ cm$, a magnetic field of 1.3T, and the magnetic field direction is perpendicular to the laser propagation direction. The magnet was installed 880 mm away from the gas−cell exit in order to measure the electron energy spectrum. Incident electrons to the magnet are dispersed, following energy− dependent trajectories. Lanex 2 (KODAC, Lanex Fast) was installed at the magnet exit, and Lanex 3 (KODAC, Lanex Fast) was installed 1180 mm away from the magnet. The energy of electrons was obtained, based on the calculation of electron trajectory[52], as shown in Eq. 2.13:

$$X = L\tan(\theta) + \rho \left[\cos(\theta) - \sqrt{1 - \left(\frac{D}{\rho} + \sin(\theta) \right)^2}\ \right]$$

$$+ \frac{F\left(\frac{D}{\rho} + \sin(\theta) \right)}{\sqrt{1 - \left(\frac{D}{\rho} + \sin(\theta) \right)^2}}\ , \qquad\qquad (\ 2.13\ )$$

where $\rho = \frac{m_0 c \beta \gamma}{eB}$

The spectral image on Lanex 2 was recorded with an ICCD (Princeton Instruments, PI−MAX4) and that on Lanex 3 was obtained with an EMCCD (Andor, iXon Ultra 888). Figure 2.25 and Figure 2.26 show the photos of Lanex 2 and Lanex 3, respectively. For the Lanex 2, a pixel size of the camera corresponded to 63 μm. Considering the distance between gas−cell exit and Lanex 2, the pixel size is converted to 53 μrad. For the Lanex 3, a pixel size of the camera corresponded to 139 μm vertically and 226 μm horizontally. Considering the distance between the gas−cell exit and Lanex 3, the pixel size is converted to 67 μrad vertically and 110 μrad horizontally. A band−pass filter (FES0650) was placed in front of both cameras

to reduce the stray light.
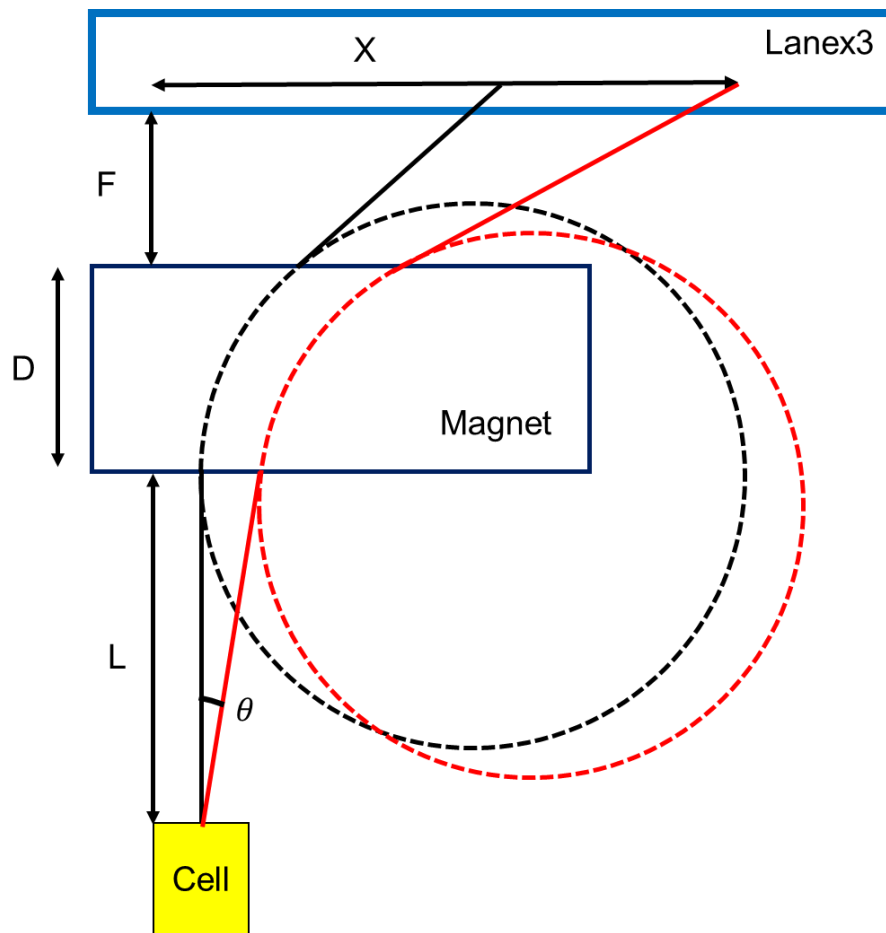
Figure 2.24: Schematics for calculating the electron energy from an electron trajectory deflected by the magnet.
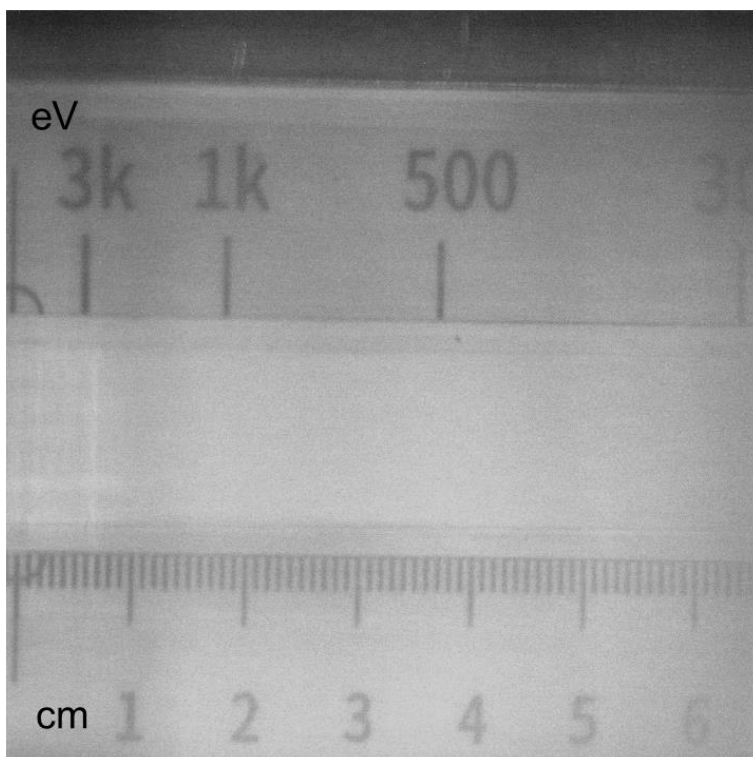
Figure 2.25: Photo of Lanex 2.
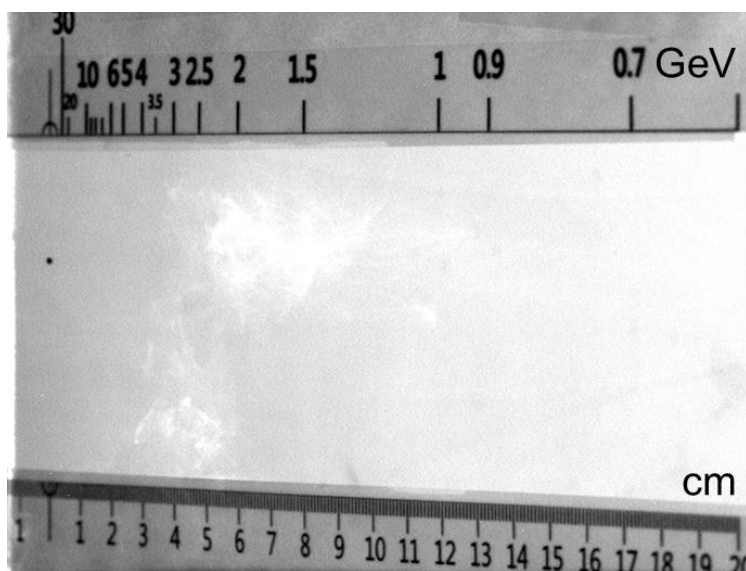
Figure 2.26: Photo of Lanex 3.

2.5.2. Gamma-ray measurement

Gamma rays from NCS was detected using two kinds of LYSO scintillation crystals – LYSO-SC and LYSO-PX. LYSO-SC, a single crystal plate, was prepared for the measurement of the beam profile of NCS gamma rays. The diameter of LYSO-SC was 90 mm and the thickness was 5 mm. In order to collect scintillated photons only from gamma ray, not from electrons, LYSO-SC was positioned behind the Lanex3, after removing electrons by the magnet. LYSO-SC was installed 2460 mm away from the gas-cell exit and 1580 mm away from the magnet. A sCMOS camera (Andor, new iStar Gen 3) was used for recording the gamma-ray profile on LYSO-SC, and the pixel size of the camera was 146 μm vertically and 151 μm horizontally. Considering the distance between the gas-cell exit to LYSO-SC, the pixel size is converted to 59 μrad vertically and 61 μrad horizontally. Figure 2.27 shows the photo of LYSO-SC.

Figure 2.27: Photo of the single crystal LYSO used for measuring the gamma-ray beam profile of NCS.

LYSO-PX, a pixelated LYSO scintillation detector, was prepared to measure the energy spectrum of NCS gamma rays. LYSO-PX was installed 3225 mm away from the gas-cell exit. An sCMOS camera (PCO, PCO.Edge) was used to record the scintillation signal from LYSO-PX. Here, the gamma-ray energy spectrum can be retrieved from the scintillation signal generated through the energy deposition mainly by the pair production process of gamma rays propagating through LYSO-PX. A total of 4050 pixels makes up LYSO-PX, divided into 90 horizontally and 45 vertically, and each pixel had the size of 1 mm x 1 mm x 12.5 mm. The pixel separator was composed of BaSO4 with a 0.1 mm thickness. The pixel size of the sCMOS camera was 76 μm by 76 μm. Considering the distance between the gas-cell exit and LYSO-PX, the pixel size was converted to 24 μrad. Figure 2.28 shows the photo of LYSO-PX.
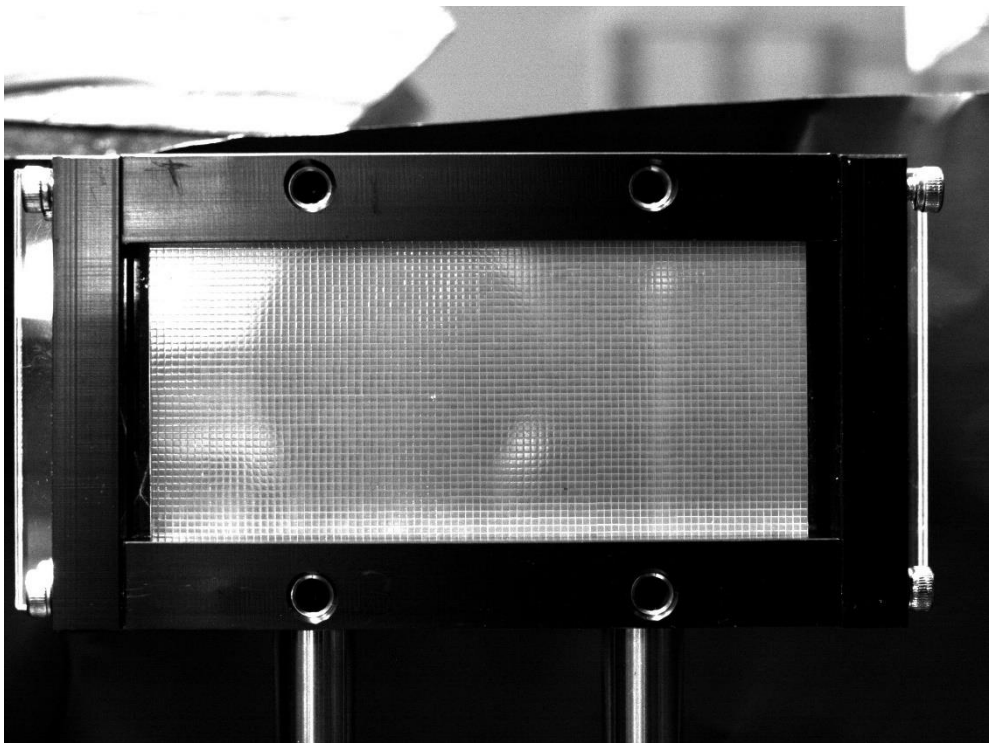
Figure 2.28: Photo of the pixelated LYSO.

2.6 Experimental results and conclusion

2.6.1. Experimental procedure

In an NCS experiment, the main driving laser was optimized for electron acceleration to produce a multi-GeV electron beam. The gas density, the group delay dispersion of the main driving laser, and the focus point of the main driving laser were adjusted to optimize the generation of a multi-GeV electron beam. The scattering laser was, then, synchronized with the main driving laser for Compton scattering. In an NCS experiment, bremsstrahlung sources, aluminum foil and Lanex1, were removed. A series of NCS laser shots were performed while changing the time delay between the two laser beams to obtain a strong gamma-ray signal from NCS.

2.6.2. Experimental results and conclusion

Through the process mentioned in the experimental procedure, the NCS experiment was conducted with ultra-relativistic electrons with energy over 2 GeV and an ultrahigh intensity laser with a peak intensity of $a_0 \approx 13$. Measured electron spectra and gamma-ray signals from NCS are shown in Figure 2.29. The measured electron and gamma-ray signals contain dotted noise signals, as shown in Figure 2.29 a)-c), because the cameras were exposed to x-rays generated during the electron acceleration. In order to remove the spiky noise, an image processing tool, ImageJ[53], was used. The 'Remove Outliers function of ImageJ replaces a pixel by the median of the pixels around it when the pixel value deviates from the median

by more than a threshold value. Here, the threshold level was set to 50, and radius, which determines the area used for calculating the median, was set as 5 for Lanex 3 and LYSO−PX and 2 for LYSO−SC. Figure 2.29 d)−f) shows the data after replacing the spiky noise. After that, the background area where there are no electron and gamma ray signals were defined. The background value was obtained by averaging signals in the background area. The data after removing the spiky noises and subtracting the background are shown in Figs. g)−i). Additional representative NCS results are shown in Figure 2.30 and Figure 2.31.

In conclusion, for NCS experiments, two ultrahigh intensity laser beams of a main driving laser and a scattering laser beam, a synchronization tool for the two lasers, and a set of diagnostics for characterizing electrons and gamma−rays were prepared and successfully examined. The main driving laser utilizes a focal spot optimization system that was optimized to minimize wavefront aberrations and maximize the energy concentration in the Airy disk, while achieving the peak laser intensity of $a_0 \approx 2$. As a result, mono− energetic electrons with energy over 2 GeV were generated using a gas cell. The scattering laser beam was optimized to a laser peak intensity of $a_0 \approx 13$ using an off−axis parabolic mirror. A spatiotemporal synchronization system was introduced to scatter the electrons with the scattering laser beam, and as a result, synchronization was achieved with the spatial accuracy of 0.6 um and the temporal jitter of an 11 fs. Additionally, by introducing a real− time delay monitoring system, the time delay was measured in real−

time and maintained during an experiment. As a result, the success rate of Compton scattering was raised to 40%. In order to carry out NCS experiments, a set of gamma−ray diagnostics based on LYSO scintillators were prepared to measure the beam profile and the energy spectrum of gamma−ray, in addition to the electron spectrometer used for acquiring electron energy spectra. After all the preparation for Compton scattering experiments, a series of NCS experiment were successfully performed; nonlinear Compton scattering between an electron beam with energy of 2 GeV or higher and an ultrahigh intensity beam with a peak laser intensity of $a_0 \approx 13$.
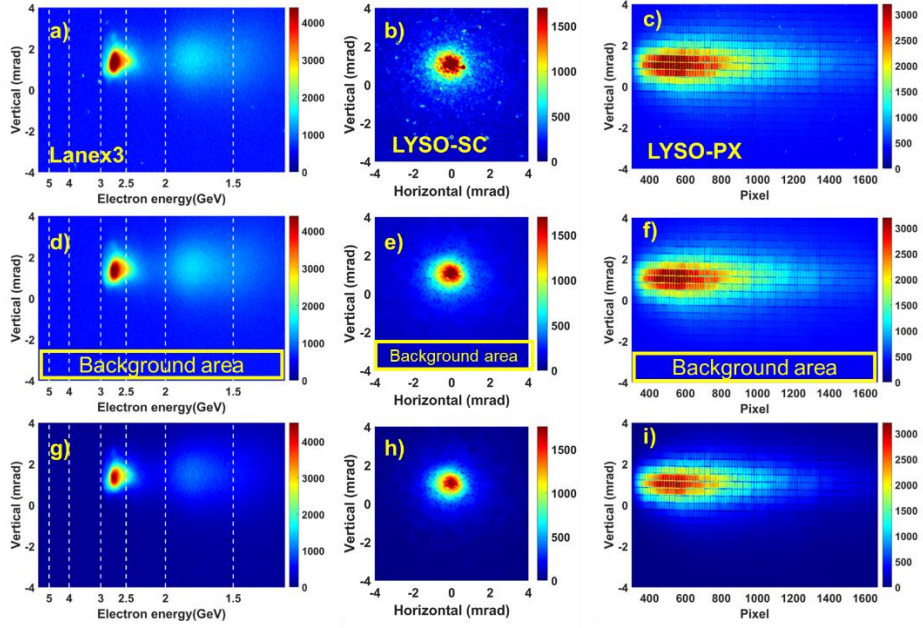
Figure 2.29: Measured results of the shot #1781 (false color). The data of electron and gamma-ray measurements are processed in two steps: a-c) raw data, d-f) data after removing spiky noises, and g-i) data after the subtraction of background. a), d), and g) Electron energy spectra (false color) taken from Lanex 3. b), e), and h) Gamma-ray beam profiles obtained from LYSO-SC. c), f), and i) Gamma-ray signals measured from LYSO-PX.
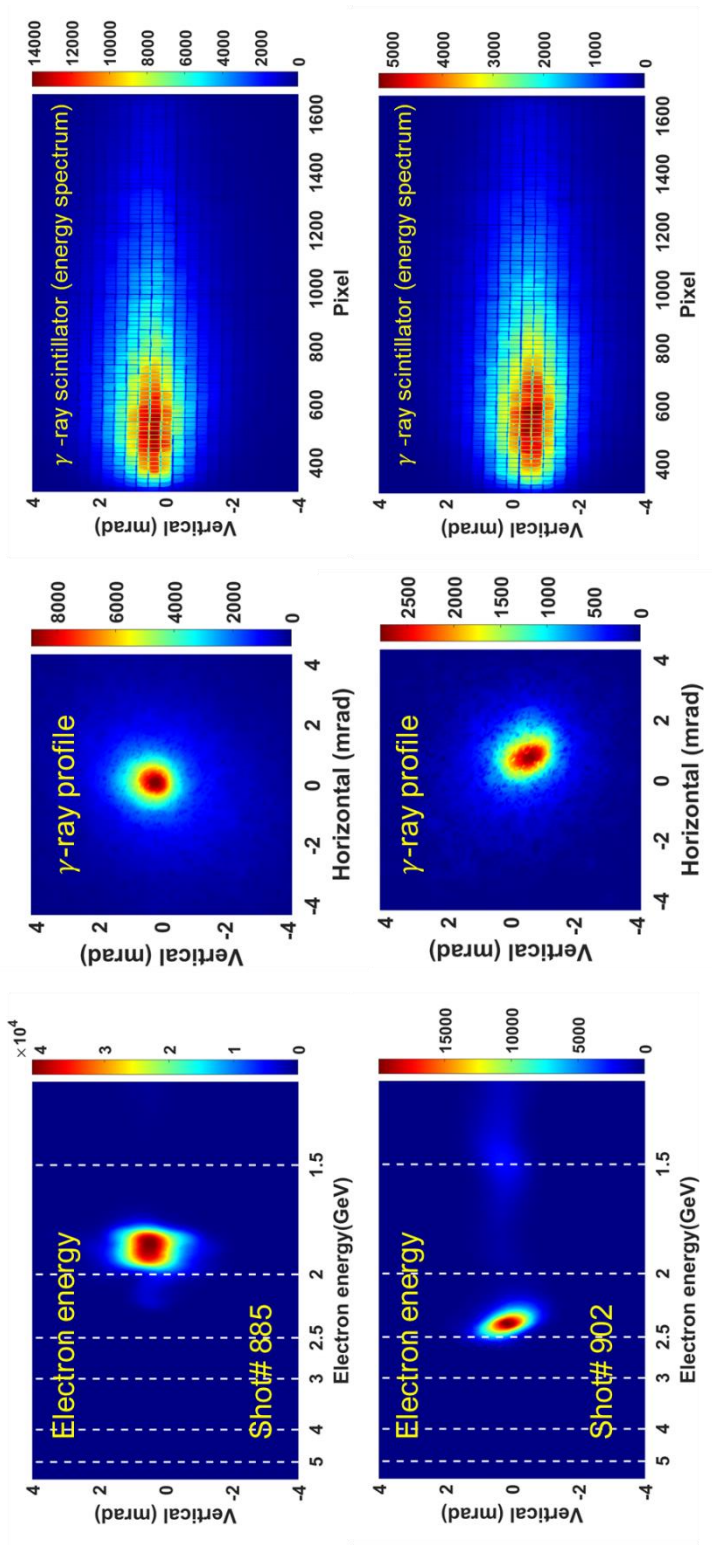
Figure 2.30: Measurement results, shots #885 and 902, of NCS experiments (false color). a, d) Electron energy spectrum measured on Lanex 3. b, e) Gamma−ray profile measured with LYSO−SC. c, f) Gamma−ray signals from LYSO−PX.
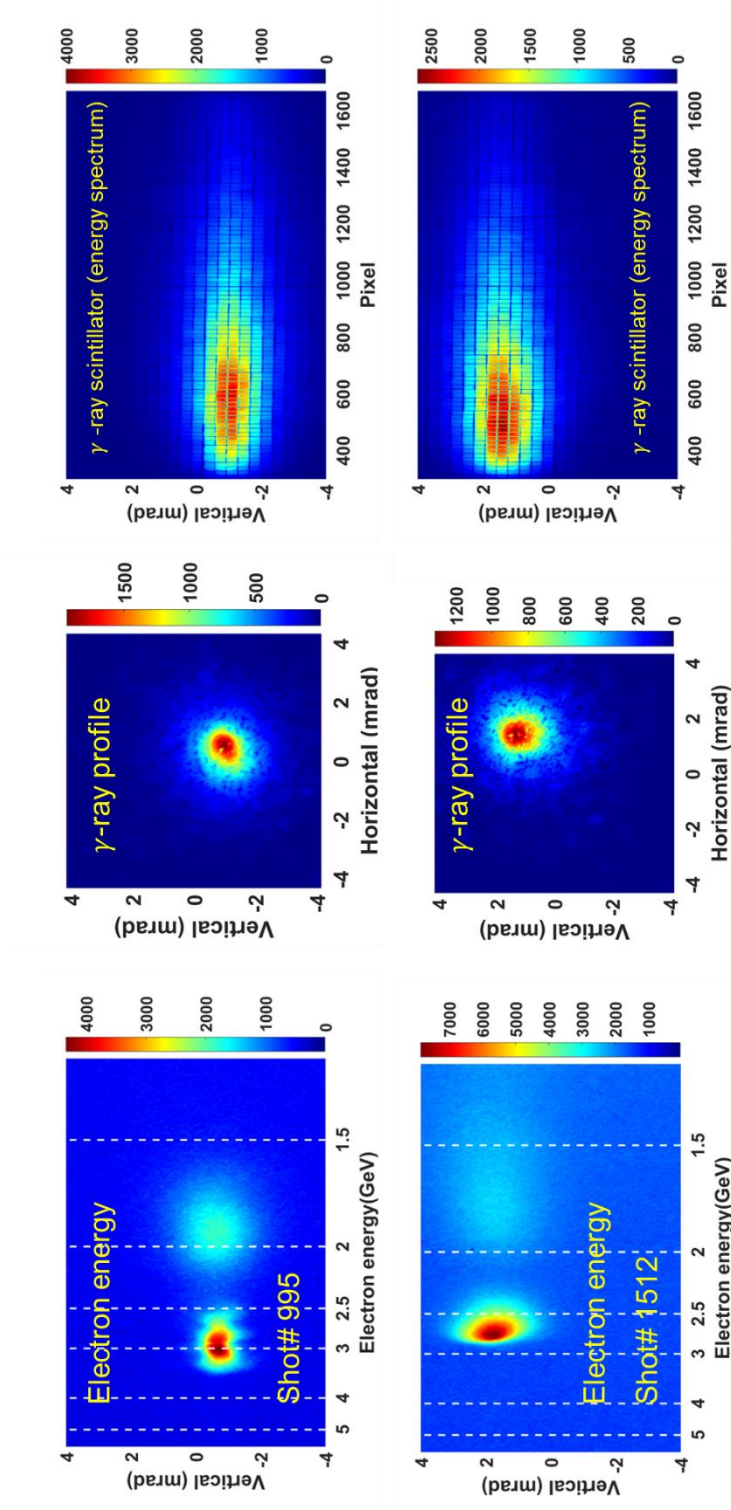
Figure 2.31: Measurement result, , shots #995 and 1512, of NCS experiments (false color). a) and d) Electron energy spectrum measured on Lanex 3. b) and e) Gamma–ray profile measured with LYSO–SC. c) and f) Gamma–ray signals from LYSO–PX.

Chapter 3. Analysis of gamma rays from nonlinear Compton scattering

3.1. Introduction

The Compton scattering between a multi-GeV electron beam and an ultrahigh intensity laser can be examined by analyzing the gamma-ray data from the single crystal LYSO (LYSO-SC) and the pixelated LYSO (LYSO-PX). The gamma-ray beam profile from LYSO-SC can provide the scattering position and possibly the delay time. The signal from LYSO-PX contains information on the gamma-ray energy spectrum.

The gamma-ray energy spectrum was obtained from two methods, as shown in Figure 3.1. The first method is the simultaneous iterative reconstruction technique (SIRT). SIRT iteratively seeks the gamma-ray energy spectrum to reproduce the measured result from LYSO-PX. The response function of LYSO-PX for a given gamma-ray energy was obtained by Geant4, the simulation code calculating the propagation of particles and radiation through matter. The other method, called the cross-sectional method, calculates the gamma-ray signal using the nonlinear Compton scattering (NCS) cross section. The required parameter for the cross-sectional method is the electron energy spectrum and the laser intensity used in an experiment. The energy spectrum of an electron beam is measured using a magnetic spectrometer coupled to Lanex 3, a scintillation screen. The actual intensity of the scattering

laser during a scattering is affected by experimental parameters, such as time delay and beam pointing jitters. The laser intensity can be estimated from the gamma-ray profile on LYSO-SC. By substituting the gamma-ray energy spectrum from the cross-sectional method to the response function of LYSO-PX, the validity of the gamma-ray energy spectrum from SIRT can be confirmed.
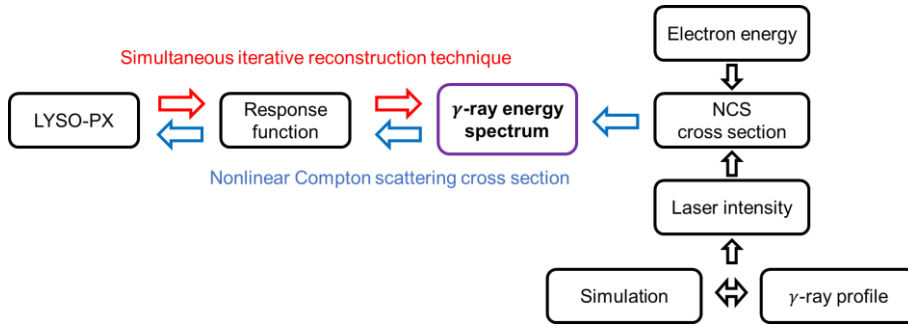
Figure 3.1 Diagram illustrating the process to retrieve the gamma-ray energy spectrum from an experimental result. The red arrow represents the use of the simultaneous iterative reconstruction technique. The blue arrow represents the cross-sectional method utilizing the NCS cross-section.

This chapter contains following sections. Section 3.2 presents the SIRT method and the response function of LYSO－PX calculated using Geant4 for a set of gamma－ray energies. Section 3.3 introduces the procedure for obtaining the gamma－ray energy spectrum using the cross－sectional method. Section 3.3.1 provides the theory of the NCS cross－section. In order to estimate the laser intensity during scattering, the simulation of the scattering process is introduced and described in Sec. 3.3.2. The input parameters for the simulation are determined by comparing the simulated and the measured gamma－ray profiles. The simulation provides the laser intensity during the scattering in Sec. 3.3.3. Section 3.4 presents the gamma－ray energy spectrum obtained from both methods. Finally, Section 3.5 presents the analysis results of gamma－ray energy spectra and the conclusion.

3.2. Simultaneous iterative reconstruction technique

The simultaneous iterative reconstruction technique (SIRT) is a method used to reconstruct an image in tomography[54, 55]. It uses an iterative process to evaluate a correction term for the signal from each pixel, while taking into account all obtained signals. The iteration method can be expressed as follows:

$$x_j^{k+1} = x_j^k + \sum_{i=1}^{m} a_{ij} \frac{b_i - \sum_{j=1}^{n} a_{ij} x_j^k}{\sum_{i=1}^{n} a_{ij}^2} \qquad (3.1)$$

Here, j is an index of gamma-ray energy, i is a pixel index of a LYSO-PX signal, k is an iteration number, x_j is the number density of jth gamma-ray energy (j=1,2,3, ... ,101, and $E_j = 1, 10, 20, 30, ... ,1000\ MeV$), a_{ij} is the signal on the ith pixel of LYSO-PX contributed by the gamma ray with energy E_j, b_i is the measured signal intensity on the ith pixel of LYSO-PX. In this study, the convergence condition for iteration was set as $R^2 > 0.99$. To obtain the gamma-ray energy spectrum without any prior information, an initial input parameter set was assigned randomly. Figure 3.2 shows the iteration result of the gamma-ray energy spectrum of shot #1781. As the iteration was repeated, it was confirmed that a gamma-ray energy spectrum with a similar response to the measured value of LYSO-PX was found and $R^2 > 0.99$ was achieved after 73 iterations.
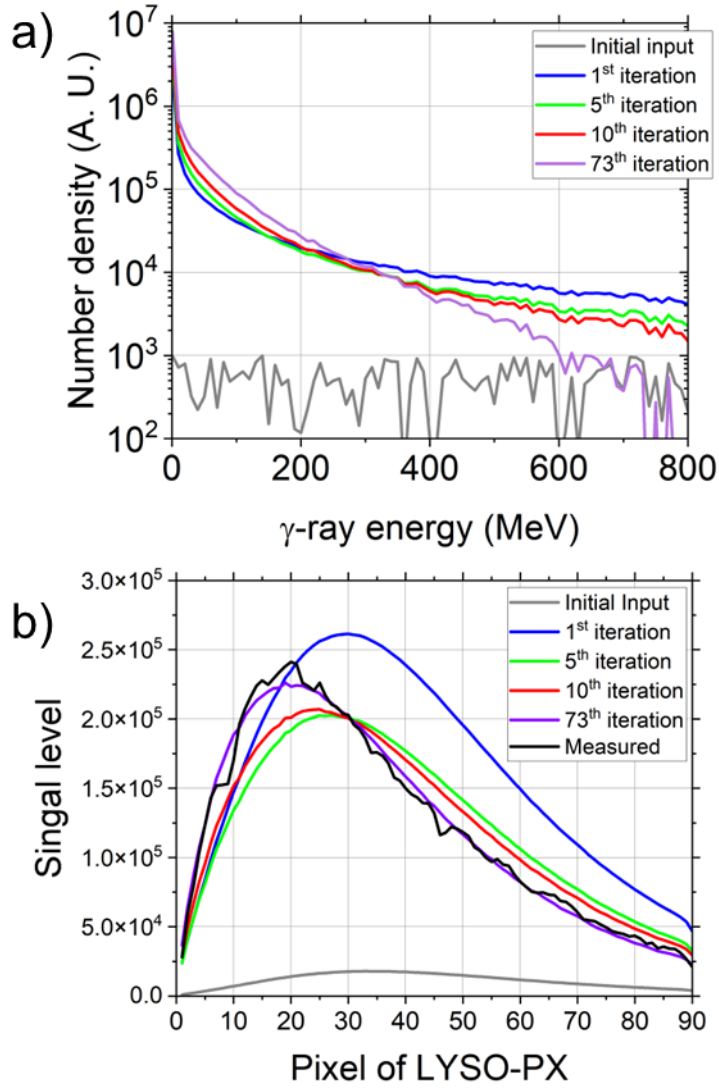
Figure 3.2: Gamma-ray spectrum reconstructed with SIRT. a) Gamma-ray energy spectrum obtained from SIRT at each iteration. b) Measured LYSO-PX signal of shot# 1781 (black) and the simulated LYSO-PX results depending on the number of iterations.

3.2.1. Response function

In order to calculate the expected response of LYSO−SC and LYSO−PX for a given gamma−ray energy spectrum, Geant4[56, 57], the particle and radiation simulation toolkit, was used. Geant4 is a widely used simulator in particle physics that can simulate particle interactions such as elastic, intrinsic scattering, bremsstrahlung, and pair production that occur in a medium. In this study, the simulation was used to determine how much gamma−ray energy is transferred to LYSO−SC and LYSO−PX while propagating through it. For a more practical simulation, the number of optical photons emitted from each scintillator element when the gamma−ray transfers energy was desirable. In general, the number of optical photons generated from the scintillator is proportional to the stored energy. Therefore, the stored energy at each scintillator depending on gamma−ray energy was simulated to calculate the response function.

In the Geant4 simulation, the geometry of the LYSO scintillators was implemented with their actual size, as shown in Figure 3.3. The simulation details are as follows: a physic list was the 'QGSP_BERT', a background material was 'air', LYSO material was $Lu_{0.9}Y_{0.9}Si_2O_5$ with a density of $7.15 \, g/cm^3$, a pixel separator between each pixel in pixelated LYSO was composed of 0.1−mm−thick $BaSO_4$ with a density of $4.49 \, g/cm^3$, a distance between LYSO−SC and LYSO−PX was 765 mm, and the gamma−ray was set as uniform circular plane source with 2−mm diameter and zero divergence. The gamma rays, 350 mm away from the LYSO−SC, propagated through the center of LYSO−SC and LYSO−PX. The simulation was performed by

propagating 10^5 gamma-ray photons for the gamma-ray energy of 1MeV, 10MeV, 20 MeV, 30 MeV, …, and 1000 MeV. In this way, the stored energy at LYSO-SC and LYSO-PX depending on injected gamma-ray energy was obtained. Figure 3.4 shows the stored energy at LYSO-SC with respect to injected gamma-ray energy, and Figure 3.5 shows the vertically integrated LYSO-PX response for a set of injected gamma-ray energies.
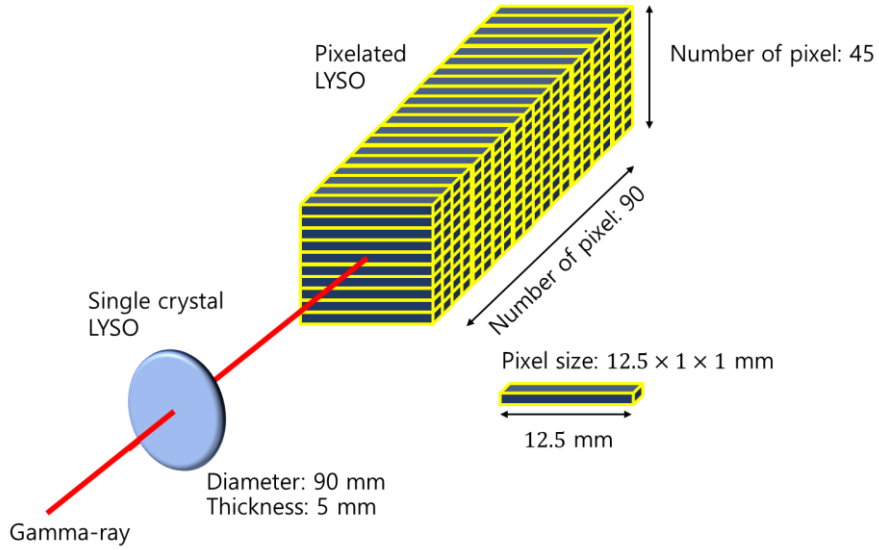
Figure 3.3: Schematics of the two scintillators used in the Geant4 simulation. The gamma-ray (shown in red) is injected into the center of the single crystal LYSO and the pixelated LYSO. The size and number of pixels of LYSO-PX is indicated in the figure.
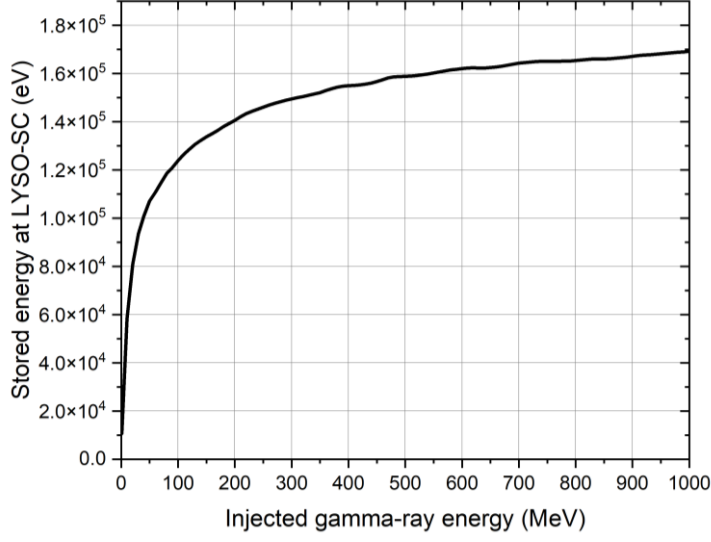
Figure 3.4: Simulated stored energy in LYSO-SC as a function of injected gamma-ray energy.
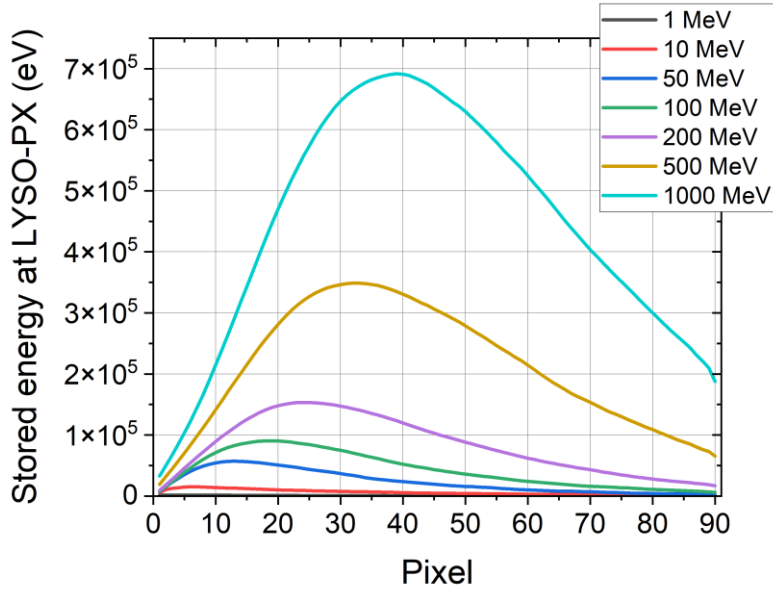
Figure 3.5: Simulated stored energy (vertically integrated) at each pixel position of LYSO-PX for a set of injected gamma-ray energies.

3.3. Cross－sectional method

A cross－sectional method is a method to calculate the gamma－ray energy spectrum based on the NCS cross section. For this method, the NCS cross－section for given electron energy and laser intensity are required.

3.3.1. Nonlinear Compton scattering cross section
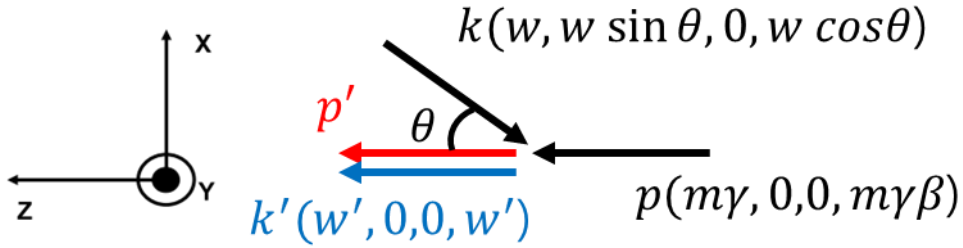
Figure 3.6: Schematics of nonlinear Compton scattering. The momentum 4－vectors of incident and scattered electrons, as well as those of photons, are represented.

The NCS cross section was estimated for the scattering geometry in Figure 3.6, showing the momentum 4－vectors of the incident and scattered electrons, as well as those of the photons. In the Fig., k($k^{'}$) represents the 4－vector of an incident (scattered) photon in the lab frame, p($p^{'}$) represents the 4－vector of the incident (scattered) electron in the lab frame. In the experimental setup, the 4－momenta of the electron and laser photon can be written as $p_\mu(m\gamma, 0,0, m\gamma\beta)$, $k_\mu(w, w\sin\theta, 0, w\cos\theta)$. The effective 4－vector of an electron, q_μ, in a linearly polarized electromagnetic wave is described as follows. Here,

for convenience, the natural units ($c = 1, \hbar = 1$) are used.

$$q_\mu = p_\mu + \frac{e^2 a_0^2}{4\,(kp)} k_\mu = p_\mu + \varepsilon k_\mu \qquad (3.2)$$

Where, m is electron mass, and e is the elementary charge. The scattering process must follow the conservation law.

$$nk + q = k' + q' \qquad (3.3)$$

Or,

$q' = nk + q - k' = (nw + m\gamma + \varepsilon w - w', nw\ sin\theta + \varepsilon w \sin\theta, 0, nw \cos\theta$

$+m\gamma\beta + \varepsilon wcos\theta - w')$.

Then the NCS cross section for the cross−sectional method (CSM) can be described by applying the plane wave approximation[58−61].

$$\frac{d\sigma_{CSM}}{du} = \frac{e^2 m^2}{8\pi^2 q_0} \frac{1}{(1+u)^2} \sum_{n=1}^{\infty} \int_0^{2\pi} d\varphi\, \{-A_0^2$$

$$+ a_0^2 \left(1 + \frac{u^2}{2(1+u)}\right)(A_1^2 - A_0 A_2)\} \qquad (3.4)$$

where, $u = \frac{k \cdot k'}{k \cdot q'}$ for $0 \le u \le u_n$,

$A_m(n, \alpha, \beta) = \frac{1}{2\pi} \int_{-\pi}^{\pi} d\phi\, cos^m(\phi) \cos(n\phi - \alpha \sin(\phi) + \beta \sin(2\phi))$,

$\alpha = z_n cos\varphi, \beta = \frac{a_0^2 u m^2}{8\,k \cdot p}$,

$z_n(u, u_n) = \frac{2na_0}{\sqrt{1+0.5a_0^2}} \sqrt{\frac{u}{u_n}(1 - \frac{u}{u_n})}$,

and $u_n = \frac{2nk \cdot q}{\tilde{m}^2}$, $\tilde{m} = m\sqrt{1 + 0.5a_0^2}$.

When $\gamma \gg a_0$, $\frac{du}{(1+u)^2} \sim \frac{dw'}{\gamma m}$,

$$\frac{d\sigma_{CSM}}{dw'} = \frac{e^2 m^2}{8\pi^2 q_0} \frac{1}{\gamma m} \sum_{n=1}^{\infty} \int_0^{2\pi} d\varphi \left\{ -A_0^2 \right.$$

$$\left. + a_0^2 \left(1 + \frac{u^2}{2(1+u)} \right) \left(A_1^2 - A_0 A_2 \right) \right\}$$

(3.5)

The linear Compton scattering cross section can be obtained with n=1 in Eq. 3.5. The cutoff energy, $\varepsilon_{\gamma,cutoff}$, of linear Compton scattering is given by:

$$\varepsilon_{\gamma,cutoff} \approx 2 \left(1 + \cos\theta \right) \gamma^2 \varepsilon_L$$

(3.6)

where ε_L is the photon energy of laser. The linear and nonlinear Compton cross sections as a function of laser intensity and electron energy are compared in Figure 3.7. Here, ε_γ is equivalent to w' in Eq. 3.5.
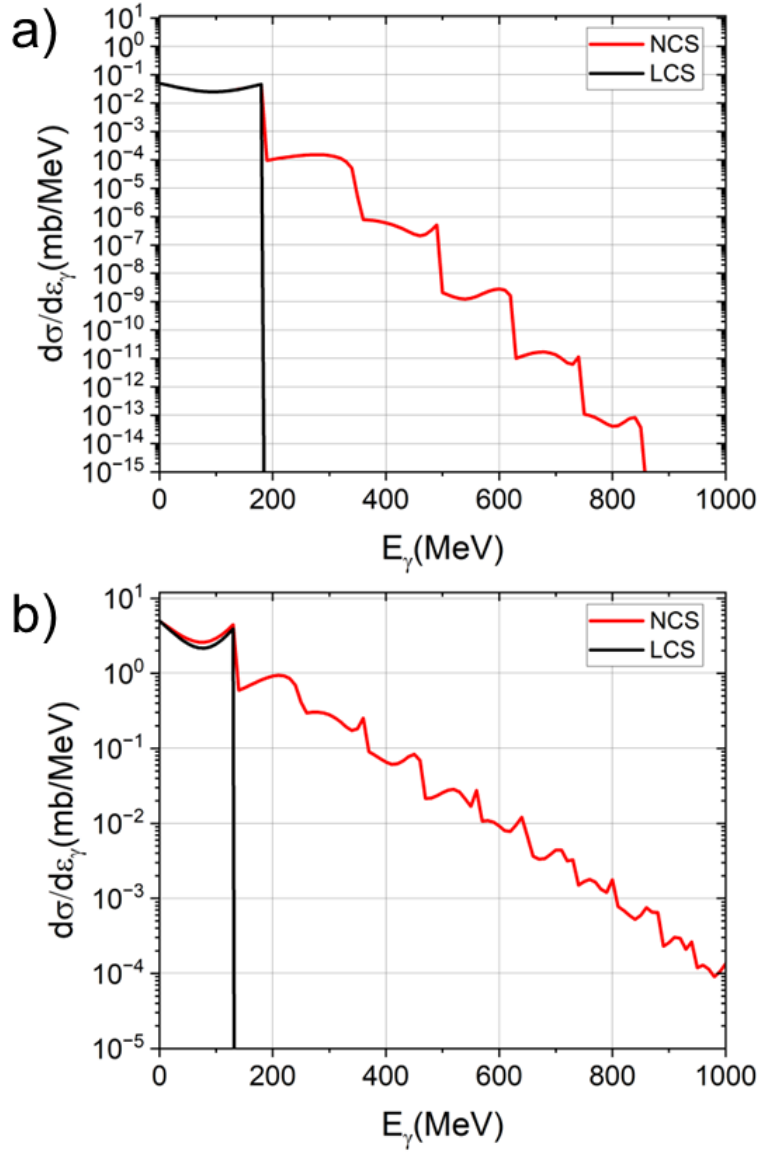
Figure 3.7: Cross section of linear (black) and nonlinear (red) Compton scatterings with the infinite plane wave assumption for the electron energy of 3 GeV and the laser intensity of a) $a_0 = 0.1$ and b) $a_0 = 1$.

3.3.2. Simulation of Compton scattering process

In order to estimate the laser intensity applied in an experiment, the scattering geometry of an electron beam and a scattering laser beam was considered in the (x, y, z, t) coordinate system.
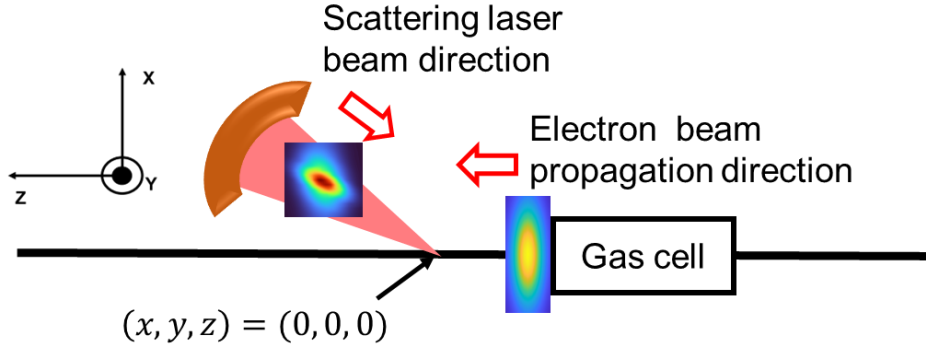
Figure 3.8: Scattering geometry between an electron beam and a scattering laser beam in the (x, y, z, t) coordinate. The electron beam from the gas−cell exit travels to the left direction. The scattering laser beam focused with the off−axis parabolic mirror is directed to the scattering position, (x, y, z) = (0, 0, 0). The scattering laser beam is scattering with the electron beam at (x, y, z, t) = (0, 0, 0, 0).

Figure 3.8 illustrates the scattering geometry between an electron beam from a gas cell and the scattering laser beam focused with an OAP in the (x, y, z, t) coordinate. The scattering laser beam moves from left to right with a scattering angle of 30 degree. The coordinate system in this study is defined as follows: The window of x and y ranges from −30 μm to 30 μm with an interval of 1 μm, the window of z ranges from −45 μm to 45 μm with an interval of 0.3 μm, and the

window of t ranges from −120 fs to 120 fs with an interval of 1 fs. The origin of the coordinate, (x, y, z) = (0, 0, 0), is set to be the intersection of the main driving laser and the scattering laser, or equivalently the scattering position. For the calculation of the scattering process, the following parameters are required: the electron profile, the pointing and profile of the scattering laser, and the time delay between the main and scattering lasers. Each parameter will be introduced in the following sections.

3.3.2.1. Scattering laser beam

In the simulation, the scattering laser beam directed to the scattering position is represented by

$$I_s(x, y, z, t) = I_0(x + \Delta x_{SL}, y +, \Delta y_{Sl}, z)$$

$$\times exp\left(-\frac{\left(\frac{z + \Delta z_{Sl}}{c} - (t - \Delta T)\right)^2}{2\sigma_s^2}\right) \quad (3.7)$$

where $I_0(x, y, z)$ is the spatial intensity profile of the scattering laser beam, Δx_{SL}, Δy_{SL} and Δz_{Sl} are the shift of the focal spot position in x, y, and z axes, respectively, ΔT is the time delay between the electron and the scattering laser beams, and σ_s is the pulse width (= 25 fs in FWHM).

The spatial intensity profile of the scattering laser beam was measured with a displacement range of −36 μm to 27 μm, as shown in Figure 3.9. The profile was then radially integrated and averaged, resulting in the radial intensity profile at the focal spot. Interpolation was employed to obtain the spatial intensity profile with a 1−μm displacement interval. Since the pointing and defocus fluctuations

were not measured during the experiment, the pointing fluctuation, Δx_{SL} and Δy_{SL}, was assumed to be $\pm$ 12 μm, and the defocus fluctuation, Δz_{SL}, was assumed to be less than two−thirds of the Rayleigh length, corresponding to 18 μm.
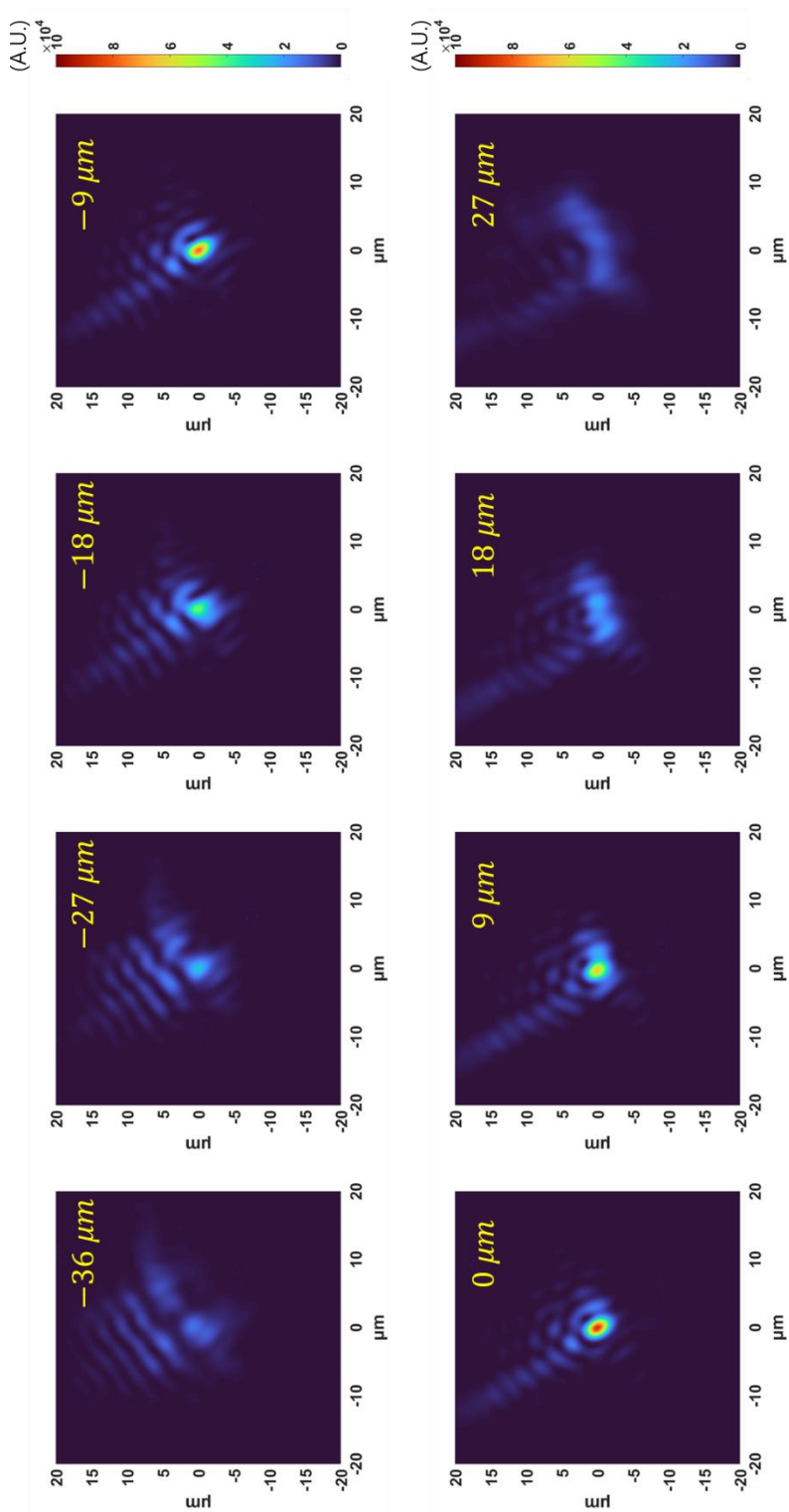
Figure 3.9: Spatial intensity profile of the scattering laser beam depends on the displacement from the focus position.
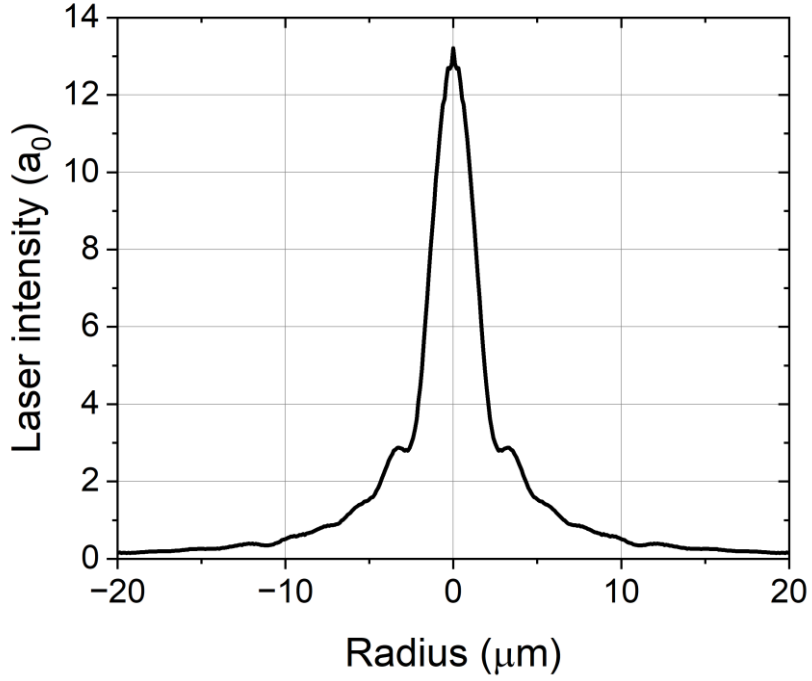
Figure 3.10: Intensity profile of a scattering laser beam at the focus position.

3.2.2.2. Electron beam

In the simulation, the electron beam directed to the scattering position is represented by the following equation:

$$N_e(x, y, z, t) = N_{e0}(x, y) \times exp\left(-\frac{(\frac{z}{c} - t)^2}{2\sigma_e{}^2}\right) \qquad (3.8)$$

where $N_{e0}(x, y, z)$ is the spatial intensity profile of the electron beam, Δx_e and Δy_e represent the deviation of the electron beam from the main driving laser axis in the x and y direction, respectively, and σ_e is the duration of an electron beam. In the simulation, σ_e is assumed to be 4.3 μm, corresponding to the temporal duration of 10 fs (FWHM), which is a typical duration of an electron beam obtained

with the laser wakefield acceleration scheme[42]. The spatial intensity profile of the main driving laser beam is treated as a 2－dimensional (x, y) Gaussian distribution. The electron beam profile for the y－axis was estimated from the vertical profile of an electron spectrum appeared on Lanex 3 and fitted to a Gaussian distribution function. As the x－axis profile could not be measured during an NCS experiment, it was assumed to be the same as that of the y－axis.

3.2.2.3. Time delay

The time delay between an electron beam and a scattering laser beam is a parameter in the simulation. The time delay between the main driving laser and an accelerated electron beam should be estimated and subtracted from the measured real－time delay. In the bubble regime of laser wakefield acceleration, an accelerated electron beam follows the main driving laser with a time delay corresponding to about half of the plasma wavelength, $\frac{1}{2}w_{pe} = \frac{1}{2}\sqrt{\frac{e^2 n_e}{\epsilon_0 m_e}}$. For an electron density of $n_e = 7 \times 10^{17} cm^{-3}$, a half of the plasma wavelength corresponds to the time delay of 68 fs. This time delay was confirmed from the correlation between the gamma ray pointing and the measured real－time delay, as shown in Figure 3.11. Figure 3.11 is a scatter plot of the real－time delay with respect to the horizontal pointing of gamma rays obtained from the LYSO－SC. The relation between the time delay, ΔT_{mea}, and the horizontal pointing, sc_h, of gamma－ray can be represented as a first－order polynomial function,

$$\Delta T_{mea} \ (fs) = -49 \ \times sc_{\hbar}(mrad) + 68 \qquad\qquad (\ 3.9\ )$$

The gamma rays should be pointed at zero when the electron and the scattering laser beams are perfectly synchronized. This means $sc_{\hbar} = 0$ and $\Delta T_{mea} = (T_{main} - T_e) + (T_e - T_{scatter}) = 68 \ fs$. For perfect synchronization, $(T_e - T_{scatter})$ is zero, so $(T_{main} - T_e)$ is 68 fs as predicted from the half of plasma wavelength. The time delay between the electron and the scattering laser beams can be expressed as,

$$\Delta T \ (fs) = T_e - T_{scatter} = \ -49 \ \times sc_{\hbar}(mrad) \qquad\qquad (\ 3.10\ )$$

Using Eq. 3.10, the time delay can be deduced by the horizontal pointing of LYSO−SC when the real−time delay monitoring system was not introduced.
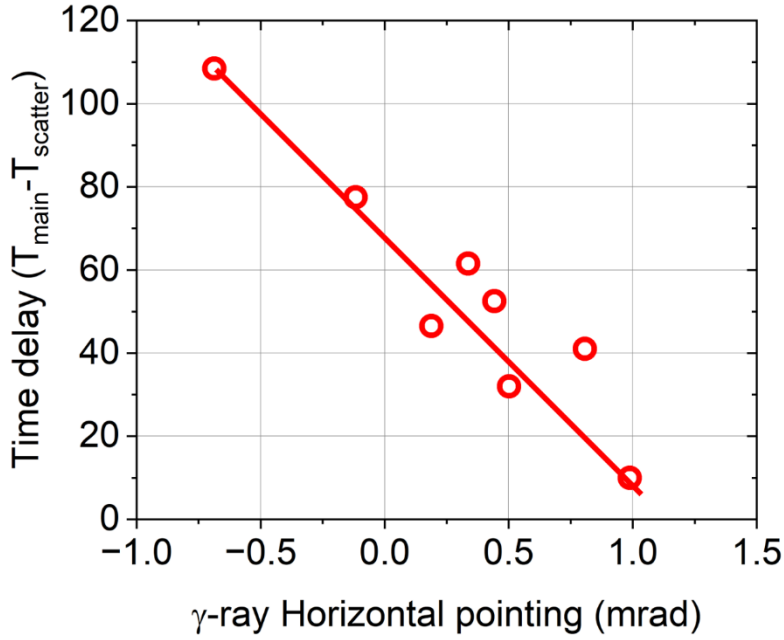
Figure 3.11: Scatter plot of time delay measured by the real-time monitoring system with respect to the horizontal gamma-ray pointing obtained from LYSO-SC. The red solid line in the scatter plot represents Eq. 3.9.

3.2.2.4. Projection ratio

For further comparison between the simulated gamma-ray profile and the measured one, it is necessary to know the projection ratio to convert the measured gamma-ray profile in the divergence map to the (x, y) coordinates. The projection ratio can be obtained from the relationship between the time delay and the pointing of gamma-ray.

$$26 = 49(1 - \frac{\sqrt{3}/2}{1 + \sqrt{3}/2})$$
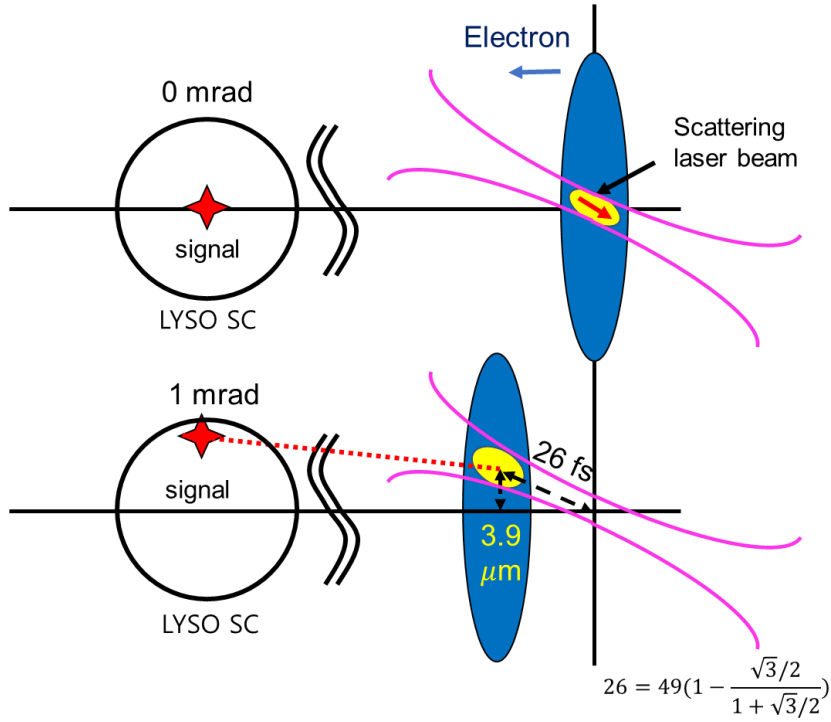
Figure 3.12: Illustration for understanding the projection ratio.

In the top image of Figure 3.12, the time delay between the electron and the scattering laser beams is zero, i.e., the scattering occurs at $(x, y, z) = (0, 0, 0)$ and the gamma−ray pointing is 0 mrad. In the bottom image of Figure 3.12 presenting the case of gamma− ray pointing of 1 mrad, the time delay between the electron and the scattering laser beams is 49 fs from Eq. 3.10. In this case, the electron beam scatters with the scattering laser beam where the center of the scattering laser beam is 7.8 μm away from the focal position, corresponding to 26 fs. Here, the distance between the center of the scattering laser beam and the main driving laser axis is 3.9 μm. As a result, the projection ratio is determined to be 3.9 μm/mrad.

3.2.2.5. Example of the simulation

Examples of the simulation depending on input parameters are given here. The first example is the case of $\Delta T = 0$, $\Delta x_{SL} = \Delta y_{SL} = 0$, and the electron beam profile has a Gaussian distribution of 30 μm in FWHM. In this case, the tightly focused scattering laser beam scatters with the electron beam at the location of $(x, y, z) = (0, 0, 0)$. Figure 3.13 shows an electron and scattering laser beam and the corresponding gamma-ray flux for this case. A gamma-ray flux is computed from $N_e(x, y, z, t) \cdot \int \frac{d\sigma_{CSM}}{d\varepsilon_\gamma} (a_0(x, y, z, t), \varepsilon_{e^-} = 2\ GeV)\ \varepsilon_\gamma d\varepsilon_\gamma$. $\frac{d\sigma_{CSM}}{d\varepsilon_\gamma}$ is the NCS cross section. Figure 3.14 shows the total time-integrated gamma-ray flux. This result shows that when the scattering laser beam makes a Compton scattering at the center of the electron beam, the gamma-ray profile becomes a symmetrical shape.
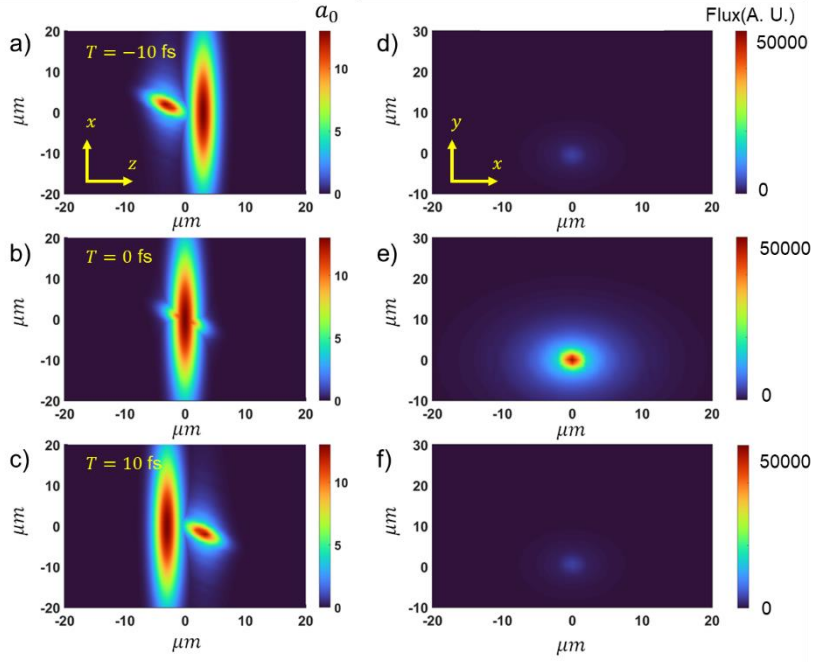
Figure 3.13: Electron and scattering laser beam implemented in the (x, y, z, t) coordinate for the case of $\Delta T = 0$, $\Delta x_{SL} = \Delta y_{SL} = \Delta z_{SL} = 0$, and the electron beam profile is the gaussian distribution of 30 μm (FWHM). a−c) Scattering profiles of the electron (moving from right to left) and the scattering laser beams (moving from left to right) at the time specified in each figure. d−f) Computed gamma−ray flux for a)−c), respectively.
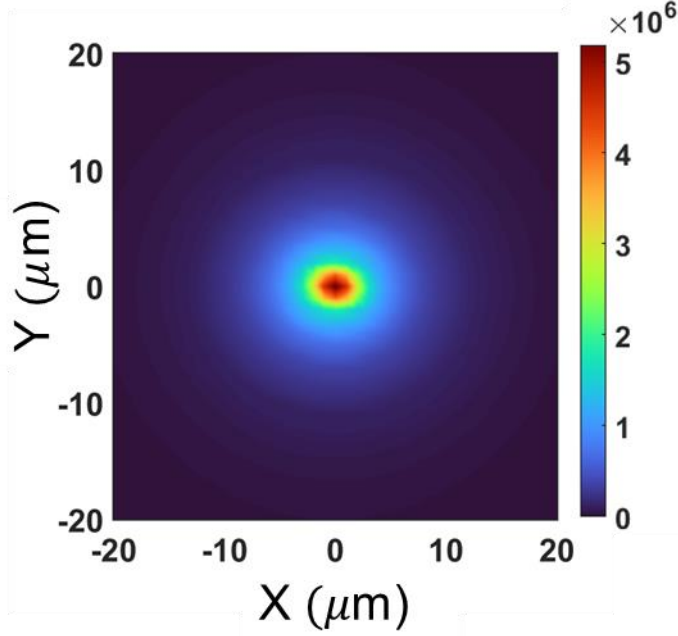
Figure 3.14: Total gamma−ray flux for the case shown in Figure 3.13.

The second example is the case of $\Delta T = 150\,fs$, $\Delta x_{SL} = 0$, $\Delta y_{SL} = 0\,\mu m$, $\Delta z_{SL} = 0$, and the electron beam profile is a gaussian distribution of $30\,\mu m$ in FWHM. In this case, the scattering laser beam scatters with the electron beam before reaching the focus; the strongest scattering position is $(x, y, z) = (12, 0, -22)\,\mu m$. The maximum laser intensity during the scattering is lower than in the first example case. Figure 3.15 shows the electron and the scattering laser beams implemented in the (x, y, z, t) coordinate for this case. Figure 3.16 shows the total time−integrated gamma−ray flux. Because of the time delay, the scattering laser beam makes a scattering at the edge of the electron beam, producing the asymmetrical gamma−ray profile.
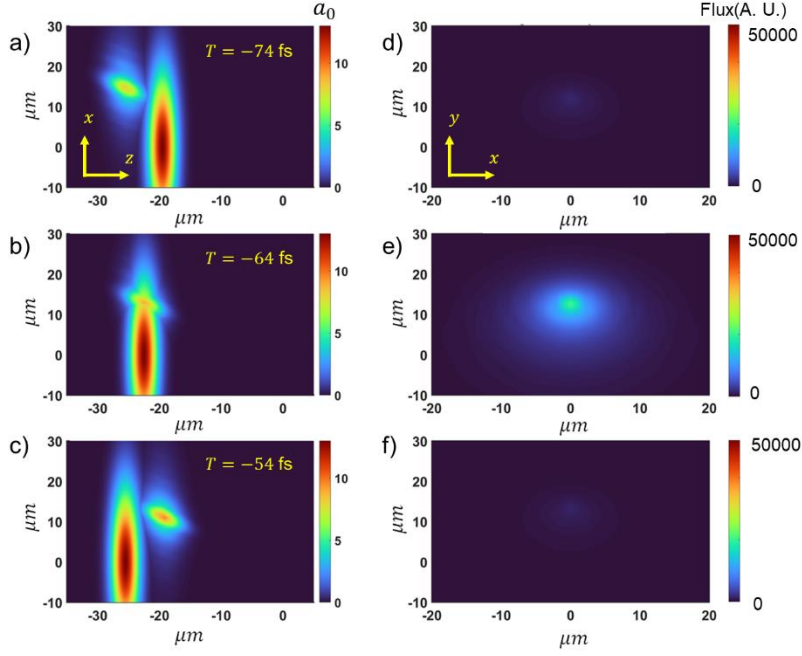
Figure 3.15: Electron and scattering laser beam implemented in the (x, y, z, t) coordinate for the case of $\Delta T = 150$ fs, $\Delta x_{SL} = \Delta y_{SL} = \Delta z_{SL} = 0$, and the electron beam profile is the gaussian distribution of 30 μm (FWHM). a–c) Scattering profiles of the electron (moving from right to left) and the scattering laser beams (moving from left to right) at the time specified in each figure. d–f) Computed gamma–ray flux for a)–c), respectively.
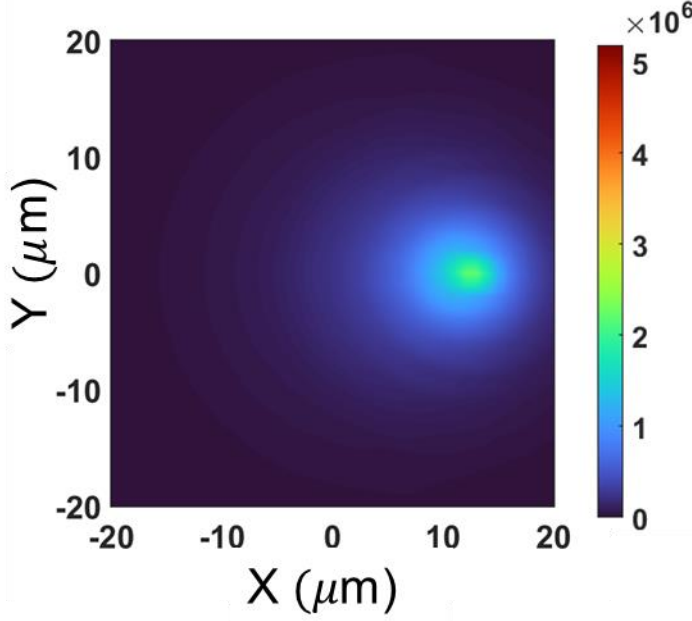
Figure 3.16: Total gamma−ray flux for the case shown in Figure 3.15.

3.3.3. Estimation of laser intensity

The realistic simulation of a scattering process can be performed after obtaining actual experimental parameters. By finding the experimental parameters, including laser intensity, corresponding to a measured gamma−ray profile, the scattering process can be simulated. The expected gamma−ray profile was calculated as follows.

$$SC_{expected}(x, y)$$

$$= C \int \int N_e(x, y, z, t) \cdot \frac{d\sigma_{CSM}}{d\varepsilon_\gamma}(a_0(x, y, z, t), \varepsilon_{e^-}) \quad (3.11)$$

$$\cdot R_{LYSO-SC}(\varepsilon_\gamma) \ d\varepsilon_\gamma \ dz \ dt$$

Here, $SC_{expected}(x, y)$ is a calculated gamma−ray profile on LYSO−SC, C a normalizing factor to set the maximum value of $SC_{expected}(x, y)$ as

1, and $R_{LYSO-SC}(\varepsilon_\gamma)$ the response function of LYSO-SC obtained at Sec. 3.2.1. Because the experimental parameters of the simulation can be found by comparing the simulated and the measured gamma-ray profiles. For comparison, measured gamma-ray profiles were also normalized and projected into the (x, y) plane using the projection ratio (3.9 μm/mrad).

3.3.3.1. Structural similarity index measure

Experimental parameters can be estimated by comparing a calculated gamma-ray profile with a measured result. The actual scattering laser intensity during a Compton scattering is not directly measurable, but very critical for rigorous analysis and understanding of the scattering process. The estimation of experimental parameters including scattering laser intensity is sought by analyzing a measured gamma-ray profile on LYSO-SC using the structural similarity index measure[62] (SSIM). SSIM is a method to compare two images using three elements: luminance, contrast, and structure. The value of the SSIM can range from 0 to 1. The closer to 1, the more similar the two images are. Luminance is described as $I(x,y) = \frac{2\mu_x\mu_y + C_1}{\mu_x{}^2 + \mu_y{}^2 + C_1}$, where $\mu_x = \frac{1}{N}\sum_{i=1}^N x_i$ is an average intensity of pixel, x_i is an intensity of i-th pixel, N is the number of total pixels, C_1 is a constant to prevent a denominator to become zero and normally expressed as $C_1 = (K_1 L)^2$ with K_1=0.01 and L being a range of intensity. Contrast is described as $c(x,y) = \frac{2\sigma_x\sigma_y + C_2}{\sigma_x{}^2 + \sigma_y{}^2 + C_2}$, C2 is also a constant to prevent a denominator to become zero and expressed as $C_2 = (K_2 L)^2$, normally K_2=0.03.

Structural similarity has the same meaning as the correlation of two images described as $s(x,y) = \frac{\sigma_{xy}+C_3}{\sigma_x\sigma_y+C_3}$, where $\sigma_{xy} = \frac{1}{N-1}\sum_{i=1}^{N}(x_i - \mu_x)(y_i - \mu_y)$. For the convenience of formula, $C_3 = 0.5 \times C_2$ is assumed. Then SSIM can be expressed as $SSIM(x,y) = I(x,y)^\alpha \cdot c(x,y)^\beta \cdot s(x,y)^\gamma$. To make a simple expression, $\alpha = \beta = \gamma = 1$ was assumed and the SSIM can be expressed as,

$$SSIM(x,y) = \frac{(2\mu_x\mu_y + C_1)(2\sigma_{xy} + C_2)}{(\mu_x{}^2 + \mu_y{}^2 + C_1)(\sigma_x{}^2 + \sigma_y{}^2 + C_2)} \qquad (3.12)$$

3.3.3.2. Comparison of gamma-ray profile

Simulated gamma-ray profiles obtained with a range of experimental parameters will be compared with the measured data. In the simulation, the experimental parameters, ΔT, Δx_{SL}, Δy_{SL} and Δz_{SL}, were considered input variables. Here, the shot #1781, with a peak electron energy of 2.7 GeV and time delay of 0 fs, was representatively analyzed. The simulated gamma-ray profile was compared with the measured data. Tables 1 and 2 show the SSIM values depending on the experimental parameters, and Figure 3.17 shows the result most similar to the measurement of shot #1781. Measured gamma-ray beam profile shows symmetrical shape based on x = 0, also the simulated gamma-ray profile with the experimental parameters, $\Delta T = 0\,fs, \Delta x_{SL} = 0\,\mu m, \Delta y_{SL} = 4\,\mu m,$ and $\Delta z_{SL} = 0\,\mu m,$ shows symmetrical shape.

SSIM (Δy_{SL}= 4 μm, Δz_{SL}= 0 μm)	$\Delta x_{SL} = -6$ (μm)	-4	-2	0	2	4	6
ΔT= -30 (fs)	0.1689	0.2749	0.4220	0.5772	0.6496	0.5387	0.3717
-20	0.2907	0.4613	0.6806	0.8865	0.9278	0.7278	0.4993
-10	0.3626	0.5582	0.7862	0.9553	0.8946	0.6550	0.4450
0	0.4405	0.6559	0.8747	0.9642	0.7973	0.5546	0.3730
10	0.5265	0.7522	0.9390	0.9178	0.6854	0.4657	0.3092
20	0.5865	0.8070	0.9397	0.8188	0.5742	0.3845	0.2499
30	0.4288	0.5796	0.6412	0.5175	0.3514	0.2313	0.1473

Table 1: Comparison result between simulated gamma-ray profiles and the measured one for the shot#1781. Simulations were carried for a set of ΔT and Δx_{SL} when $\Delta y_{SL} = 4\,\mu m$ and $\Delta z_{SL} = 0\,\mu m$.

SSIM (ΔT= 0 fs, Δx_{SL}= 0 μm)	$\Delta y_{SL} = -6$ (μm)	-4	-2	0	2	4	6
Δz_{SL}= -12 (μm)	0.0664	0.1536	0.2866	0.4805	0.7260	0.8865	0.7513
-8	0.0672	0.1578	0.2949	0.4976	0.7601	0.9404	0.7959
-4	0.0682	0.1597	0.2976	0.5034	0.7743	0.9640	0.8108
0	0.0688	0.1601	0.2968	0.5018	0.7735	0.9642	0.8060
4	0.0690	0.1588	0.2930	0.4936	0.7577	0.9391	0.7831
8	0.0689	0.1560	0.2862	0.4791	0.7280	0.8913	0.7436
12	0.0687	0.1510	0.2746	0.4557	0.6813	0.8188	0.6823

Table 2: Comparison result between simulated gamma-ray profiles and the measured one for the shot#1781. Simulations were carried for a set of Δy_{SL} and Δz_{SL} when $\Delta T = 0\,fs$ and $\Delta x_{SL} = 0\,\mu m$.
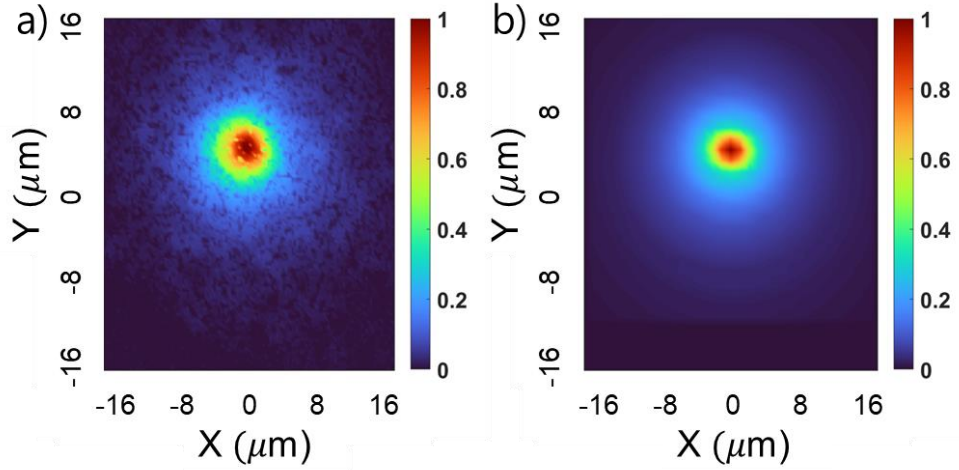
Figure 3.17: a) Measured gamma−ray beam profile from LYSO−SC of the shot #1781. b) Simulated gamma−ray beam profile with the parameters, $\Delta T = 0\,fs$, $\Delta x_{SL} = 0\,\mu m$, $\Delta y_{SL} = 4\,\mu m$ and $\Delta z_{SL} = 0\,\mu m$.

3.3.3.3. Laser intensity during the scattering

From the SSIM analysis the actual laser intensity during the scattering can be estimated, along with the number of scattered electrons. For the shot # 1781, the simulated gamma−ray profile using the parameters, $\Delta T = 0\,fs, \Delta x_{sl} = 0\,\mu m, \Delta y_{sl} = 4\,\mu m$, $\Delta z_{sl} = 0\,\mu m$, produced the highest SSIM result. Figure 3.18 shows a snapshot of the electron and the scattering laser beams in this case. At the coordinate of (x, y, z, t) = (0, 0, 0, 0), the scattering laser beam intensity and the electron beam density were $I_s(0,0,0,0) = 13$ and $N_e(0,0,0,0) = 4000$, as shown in Figure 3.18. In other words, the number of electrons scattering with a laser of $a_0 = 13$ is 4000. The total number of electrons scattered with the laser intensity $a_0 = 13$ can be obtained by $\int\int\int\int N_{e,scattered}(x,y,z,t)\,dxdydzdt$, where $N_{e,scattered}(x,y,z,t) = N_e(x,y,z,t)$ for $I_s(x,y,z,t) = 13$ and

$N_{e,scattered}(x, y, z, t) = 0$ for $I_s(x, y, z, t) \neq 13$. For shot #1781, the number of electrons scattering with a laser beam at a certain a_0 value is shown in Figure 3.19.
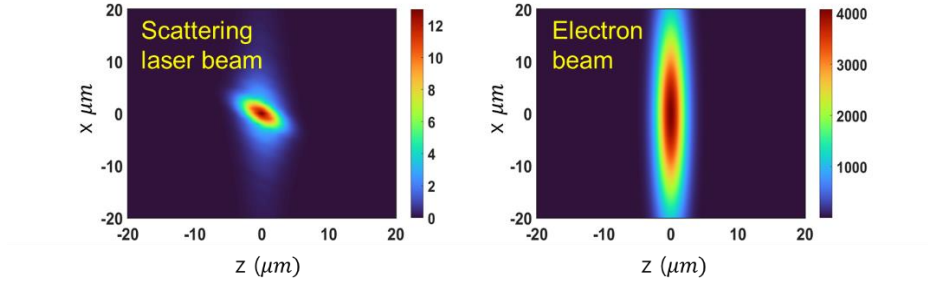
Figure 3.18: Images of (a) electron and (b) scattering laser beams in the x−z plane for $y = 4\ \mu m$ and $t = 68\ fs$ of the shot #1781.
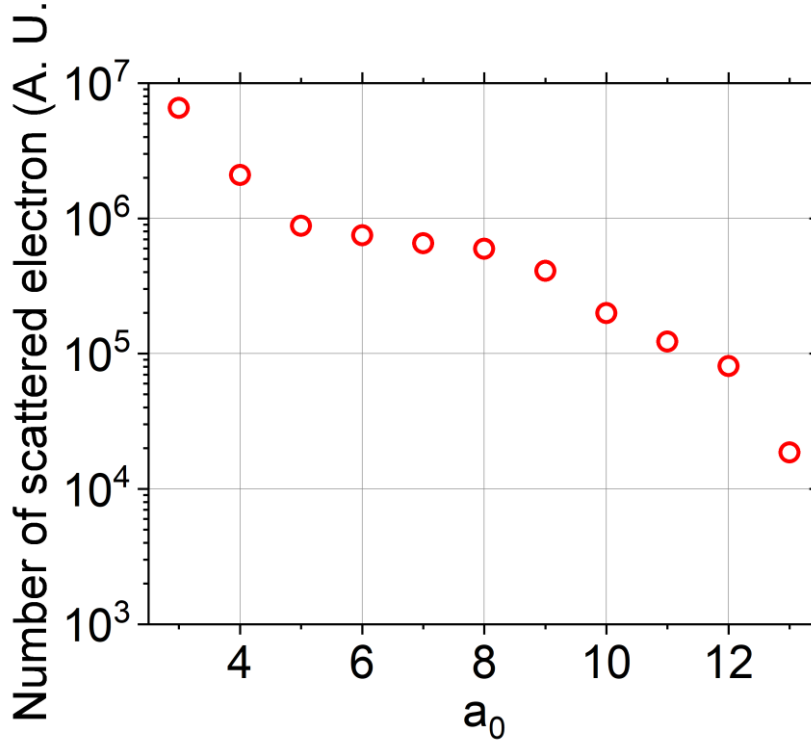
Figure 3.19: Distribution of scattering electrons with respect to a_0 of the shot #1781, with parameters of $\Delta T = 0\,fs, \Delta x_{sl} = 0\,\mu m, \Delta y_{sl} = 4\,\mu m$, and $\Delta z_{sl} = 0\,\mu m$.

The simulation results may not perfectly match the experimental results due to the factors such as a non−gaussian electron beam profile, pointing fluctuations, and other inaccuracies in the experimental setup. It is however noted that the peak position of the simulated gamma−ray profile is relatively insensitive to electron beam properties. As the electron beam size is much larger than the scattering laser beam, the peak position of the gamma−ray profile is more affected by the spatiotemporal distribution of the scattering laser beam than the electron beam. To determine if the simulated gamma−ray profile matched the measured profile, a threshold of

SSIM > 0.9 was used as the criterion. Figure 3.20 shows the scattering electron for different laser intensities, along with the corresponding gamma-ray profiles with SSIM > 0.9. The red circles represent the average scattering electrons at each laser intensity, with error bars indicating the minimum and maximum values.
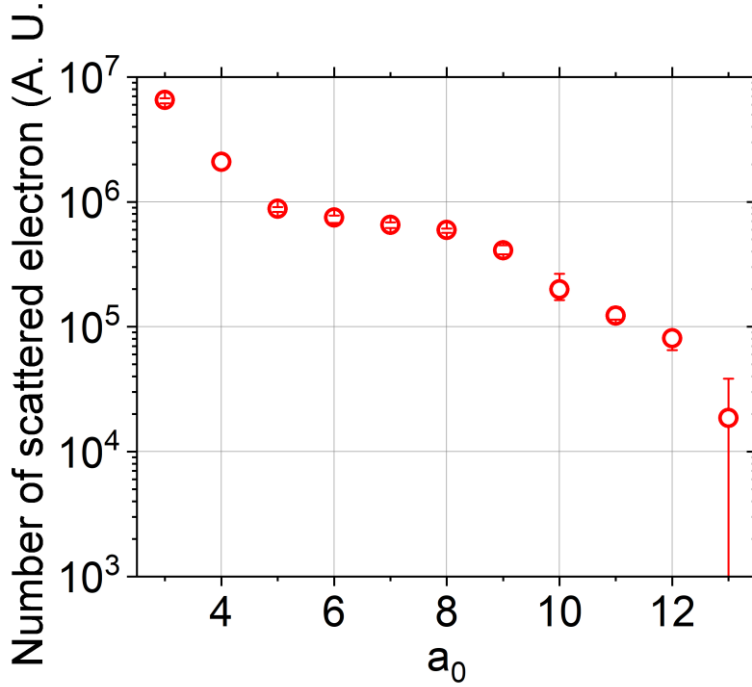
Figure 3.20: Distribution of scattering electrons with respect to a_0 for the shot #1781 calculated based on the parameters that resulted in gamma-ray profiles with SSIM > 0.9. The experimental parameters used in the simulation included variations in $\Delta T = -20$ to $20\ fs$, $\Delta x_{sl} = -4$ to $4\ \mu m$, $\Delta y_{sl} = 4\ \mu m$, and $\Delta z_{sl} = -12$ to $12\ \mu m$. Red circles represent the average scattering electrons at each laser intensity and error bars indicate the minimum and maximum values for the cases of SSIM > 0.9.

3.4. Gamma-ray energy spectrum

The reconstruction of gamma-ray energy spectra has been performed with two methods — SIRT and the cross-sectional method. For the cross-sectional method, the gamma-ray energy spectrum can be obtained from

$$\frac{dN_{\varepsilon_\gamma}}{d\varepsilon_\gamma} = \int N_{a_0} \int \frac{dn_e}{d\varepsilon_{e-}} \cdot \frac{d\sigma_{CSM}}{d\varepsilon_\gamma}(a_0, \varepsilon_{e-})\ d\varepsilon_{e-}\ da_0, \qquad (3.13)$$

where $\frac{dn_e}{d\varepsilon_{e-}}$ is the electron energy spectrum measured on Lanex3. The analysis result of the gamma-ray energy spectrum of the shot #1781 is shown in Figure 3.21. Figure 3.21 a) shows the histogram of scattering electrons with respect to a_0, obtained from Sec. 3.3. For this distribution, the gamma-ray energy spectrum was calculated using Eq. 3.13 and the result was shown as the red line in Figure 3.21 b). Also, the gamma-ray energy spectrum obtained by SIRT is shown in the blue line of Figure 3.21 b). The expected signal on LYSO-PX can be computed by,

$$PX = C \cdot \int \frac{dN_{\varepsilon_\gamma}}{d\varepsilon_\gamma} \cdot R_{LYSO-PX}(\varepsilon_\gamma)\ d\varepsilon_\gamma \qquad (3.14)$$

Here, PX is an expected LYSO-PX count, $R_{LYSO-PX}(\varepsilon_\gamma)$ is the response of LYSO-PX when a gamma-ray photon with energy ε_γ is injected, C is a normalization factor to make PX equal to the total count of the measured one. Figure 3.21 c) shows the measured signal of LYSO-PX and the calculated response of LYSO-PX using Eq. 3.14. The calculated response from the cross-sectional method matches well the measured response with R^2 of 0.99. Figure 3.21 d) shows

the total counts for the gamma rays with energy above ε_γ, which is obtained from the formula, $C \cdot \int_\varepsilon^\infty \frac{dN_{\varepsilon_\gamma}}{d\varepsilon_\gamma} \cdot R_{LYSO-PX}(\varepsilon_\gamma) \, d\varepsilon_\gamma$. For the measurement using the camera, the total noise is generally defined as $\sqrt{\sigma_{shot}^2 + \sigma_{back}^2}$, where σ_{shot} is a shot noise, σ_{back} is a background noise including the dark current noise and the readout noise. When the signal is large, the shot noise is equal to square root of signal. To estimate σ_{back}, the total count on LYSO−PX without Compton scattering was repeatedly measured 25 times, and the standard deviation of the total count without the signal was 6×10^6 counts, which corresponds to σ_{back}. For the shot #1781, the total noise level is $\sqrt{\sigma_{shot}^2 + \sigma_{back}^2} \approx 6 \times 10^6$, which sets ε_γ more than 450 MeV; the total count above this energy was more than two times the total noise level appeared in both methods. In other words, the gamma−rays with energy over 450 MeV meaningfully take part in the measured signal. Consequently, we claim from the measurement and analysis that gamma−rays with energy over 450 MeV was confirmed.

In the case of NCS, the scattering between an ultra−relativistic electron and n laser photons can produce gamma−ray photons up to the energy ε_γ[7, 61],

$$\varepsilon_\gamma \approx \frac{n}{1 + \frac{a_0^2}{2} + \frac{2n\gamma\varepsilon_L}{m_e c^2}(1 + cos\theta)} \varepsilon_{\gamma,cutoff} \qquad (3.15)$$

Here γ is the Lorentz factor of electron, ε_L is the energy of a laser photon, and θ is the scattering angle of NCS. After substituting Eq 3.6 into Eq. 3.15, Eq. 3.15 can be rearranged for the nonlinearity order, n, as follows:

$$n \approx \frac{\varepsilon_\gamma}{2\varepsilon_L \gamma(1 + \cos\theta)} \frac{(1 + \frac{a_0^2}{2})}{(\gamma - \frac{\varepsilon_\gamma}{mc^2})} \qquad (3.16)$$

In the above result and peak electron energy of 2.7 GeV as shown in Figure 2.29, the nonlinearity order was 286. In order words, 286 photons simultaneously scatter with an electron, emitting gamma‑ray photon of 450 MeV. Consequently, the analysis of the gamma‑ray energy spectrum from the shot #1781 showed that NCS occurred in the strongly nonlinear regime.

Figure 3.21: Analysis results of the measured gamma rays for the shot #1781. a) Histogram of scattering electrons with respect to a_0. b) Gamma-ray energy spectrum. The gamma-ray spectrum obtained with the cross-sectional method (CSM) is shown by the red line. The black dashed line is the one calculated for the n=1 case of CSM, i.e., the component of linear Compton scattering. The blue line represents the result by SIRT. c) Comparison of reconstructed LYSO-PX signals for the shot #1781. The black squares show the measured signal. The red and the blue lines represent CSM and SIRT obtained using Eq. 3.14, respectively. The black dashed line is the one calculated for the n=1 case of CSM. d) Total counts on LYSO-PX for $\varepsilon > \varepsilon_\gamma$. The black dashed line is the noise level. Gamma-rays up to 450 MeV was detectable.

3.5. Additional analysis of NCS gamma-ray results and conclusion

Four shots (shot #885, 902, 995, and 1512) with strong gamma-ray signals were analyzed by applying the same method used for the shot #1781. The electron energy spectra and LYSO-PX response for four shots are described in Figure 3.22 and Figure 3.23, respectively. Figure 3.24 shows the gamma-ray profile simulated with the parameters presented in Table 3. The parameters, resulting in SSIM over 0.9, were presented in Table 4. The analysis results for gamma-ray energy spectra are presented in Figs. 3. 25-3. 28.
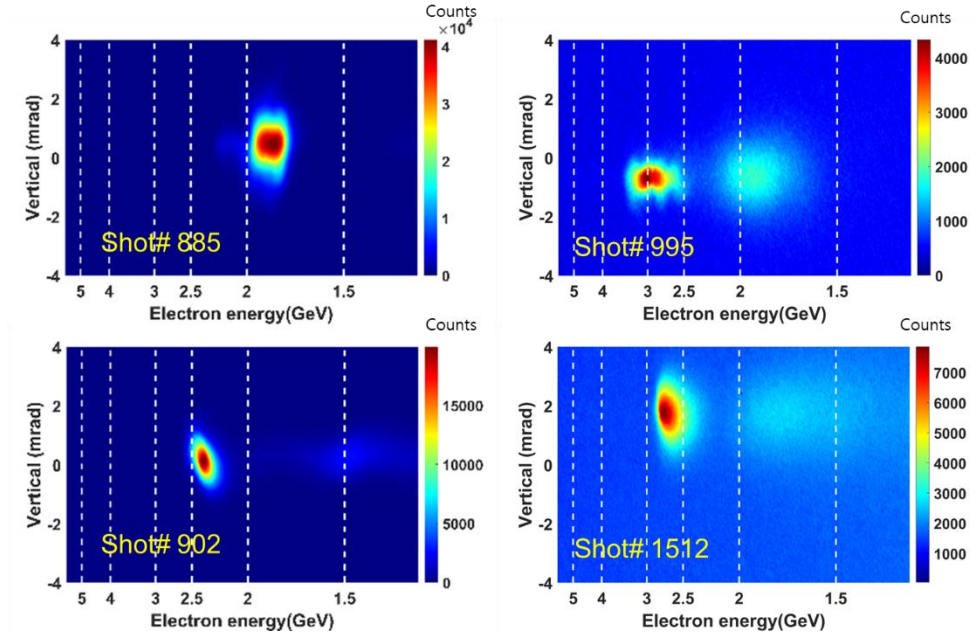
Figure 3.22: Measured electron energy spectra for the shots #885, 902, 995, and 1512.
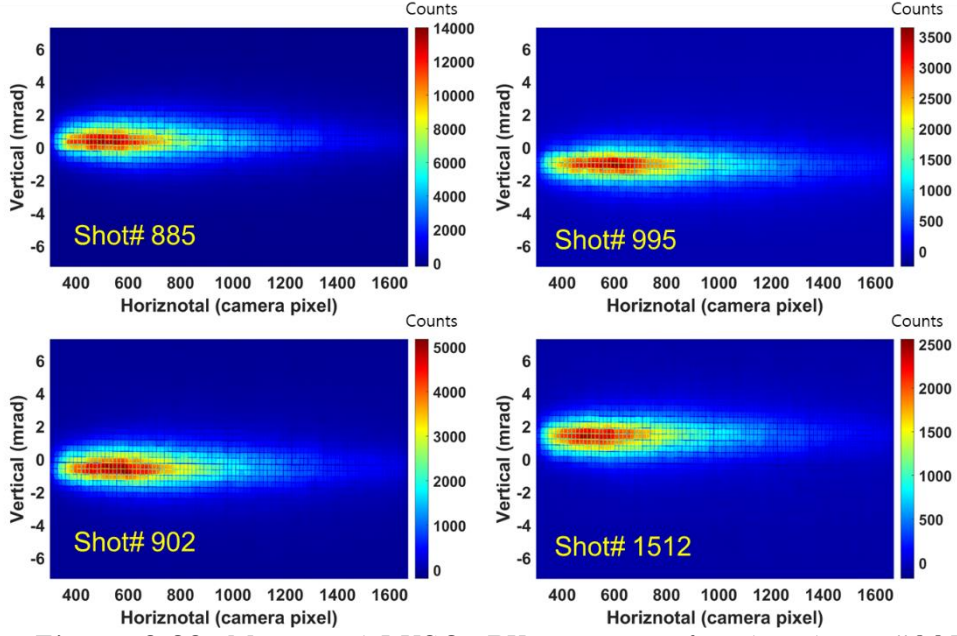
Figure 3.23: Measured LYSO-PX response for the shots #885, 902, 995, and 1512.
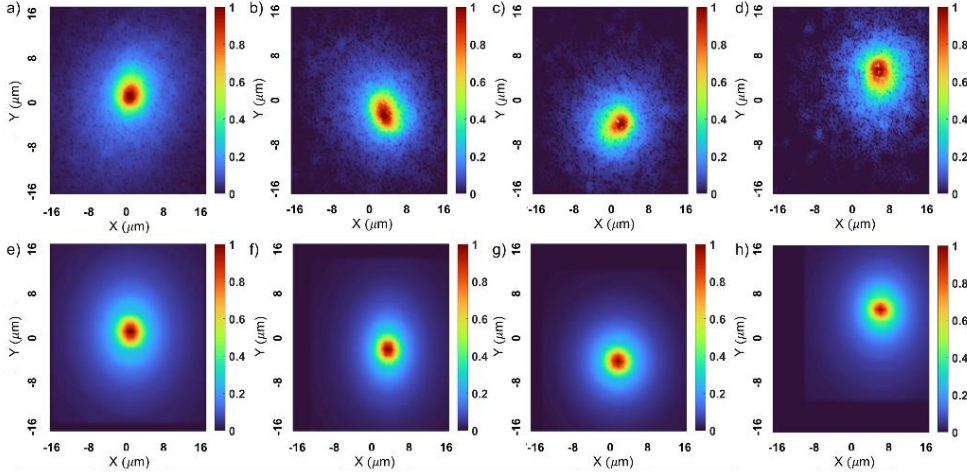
Figure 3.24: a-d) Gamma-ray profile measured by LYSO-SC for shots #885, 902, 995, and 1512 respectively. e-h) Gamma-ray profile simulated for shots #885, 902, 995, and 1512 with the experimental parameters presented in Table 3.

	ΔT (fs)	Δx_{sl} (μm)	Δy_{sl} (μm)	Δz_{sl} (μm)
885	10	0	1	0
902	40	0	-2	0
995	20	0	-4	0
1512	90	2	5	5

Table 3: Representative parameters for the shots #885, 902, 995, and 1512.

	ΔT (fs)	Δx_{sl} (μm)	Δy_{sl} (μm)	Δz_{sl} (μm)
885	-10 to 30	-4 to 4	1	-12 to 12
902	20 to 60	-2 to 4	-2	-12 to 12
995	0 to 40	-4 to 4	-4	-12 to 12
1512	80 to 100	0 to 4	5	-12 to 12

Table 4: Parameters giving SSIM over 0.9 for the shots #885, 902, 995, and 1512.
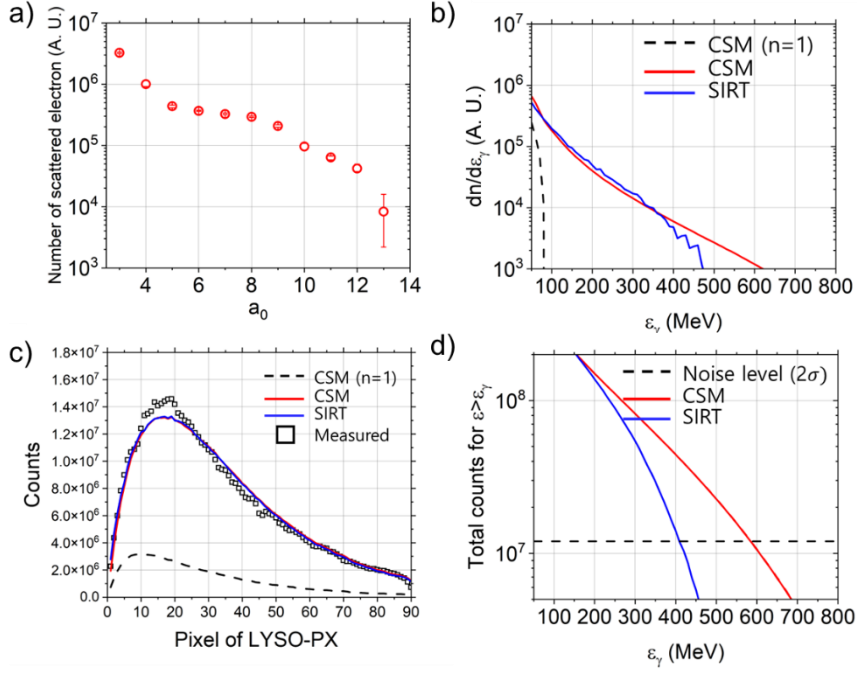
Figure 3.25: Analysis results of the measured gamma rays for the shot #885. a) Histogram of scattering electrons with respect to a_0. b) Gamma−ray energy spectrum. The gamma−ray spectrum obtained with the cross−sectional method (CSM) is shown by the red line. The black dashed line is the one calculated for the n=1 case of CSM, i.e., the component of linear Compton scattering. The blue line represents the result by SIRT. c) Comparison of reconstructed LYSO−PX signals for the shot #1781. The black squares show the measured signal. The red and blue lines represent CSM and SIRT obtained using Eq. 3.14, respectively. The black dashed line is the one calculated for the n=1 case of CSM. d) Total counts on LYSO−PX for $\varepsilon > \varepsilon_\gamma$. Gamma rays with energy up to 410 MeV were detectable.
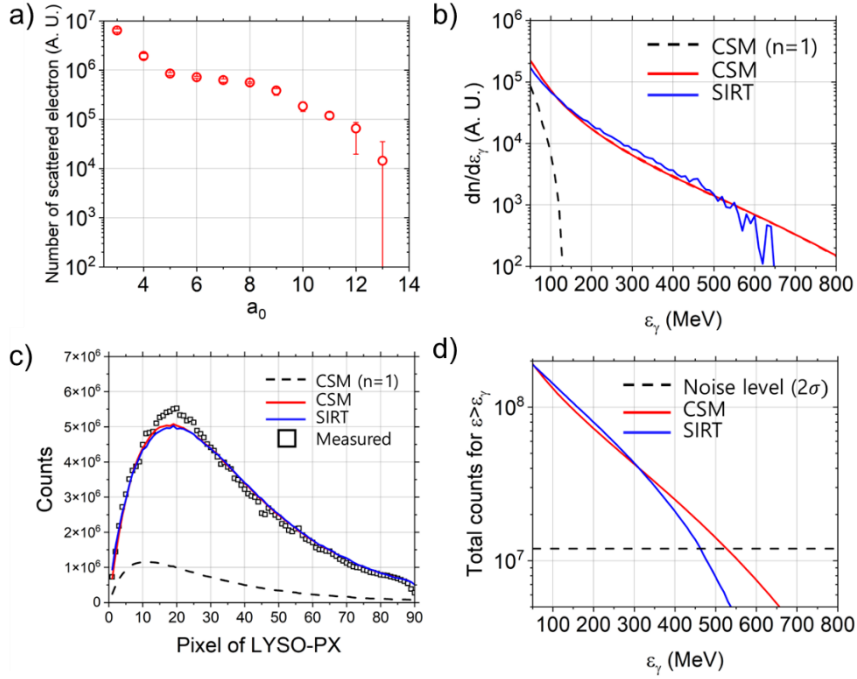
Figure 3.26: Analysis results of the measured gamma rays for the shot #902. a) Histogram of scattering electrons with respect to a_0. b) Gamma-ray energy spectrum. The gamma-ray spectrum obtained with the cross-sectional method (CSM) is shown by the red line. The black dashed line is the one calculated for the n=1 case of CSM, i.e., the component of linear Compton scattering. The blue line represents the result by SIRT. c) Comparison of reconstructed LYSO-PX signals for the shot #1781. The black squares show the measured signal. The red and blue lines represent CSM and SIRT obtained using Eq. 3.14, respectively. The black dashed line is the one calculated for the n=1 case of CSM. d) Total counts on LYSO-PX for $\varepsilon > \varepsilon_\gamma$. Up to 460 MeV gamma-ray was detectable.
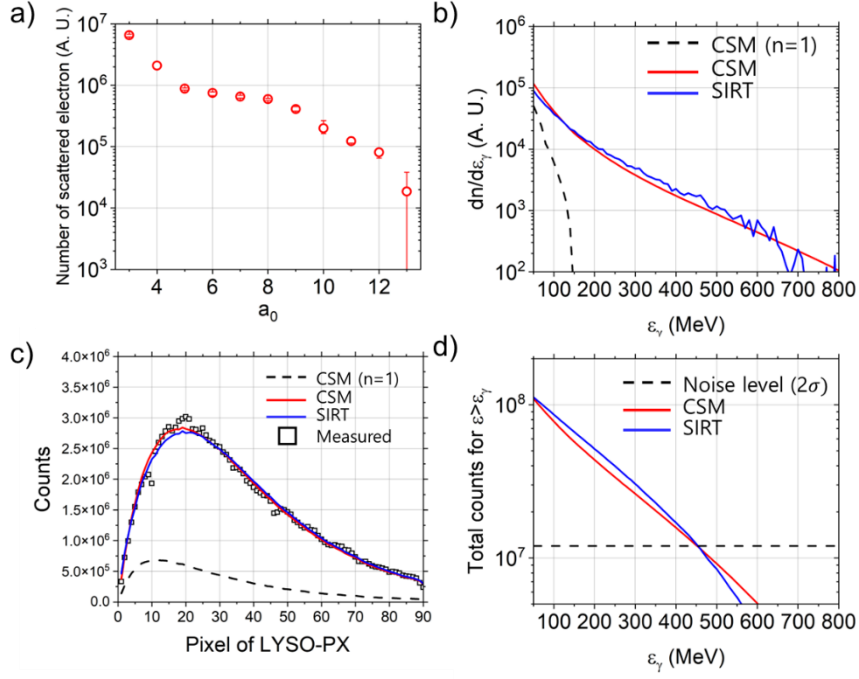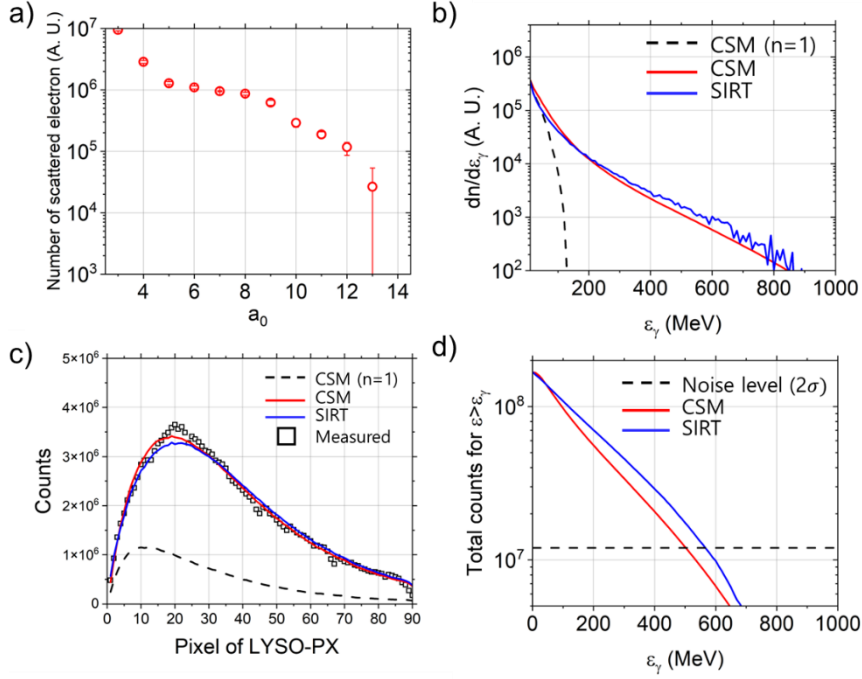
Figure 3.27: Analysis results of the measured gamma rays for the shot #995. a) Histogram of scattering electrons with respect to a_0. b) Gamma-ray energy spectrum. The gamma-ray spectrum obtained with the cross-sectional method (CSM) is shown by the red line. The black dashed line is the one calculated for the n=1 case of CSM, i.e., the component of linear Compton scattering. The blue line represents the result by SIRT. c) Comparison of reconstructed LYSO-PX signals for the shot #1781. The black squares show the measured signal. The red and blue lines represent CSM and SIRT obtained using Eq. 3.14, respectively. The black dashed line is the one calculated for the n=1 case of CSM. d) Total counts on LYSO-PX for $\varepsilon > \varepsilon_\gamma$. Up to 490 MeV gamma-ray was detectable.
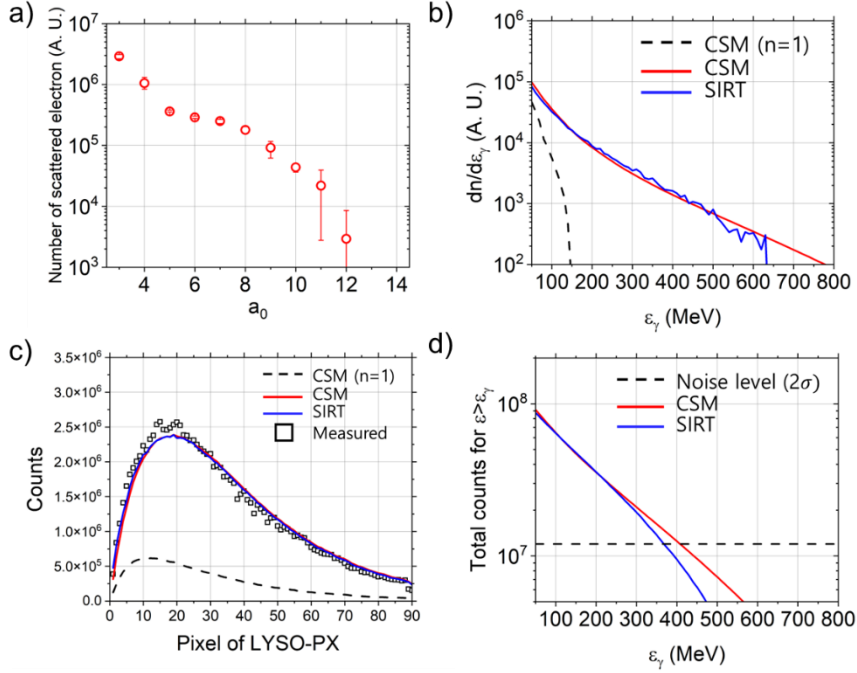
Figure 3.28: Analysis results of the measured gamma rays for the shot #1512. a) Histogram of scattering electrons with respect to a_0. b) Gamma-ray energy spectrum. The gamma-ray spectrum obtained with the cross-sectional method (CSM) is shown by the red line. The black dashed line is the one calculated for the n=1 case of CSM, i.e., the component of linear Compton scattering. The blue line represents the result by SIRT. c) Comparison of reconstructed LYSO-PX signals for the shot #1781. The black squares show the measured signal. The red and blue lines represent CSM and SIRT obtained using Eq. 3.14, respectively. The black dashed line is the one calculated for the n=1 case of CSM. d) Total counts on LYSO-PX for $\varepsilon > \varepsilon_\gamma$. Gamma-ray energy up to 360 MeV was detectable.

The NCS results by scattering laser peak intensity of $a_0 = 13$ with ultra−relativistic electrons ranging from 1.8 to 3.0 GeV were analyzed. Table 5 shows the analysis parameters for the shots #885, 902, 995, 1512, and 1781 − peak energy of the electrons, maximum measurable gamma−ray energy, nonlinearity order, and χ_e. The nonlinearity order indicates the minimum number of laser photons required to produce the maximum measurable gamma−ray energy by NCS. In the case of shot #885, relatively low energy electron, 1.8 GeV, produced a gamma−ray energy of 410 MeV, indicating a nonlinearity order of 630. The nonlinearity of a few hundred means the NCS experiment was performed in the highly nonlinear regime. In the case of shot #995, which had the highest peak electron energy, the strongest gamma−ray energy, 490 MeV, was measured. In this case, the strong field quantum electrodynamics parameter χ_e is 0.43, indicating that the NCS experiment was conducted in the strong field quantum electrodynamics regime close to $\chi_e=1$.

	ε_{e^-} (GeV)	$\varepsilon_{\gamma,max}$ (MeV)	Nonlinearity order	χ_e
885	1.8	410	630	0.26
902	2.4	460	380	0.34
995	3.0	490	251	0.43
1512	2.7	360	220	0.39
1781	2.7	450	286	0.39

Table 5: Analysis results for the shots #885, 902, 995, 1512 and 1781.

In this NCS research, gamma-ray energy spectra were reconstructed using the two methods - the cross-sectional method and SIRT. The SIRT used LYSO-PX measurement results and Geant4 simulations to obtain the gamma-ray energy spectra. The cross-sectional method primarily estimated the laser intensity during scattering through simulation to calculate gamma-ray energy spectra. The simulation input parameters, including the time delay, the scattering laser beam pointing, and the defocus of scattering laser beam, were obtained by comparing the measured and the simulated gamma-ray profiles. Both methods revealed the production of gamma rays with energy much larger than the cutoff energy of linear Compton scattering. For example, for the shot #995, the gamma-ray energy of 490 MeV was obtained, while the cutoff energy of linear Compton scattering is 200 MeV. Here, the gamma-ray photon of 490 MeV was generated from the Compton scattering of an electron with more than 250 photons. As with the other four shots analyzed, the results from the NCS experiment confirmed that the nonlinearity order was as high as 630. Consequently, the analyzed results confirmed that the NCS was experimentally demonstrated in the strongly nonlinear regime with the quantum nonlinearity parameter as high as $\chi_e = 0.43$.

Chapter 4. Conclusion

Nonlinear Compton scattering (NCS) has been explored to investigate light−matter interactions in the strong field QED regime. A series of NCS experiments with a multi−PW laser was designed and performed using an ultra−relativistic electron beam and an ultrahigh intensity laser. For the investigation of the strong field QED regime, an electron beam with energy of 2 − 3 GeV was produced from a He gas cell driven by a PW laser using the LWFA method, and a scattering laser with the normalized vector potential $a_0 \approx 13$ was prepared. As the spatiotemporal synchronization between the electron and the scattering laser beams determines the occurrence of scattering and affects the actual laser intensity during the scattering with an electron beam, a set of spatiotemporal synchronization systems were developed. The first spatiotemporal synchronization system with a pellicle at the scattering position achieved the temporal synchronization with a jitter of 11 fs. In addition, the real−time delay monitoring system using spatial and spectral interferometry measured the time delay range up to 200 fs between the main driving laser and the scattering laser during an experiment, maintaining the time delay within 14 fs (rms). With these installations, the scattering probability increased up to 40%.

In this series of NCS experiments with a collection of 113 gamma−ray data, five results with strong gamma−ray signals were analyzed. Gamma−ray energy spectra were retrieved from the measured signal on the pixelated LYSO detector by applying two

methods, SIRT and the cross−sectional method. In the case of SIRT a gamma−ray energy spectrum was retrieved from a pixelated LYSO signal by an iteration based on the response function calculated using the GEANT4 code for a set of gamma−ray energies. In the case of the cross−sectional method, the gamma−ray energy spectrum for given experimental parameters, including the time delay, the scattering laser beam pointing, and the defocus of scattering laser beam, was calculated using the cross section of nonlinear Compton scattering. The laser intensity during scattering was estimated from the measured gamma−ray profile on the single crystal LYSO. The gamma−ray energy spectrum obtained from both methods showed good agreement when compared to check consistency. In the case of the gamma−ray energy spectrum obtained with an electron beam with a peak energy of 3.0 GeV, the gamma−ray energy extended up to 490 MeV, which far exceeded the cutoff energy, 200 MeV, of linear Compton scattering. Considering the scattering laser intensity estimated from the analysis, the normalized vector potential, a_0, was 13, and the corresponding quantum nonlinear parameter χ_e was 0.43. This result was a clear indication that the NCS occurred between an electron and 250 laser photons. Since this kind of experimental results has not been reported before, our experimental data will pave the road to the new physics regime of strong field QED and provide crucial data to prompt theoretical advancements in this area.

Bibliography

1.   D. Hanneke, S. Fogwell and G. Gabrielse, Phys Rev Lett **100** (12), 120801 (2008).
2.   T. Aoyama, M. Hayakawa, T. Kinoshita and M. Nio, Phys Rev Lett **109** (11), 111807 (2012).
3.   J. Schwinger, Physical Review **82** (5), 664-679 (1951).
4.   M. Buchanan, Nature Physics **2** (11), 721-721 (2006).
5.   W. H.-H. EULER, Z. Phys. **98**, 714 (1936).
6.   J. W. Yoon, Y. G. Kim, I. W. Choi, J. H. Sung, H. W. Lee, S. K. Lee and C. H. Nam, Optica **8** (5) (2021).
7.   A. Di Piazza, C. Müller, K. Z. Hatsagortsyan and C. H. Keitel, Reviews of Modern Physics **84** (3), 1177-1228 (2012).
8.   N. Narozhnyi, A. I. Nikishov and V. Ritus, Zh. Eksperim. i Teor. Fiz. **47** (1964).
9.   C. Bula, K. T. McDonald, E. J. Prebys, C. Bamber, S. Boege, T. Kotseroglou, A. C. Melissinos, D. D. Meyerhofer, W. Ragg, D. L. Burke, R. C. Field, G. Horton-Smith, A. C. Odian, J. E. Spencer, D. Walz, S. C. Berridge, W. M. Bugg, K. Shmakov and A. W. Weidemann, Phys Rev Lett **76** (17), 3116-3119 (1996).
10.   E. Esarey, C. B. Schroeder and W. P. Leemans, Reviews of Modern Physics **81** (3), 1229-1285 (2009).
11.   S. Chen, N. D. Powers, I. Ghebregziabher, C. M. Maharjan, C. Liu, G. Golovin, S. Banerjee, J. Zhang, N. Cunningham, A. Moorti, S. Clarke, S. Pozzi and D. P. Umstadter, Phys Rev Lett **110** (15), 155003 (2013).
12.   G. Sarri, D. J. Corvan, W. Schumaker, J. M. Cole, A. Di Piazza, H. Ahmed, C. Harvey, C. H. Keitel, K. Krushelnick, S. P. Mangles, Z. Najmudin, D. Symes, A. G. Thomas, M. Yeung, Z. Zhao and M. Zepf, Phys Rev Lett **113** (22), 224801 (2014).
13.   K. Khrennikov, J. Wenz, A. Buck, J. Xu, M. Heigoldt, L. Veisz and S. Karsch, Physical Review Letters **114** (19) (2015).
14.   J. M. Cole, K. T. Behm, E. Gerstmayr, T. G. Blackburn, J. C. Wood, C. D. Baird, M. J. Duff, C. Harvey, A. Ilderton, A. S. Joglekar, K. Krushelnick, S. Kuschel, M. Marklund, P. McKenna, C. D. Murphy, K. Poder, C. P. Ridgers, G. M. Samarin, G. Sarri, D. R. Symes, A. G. R. Thomas, J. Warwick, M. Zepf, Z. Najmudin and S. P. D. Mangles, Physical Review X **8** (1) (2018).
15.   W. Yan, C. Fruhling, G. Golovin, D. Haden, J. Luo, P. Zhang, B. Zhao, J. Zhang, C. Liu, M. Chen, S. Chen, S. Banerjee and D. Umstadter, Nature Photonics **11** (8), 514-520 (2017).
16.   K. Poder, M. Tamburini, G. Sarri, A. Di Piazza, S. Kuschel, C.

D. Baird, K. Behm, S. Bohlen, J. M. Cole, D. J. Corvan, M. Duff, E. Gerstmayr, C. H. Keitel, K. Krushelnick, S. P. D. Mangles, P. McKenna, C. D. Murphy, Z. Najmudin, C. P. Ridgers, G. M. Samarin, D. R. Symes, A. G. R. Thomas, J. Warwick and M. Zepf, Physical Review X **8** (3) (2018).

17.   J. H. Sung, H. W. Lee, J. Y. Yoo, J. W. Yoon, C. W. Lee, J. M. Yang, Y. J. Son, Y. H. Jang, S. K. Lee and C. H. Nam, Opt Lett **42** (11), 2058-2061 (2017).

18.   G. Breit and J. A. Wheeler, Physical Review **46** (12), 1087-1091 (1934).

19.   D. L. Burke, R. C. Field, G. Horton-Smith, J. E. Spencer, D. Walz, S. C. Berridge, W. M. Bugg, K. Shmakov, A. W. Weidemann, C. Bula, K. T. McDonald, E. J. Prebys, C. Bamber, S. J. Boege, T. Koffas, T. Kotseroglou, A. C. Melissinos, D. D. Meyerhofer, D. A. Reis and W. Ragg, Physical Review Letters **79** (9), 1626-1629 (1997).

20.   X. Ribeyre, E. d'Humieres, O. Jansen, S. Jequier, V. T. Tikhonchuk and M. Lobet, Phys Rev E **93** (1), 013201 (2016).

21.   G. Baldwin and G. Klaiber, Physical Review **71** (1), 3 (1947).

22.   J. Pruet, D. McNabb, C. Hagmann, F. Hartemann and C. Barty, Journal of Applied Physics **99** (12), 123102 (2006).

23.   D. Habs, T. Tajima, J. Schreiber, C. P. J. Barty, M. Fujiwara and P. G. Thirolf, The European Physical Journal D **55** (2), 279-285 (2009).

24.   R. Hajima, T. Hayakawa, T. Shizuma, C. Angell, R. Nagai, N. Nishimori, M. Sawamura, S. Matsuba, A. Kosuge and M. Mori, The European Physical Journal Special Topics **223** (6), 1229-1236 (2014).

25.   M. M. Gunther, O. N. Rosmej, P. Tavana, M. Gyrdymov, A. Skobliakov, A. Kantsyrev, S. Zahter, N. G. Borisenko, A. Pukhov and N. E. Andreev, Nat Commun **13** (1), 170 (2022).

26.   L. Serafini, I. Drebot, A. Bacci, F. Broggi, C. Curatolo, A. Marocchino, N. Panzeri, V. Petrillo, A. R. Rossi and M. R. Conti, Nuclear Instruments and Methods in Physics Research Section A: Accelerators, Spectrometers, Detectors and Associated Equipment **909**, 309-313 (2018).

27.   S. Corde, K. T. Phuoc, G. Lambert, R. Fitour, V. Malka, A. Rousse, A. Beck and E. Lefebvre, Reviews of Modern Physics **85** (1), 1 (2013).

28.   K. Petersson and Collaborators, Res Outreach **2020** (117), 66-69 (2020).

29.   J. D. Wilson, E. M. Hammond, G. S. Higgins and K. Petersson, Frontiers in oncology **9**, 1563 (2020).

30.   N. Esplen, M. S. Mendonca and M. Bazalova-Carter, Phys Med Biol **65** (23), 23TR03 (2020).

31.   A. Einstein, Physikalische

Zeitschrift **18**, 121–128 (1917).

32.   T. H. Maiman, Nature **187** (4736), 493–494 (1960).

33.   F. J. McClung and R. W. Hellwarth, Appl. Opt. **1** (S1), 103–105 (1962).

34.   L. E. Hargrove, R. L. Fork and M. A. Pollack, Applied Physics Letters **5** (1), 4–5 (1964).

35.   D. A. Stetser and A. J. DeMaria, Applied Physics Letters **9** (3), 118–120 (1966).

36.   J. P. Laussade and A. Yariv, Applied Physics Letters **13** (2), 65–66 (1968).

37.   D. Strickland and G. Mourou, Optics Communications **56** (3), 219–221 (1985).

38.   C. N. Danson, C. Haefner, J. Bromage, T. Butcher, J.-C. F. Chanteloup, E. A. Chowdhury, A. Galvanauskas, L. A. Gizzi, J. Hein, D. I. Hillier, N. W. Hopps, Y. Kato, E. A. Khazanov, R. Kodama, G. Korn, R. Li, Y. Li, J. Limpert, J. Ma, C. H. Nam, D. Neely, D. Papadopoulos, R. R. Penman, L. Qian, J. J. Rocca, A. A. Shaykin, C. W. Siders, C. Spindloe, S. Szatmári, R. M. G. M. Trines, J. Zhu, P. Zhu and J. D. Zuegel, High Power Laser Science and Engineering **7** (2019).

39.   T. Tajima and J. M. Dawson, Physical Review Letters **43** (4), 267 (1979).

40.   J. Faure, Y. Glinec, A. Pukhov, S. Kiselev, S. Gordienko, E. Lefebvre, J.-P. Rousseau, F. Burgy and V. Malka, Nature **431** (7008), 541–544 (2004).

41.   C. Geddes, C. Toth, J. Van Tilborg, E. Esarey, C. Schroeder, D. Bruhwiler, C. Nieter, J. Cary and W. Leemans, Nature **431** (7008), 538–541 (2004).

42.   M. C. Downer, R. Zgadzaj, A. Debus, U. Schramm and M. C. Kaluza, Reviews of Modern Physics **90** (3), 035002 (2018).

43.   G. Schmidt, *Physics of high temperature plasmas*. (Elsevier, 2012).

44.   H. T. Kim, V. B. Pathak, K. Hong Pae, A. Lifschitz, F. Sylla, J. H. Shin, C. Hojbota, S. K. Lee, J. H. Sung, H. W. Lee, E. Guillaume, C. Thaury, K. Nakajima, J. Vieira, L. O. Silva, V. Malka and C. H. Nam, Sci Rep **7** (1), 10203 (2017).

45.   Y. Ji, Y. Chung, D. Sprinzak, M. Heiblum, D. Mahalu and H. Shtrikman, Nature **422** (6930), 415–418 (2003).

46.   C. Aniculaesei, H. T. Kim, B. J. Yoo, K. H. Oh and C. H. Nam, Rev Sci Instrum **89** (2), 025110 (2018).

47.   L. Antonucci, X. Solinas, A. Bonvalet and M. Joffre, Opt Express **28** (12), 18251–18260 (2020).

48.   D. J. Corvan, T. Dzelzainis, C. Hyland, G. Nersisyan, M. Yeung, M. Zepf and G. Sarri, Opt. Express **24** (3), 3127–3136 (2016).

49.   D. Y. Kim, C. I. Hojbota, M. Mirzaie, S. K. Lee, K. Y. Kim, J. H. Sung and C. H. Nam, Rev Sci Instrum **93** (11), 113001 (2022).
50.   C. I. Hojbota, H. T. Kim, J. H. Shin, C. Aniculaesei, B. S. Rao and C. H. Nam, AIP Advances **9** (8) (2019).
51.   T. Andre, I. A. Andriyash, A. Loulergue, M. Labat, E. Roussel, A. Ghaith, M. Khojoyan, C. Thaury, M. Valleau, F. Briquez, F. Marteau, K. Tavakoli, P. N'Gotta, Y. Dietrich, G. Lambert, V. Malka, C. Benabderrahmane, J. Veteran, L. Chapuis, T. El Ajjouri, M. Sebdaoui, N. Hubert, O. Marcouille, P. Berteaud, N. Leclercq, M. El Ajjouri, P. Rommeluere, F. Bouvet, J. Duval, C. Kitegi, F. Blache, B. Mahieu, S. Corde, J. Gautier, K. Ta Phuoc, J. P. Goddet, A. Lestrade, C. Herbeaux, C. Evain, C. Szwaj, S. Bielawski, A. Tafzi, P. Rousseau, S. Smartsev, F. Polack, D. Dennetiere, C. Bourassin-Bouchet, C. De Oliveira and M. E. Couprie, Nat Commun **9** (1), 1334 (2018).
52.   H. J. Cha, I. W. Choi, H. T. Kim, I. J. Kim, K. H. Nam, T. M. Jeong and J. Lee, Rev Sci Instrum **83** (6), 063301 (2012).
53.   C. A. Schneider, W. S. Rasband and K. W. Eliceiri, Nat Methods **9** (7), 671-675 (2012).
54.   H. Rutishauser, Numerische Mathematik **13** (1), 4-13 (1969).
55.   W. Wei, Y. Biwen and W. Jiexian, Geodesy and Geodynamics **4** (1), 41-45 (2013).
56.   S. Agostinelli, J. Allison, K. Amako, J. Apostolakis, H. Araujo, P. Arce, M. Asai, D. Axen, S. Banerjee, G. Barrand, F. Behner, L. Bellagamba, J. Boudreau, L. Broglia, A. Brunengo, H. Burkhardt, S. Chauvie, J. Chuma, R. Chytracek, G. Cooperman, G. Cosmo, P. Degtyarenko, A. Dell'Acqua, G. Depaola, D. Dietrich, R. Enami, A. Feliciello, C. Ferguson, H. Fesefeldt, G. Folger, F. Foppiano, A. Forti, S. Garelli, S. Giani, R. Giannitrapani, D. Gibin, J. J. Gómez Cadenas, I. González, G. Gracia Abril, G. Greeniaus, W. Greiner, V. Grichine, A. Grossheim, S. Guatelli, P. Gumplinger, R. Hamatsu, K. Hashimoto, H. Hasui, A. Heikkinen, A. Howard, V. Ivanchenko, A. Johnson, F. W. Jones, J. Kallenbach, N. Kanaya, M. Kawabata, Y. Kawabata, M. Kawaguti, S. Kelner, P. Kent, A. Kimura, T. Kodama, R. Kokoulin, M. Kossov, H. Kurashige, E. Lamanna, T. Lampén, V. Lara, V. Lefebure, F. Lei, M. Liendl, W. Lockman, F. Longo, S. Magni, M. Maire, E. Medernach, K. Minamimoto, P. Mora de Freitas, Y. Morita, K. Murakami, M. Nagamatu, R. Nartallo, P. Nieminen, T. Nishimura, K. Ohtsubo, M. Okamura, S. O'Neale, Y. Oohata, K. Paech, J. Perl, A. Pfeiffer, M. G. Pia, F. Ranjard, A. Rybin, S. Sadilov, E. Di Salvo, G. Santin, T. Sasaki, N. Savvas, Y. Sawada, S. Scherer, S. Sei, V. Sirotenko, D. Smith, N. Starkov, H. Stoecker, J. Sulkimo, M. Takahata, S. Tanaka, E. Tcherniaev, E. Safai Tehrani, M. Tropeano, P. Truscott, H. Uno, L. Urban, P. Urban, M. Verderi, A. Walkden, W. Wander, H.

Weber, J. P. Wellisch, T. Wenaus, D. C. Williams, D. Wright, T. Yamada, H. Yoshida and D. Zschiesche, Nuclear Instruments and Methods in Physics Research Section A: Accelerators, Spectrometers, Detectors and Associated Equipment **506** (3), 250-303 (2003).

57.   J. Allison, K. Amako, J. Apostolakis, P. Arce, M. Asai, T. Aso, E. Bagli, A. Bagulya, S. Banerjee, G. Barrand, B. R. Beck, A. G. Bogdanov, D. Brandt, J. M. C. Brown, H. Burkhardt, P. Canal, D. Cano-Ott, S. Chauvie, K. Cho, G. A. P. Cirrone, G. Cooperman, M. A. Cortés-Giraldo, G. Cosmo, G. Cuttone, G. Depaola, L. Desorgher, X. Dong, A. Dotti, V. D. Elvira, G. Folger, Z. Francis, A. Galoyan, L. Garnier, M. Gayer, K. L. Genser, V. M. Grichine, S. Guatelli, P. Guèye, P. Gumplinger, A. S. Howard, I. Hřivnáčová, S. Hwang, S. Incerti, A. Ivanchenko, V. N. Ivanchenko, F. W. Jones, S. Y. Jun, P. Kaitaniemi, N. Karakatsanis, M. Karamitros, M. Kelsey, A. Kimura, T. Koi, H. Kurashige, A. Lechner, S. B. Lee, F. Longo, M. Maire, D. Mancusi, A. Mantero, E. Mendoza, B. Morgan, K. Murakami, T. Nikitina, L. Pandola, P. Paprocki, J. Perl, I. Petrović, M. G. Pia, W. Pokorski, J. M. Quesada, M. Raine, M. A. Reis, A. Ribon, A. Ristić Fira, F. Romano, G. Russo, G. Santin, T. Sasaki, D. Sawkey, J. I. Shin, I. I. Strakovsky, A. Taborda, S. Tanaka, B. Tomé, T. Toshito, H. N. Tran, P. R. Truscott, L. Urban, V. Uzhinsky, J. M. Verbeke, M. Verderi, B. L. Wendt, H. Wenzel, D. H. Wright, D. M. Wright, T. Yamashita, J. Yarba and H. Yoshida, Nuclear Instruments and Methods in Physics Research Section A: Accelerators, Spectrometers, Detectors and Associated Equipment **835**, 186-225 (2016).

58.   V. N. Baier and V. M. Katkov, Physics Letters A **25** (7), 492-493 (1967).

59.   T. Erber, Reviews of Modern Physics **38** (4), 626-659 (1966).

60.   A. I. N. a. V. I. RITUS, SOVIET PHYSICS JETP **19** (2), 529 (1964).

61.   V. I. Ritus, Journal of Soviet Laser Research **6** (5), 497-617 (1985).

62.   Z. Wang, A. C. Bovik, H. R. Sheikh and E. P. Simoncelli, IEEE Trans Image Process **13** (4), 600-612 (2004).

PW 레이저를 이용한 비선형 컴프톤 산란 실험을 위한 광학 및 감마선 진단계 개발

김 도 연

에너지시스템공학부

서울대학교 대학원

이 논문은 고에너지 전자와 초강력 레이저 사이의 비선형 컴프턴 산란을 실험적으로 구현하고 분석하는데 필요한 광학 및 감마선 진단계를 다룬다. PW 레이저 기술의 발전으로 강한 전기장 하에서의 양자전기역학이 본격적으로 연구되기 시작했다. 레이저 웨이크필드 가속 방식을 기반으로 PW레이저로 헬륨 가스 표적에 입사하여 수 GeV 에너지ㅡ이 전자빔을 생성하였다. 이 전자빔이 초강력 레이저와 산란될 때 다중 광자 컴프톤 산란, 즉 비선형 컴프톤 산란이 발생하여 선형 컴프톤 산란의 한계에너지 보다 강한 에너지의 감마선을 생성할 수 있다. 비선형 컴프톤 산란 실험을 수행하기 위해서는 전자를 가속하는 레이저와 충돌시키고자 하는 레이저의 시공간 동기화가 준비되어야 한다. spatial interferometer와 spectral interferometer로 구성된 실시간 두 레이저 사이의 시간 지연 측정 시스템을 도입하여 컴프톤 산란 실험을 성공적으로 수행하였고 이때 성공률을 40 %로

상승시켰다.

컴프톤 산란에서 생성된 감마선 진단을 위해 공간분포를 측정하기 위한 신틸레이터와 에너지 스펙트럼을 측정하기 위한 신틸레이터가 준비되었다. 비선형 컴프톤 산란에 의해 생성된 감마선 에너지 분포는 두가지 방법으로 구하였다. 첫번째는 비선형 컴프톤 산란 단면적에 기초하여 계산하는 것이며 두번째는 동시 반복 재구성 기법을 사용하는 것이다. 우선 비선형 컴프톤 산란 단면적을 이용하기 위해서는 산란 시 레이저의 세기를 알아야 한다. 산란 중의 레이저의 세기와 산란한 전자수는 전자와 충돌 레이저를 (x, y, z, t)에 구현하여 구하였으며, 이를 바탕으로 비선형 컴프톤 산란 단면적을 이용하여 감마선 에너지 분포를 계산하였다. 다른 한편으로 동시 반복 재구성 기법을 이용하여 픽셀화된 신틸레이터의 측정결과를 분석하여 감마선 에너지 분포를 얻었다. 두 방법으로 구한 감마선 에너지 스펙트럼이 선형 컴프톤 산란의 한계 에너지를 초과하는 수백 MeV까지 있었음을 확인함으로써 비선형 컴프톤 산란이 실험적으로 일어나는 것을 검증하였다. 이 연구를 통해 강한 전기장 하에서의 양자전기역학의 빛과 입자 사이의 상호작용을 실험적으로 연구할 수 있었다.

감사의 글

많은 분들의 도움이 있었기에 저의 연구와 박사학위논문을 잘 마무리할 수 있었습니다. 이 글을 통해 감사의 인사를 드리고자 합니다.

먼저 대학원생활을 지도해주신 황용석 지도교수님께 감사드립니다. 대학원에서의 가르침과 쌓은 경험이 있었기에 연구단으로 옮겨서도 새로운 실험실에 적응할 수 있었습니다. 다소 생소할 수 있는 연구주제라도 박사학위를 끝까지 마칠 수 있도록 이끌어 주셔서 감사드립니다.

저의 연구를 지도해 주시며 학위논문 작성까지 이끌어 주신 남창희 단장님께 감사를 표합니다. 단장님 덕분에 좋은 연구를 주제로 연구를 할 수 있었고, 연구 노하우를 알려주신 덕분에 데이터를 사료 깊게 해석하고 논리적으로 정리하는 연구자로써 소양을 기를 수 있었습니다.

바쁜 상황에서도 논문의 심사를 맡아 주시고 연구 결과를 발전시키며 정리하는데 도움을 주신 김기용 교수님, 정경재 교수님, 김기현 교수님께 감사드립니다.

연구 결과에 대해서 언제든 활발히 논의해주었던 Dr. Calin Ioan HOJBOTA와 Dr. Mohammad Mirzaie에게 감사의 말을 전합니다—I am grateful for the multiple discussions on the LWFA and NCS with Dr. Calin Ioan HOJBOTA and Dr. Mohammad Mirzaie, which led to highly successful experiments). 레이저와 레이저를 응용하는 실험에 대해 여쭤볼 때마다 친절히 알려주신 김형택, 성재희, 윤진우, 이성구, 최일우

박사님께 감사드립니다.